MAGNETO-DIELECTRIC MATERIAL CHARACTERIZATION AND RF ANTENNA DESIGN

A Dissertation
Presented to
The Academic Faculty

By

Kyu Hwan Han

In Partial Fulfillment
of the Requirements for the Degree
Doctor of Philosophy in the
School of Electrical and Computer Engineering

Georgia Institute of Technology
August 2015

MAGNETO-DIELECTRIC MATERIAL CHARACTERIZATION AND RF ANTENNA DESIGN

Approved by:

Dr. Madhavan Swaminathan, Advisor
School of Electrical and Computer Engineering
Georgia Institute of Technology

Dr. Raj M. Pulugurtha
School of Electrical and Computer Engineering
Georgia Institute of Technology

Dr. Andrew F. Peterson
School of Electrical and Computer Engineering
Georgia Institute of Technology

Dr. Meilin Liu
School of Materials Science and Engineering
Georgia Institute of Technology

Dr. Gregory D. Durgin
School of Electrical and Computer Engineering
Georgia Institute of Technology

Date Approved: April 23rd 2015

To Jesus, my Lord

ACKNOWLEDGMENTS

Before I begin, I would like to give thanks God, whom gives all my strength, wisdom and everything else to make this dissertation possible. Without him, I would not be able to accomplish this wonderful experience.

Also, I honorably appreciate the support from colleagues and friends helping and encouraging me to achieve this goal during my Ph. D program at Georgia Tech. I present my grand appreciation to my great academic advisor, Prof. Madhavan Swaminathan, for everything he had done for me to guide through this tunnel, and giving me the unforgettable opportunity to join his group, Mixed Signal Design Group. This became a turning point of my career and life. I admire his passion towards the research and his students, and his continuous support, trust, guidance, and encouragement allowed me to finally present this dissertation to the world. I wish to follow his path as a scholar and an engineer.

I am also grateful for the effort of committee members, Dr. Andrew F. Peterson, Dr. Gregory D. Durgin, Dr. Raj M. Pulugurtha and Dr. Meilin Liu to enhance my dissertation with their precious discussions and comments.

During my Ph. D study, I have met so many wonderful members of the Mixed Signal Design Group. I appreciate Dr. Sunghwan Min and Dr. Junki Min for mentoring my research. Technical discussion with them helped me to shape my goal. I was lucky to have talented and smart colleagues Dr. Nevin Altunyurt, Dr. Seunghyun Hwang, Dr. Jianyong Xie, Dr. Myunghyun Ha, Dr. Suzanne Huh, Dr. Narayanan T.V., Dr. Abhilash Goyal, Dr. Jaeyoung Choi, Dr. Biancun Xie, and Dr. Satyan Telikepalli. Especially I would like to thank Dr. Nevin Altunyurt who helped me on my early Ph. D. life for shaping and boosting

my research progress. I would also like to give credits to colleagues whom I spent my recent years: Stephen Dumas, David Zhang, Sung Joo Park, Rishik Bazaz, Ming Yi, Diapa Sonogo, Sang Kyu Kim, Coline Pardue and Hanbyul Kim for their support and valuable discussion during our group meetings.

I acknowledge that many people outside the lab supported me throughout this Ph. D program years. I would like to thank members of Georgia Tech Korean Student Association (GTKSA). Experience as a president, vice-president and senior advisor with them for the last few years was invaluable for building my Ph. D. life. I also appreciate members of the New Church of Atlanta for encouraging me to achieve this dissertation, especially Pastor Bill Sim, Pastor Timothy Eom, Kyoung Sun Ryu and Mark Sohn. I thank them for supporting me to know and believe Jesus.

How can I thank my family for their devotion and their lives to support their son? I thank God that He allowed me this perfect and lovely parents to me. My father, Duck Young Han, who used to be a great electrical engineer, gave me an inspiration to also be an engineer. He has always been my role model and he will be my life-time advisor forever. My mother, Young Hee Lee, who has the warmest heart to her family and her son, loves me so much and I cannot forget her devotion to her family. I just want to say that I am so lucky for being their son. I also thank my brother, Young Hwan Han, who prayed for me to get through this tough Ph. D. life. I thank him for being my young brother and my life time friend. Thank you all and love you all.

TABLE OF CONTENTS

ACKNOWLEDGMENTS ..... **IV**

LIST OF TABLES ..... **IX**

LIST OF FIGURES ..... **X**

SUMMARY ..... **XVI**

CHAPTER 1 INTRODUCTION **1**

1.1 Background and Motivation 1

1.2 Contributions 7

1.3 Organization of the Dissertation 8

CHAPTER 2 MAGNETO-DIELECTRIC COMPOSITE MATERIAL SYNTHESIS AND ANALYSIS **9**

2.1 Introduction 9

2.2 MD Materials Modeling and Design Guidelines 10

2.3 Magneto-Dielectric Composite Material Synthesis and Characterization 18

2.4 Summary 23

CHAPTER 3 CHARACTERIZATION OF MAGNETO-DIELECTRIC MATERIAL **25**

3.1 Introduction 25

3.2 Cavity Perturbation Technique (CPT) 26
3.3 Substrate Integrated Waveguide (SIW) Cavity Design and Simulation 28
3.4 SIW Cavity Resonator Fabrication and Measurements 34
3.5 Magneto-Dielectric Composite Synthesis and Properties Extraction 40
3.6 Analysis of Anisotropic Property 48
3.7 Air Gap Analysis 52
3.8 Summary 53

CHAPTER 4 CAUSAL MODEL DEVELOPMENT FOR EXTRACTED MD MATERIAL PROPERTIES 55

4.1 Introduction 55
4.2 Kramers-Kronig Relations 56
4.3 Modeling of Magneto-Dielectric Material Property 60
4.4 Summary 70

CHAPTER 5 ANTENNA MINIATURIZATION AND SAR REDUCTION 71

5.1 Introduction 71
5.2 Magneto-Dielectric Composite Properties 72
5.3 Microstrip Patch Antenna Design 74
5.4 Planar Inverted-F Antenna (PIFA) Design 80
5.5 Specific Absorption Rate (SAR) reduction techniques 86
5.6 PIFA on MD composite material and SAR reduction 89
5.7 PIFA Fabrication and Measurements 98

5.8 SUMMARY 104

CHAPTER 6 CONCLUSIONS 106

6.1 CONTRIBUTIONS 107

6.2 FUTURE WORK 109

6.3 PUBLICATIONS 110

6.4 INVENTION DISCLOSURE 111

REFERENCES 113

LIST OF TABLES

Table 1. Summary of the literature review for the MD material properties and antenna performance 7

Table 2. MD composite materials design guidelines 17

Table 3. SIW cavity response as varying permittivity/permeability with different sample location. 33

Table 4. SIW Cavity Resonator Specification for Figure 3.2. (Units: mm) 35

Table 5. Extracted permittivity and permeability of sample materials using measurements of 2GHz cavity. 40

Table 6. Parameters of Equation (42) for complex permittivity model. 66

Table 7. Parameters of Equation (42) for complex permeability model. 66

Table 8. Front-to-back ratio of three PIFAs 91

Table 9. Specification of Human head model. 92

Table 10. Specification of human organ tissues [55] 93

Table 11. PIFAs performance with head phantom 94

Table 12. Antenna performance with human leg model 97

Table 13. Specifications and performance (simulated) of $PATCH_{MD}$ and $PIFA_{MD}$ 98

Table 14. Simulated and measured antenna performance for $PIFA_{MD}$. 104

LIST OF FIGURES

Figure 1.1. Examples of antenna miniaturization technique based on the shaping geometry (a) Meander antenna, (b) Slot antenna, (c) Lumped element loading antenna and (d) PIFA. 2

Figure 1.2. Examples of conventional material characterization methods (a) Impedance analyzer method, (b) Two structures method and (c) NRW method. 5

Figure 2.1. Geometry of (a) two-layer particle and (b) composite structure. 10

Figure 2.2. MD composite materials modeling (a) effective permittivity and (b) electric loss tangent. 12

Figure 2.3. Effective permittivity of 2-layer composite from (3) with different core radii, a2, when the oxidized layer = 10nm. 14

Figure 2.4. Effective permittivity of 2-layer composite from (3) with different oxidized layers, a1, when a2=20nm. 14

Figure 2.5. Electric loss tangent of 2-layer composite from (3) with different cobalt-oxide layers, a1, when a2=20nm. 15

Figure 2.6. Effective permeability of composite from (8) with different intrinsic permeabilities. 16

Figure 2.7. Process steps to synthesize MD material. 19

Figure 2.8. XRD spectrum of cobalt-polymer nanocomposites [27]. 20

Figure 2.9. (a) and (b) TEM images of cobalt nanoparticles in cobalt-polymer nanocomposites [26]. 21

Figure 2.10. VSM measurements of hysteresis curve for cobalt-polymer nanocomposites [27]. 22

Figure 2.11. Effect of metal nanoparticle size on nanocomposite (a) permeability, (b) magnetic loss. 23

Figure 3.1. Small material perturbation (a) Original cavity and (b) perturbed cavity. 26

Figure 3.2. Details of SIW cavity resonator (a) perspective view, (b) top view and (c) corner-to-corner probing. 29

Figure 3.3. Field distribution of 1.5 GHz TE_{102} mode SIW cavity resonator and sample insertion location (a) E-field and (b) H-field. 31

Figure 3.4. Field distribution of 2 GHz TE_{103} mode SIW cavity resonator and sample insertion location (a) E-field and (b) H field. 31

Figure 3.5. Return loss simulation with parameter sweep when the sample is at the E-field maximum position (a) ε'_r, (b) μ'_r, (c) electric loss tangent, and (d) magnetic loss tangent. 33

Figure 3.6. Return loss simulation with parameter sweep when the sample is at the H-field maximum position (a) ε'_r, (b) μ'_r, (c) electric loss tangent, and (d) magnetic loss tangent. 34

Figure 3.7. SIW cavity resonators. 35

Figure 3.8. 3.5 GHz SIW cavity resonators with different hole locations for (a) permittivity and (b) permeability measurements. 36

Figure 3.9. Picture of sample preparation. 37

Figure 3.10. Corner-to-corner probe excitation. 37

Figure 3.11. SIW cavity resonator measurements with various samples (a) E-field maximum position and (b) H-field maximum position. 39

Figure 3.12. (a) Picture of synthesized MD composite samples and (b) TEM image of cobalt in fluoropolymer matrix [27]. 41

Figure 3.13. Extracted ε_r' using the CPT with SIW cavity resonators. 42

Figure 3.14. Extracted μ_r' using the CPT with SIW cavity resonators. 43

Figure 3.15. Extracted tanδ_e the CPT with SIW cavity resonators. 43

Figure 3.16. Extracted tanδ_m the CPT with SIW cavity resonators. 44

Figure 3.17. Extracted ε_r' for different density samples B and B' 45

Figure 3.18. Extracted μ_r' for different density samples B and B'. 45

Figure 3.19. Extracted tanδ_e for different density samples B and B' 46

Figure 3.20. Extracted tanδ_m for different density samples B and B' 46

Figure 3.21. Correlation of return loss simulation and measurements of Sample B from permittivity measurements. 47

Figure 3.22. Correlation of return loss simulation and measurements of Sample B from permeability measurements. 48

Figure 3.23. Field vector distribution in SIW cavity (a) E-field and (b) H-field. 49

Figure 3.24. Return loss simulation with parameter sweep (a) $\varepsilon_{x,y,z}$ sweep when the sample is at E-field maximum, (b) $\mu_{x,y,z}$ sweep when the sample is at H-field maximum. 50

Figure 3.25. Return loss measurements of sample C in two directions with (a) 2GHz SIW cavity and (b) 2.5GHz SIW cavity. 51

Figure 3.26. Effect of air gap (a) permittivity measurement and (b) permeability measurement. 52

Figure 4.1. Contour of integration for Equation (31)..... 58

Figure 4.2. Frequency dependence of permittivity calculated with Lorentzian dispersion law with f_{rel} = (a) 2GHz, (b) 4GHz, (c) 6GHz and (d) 8GHz. 61

Figure 4.3. Comparison of Lorentzian and Debye dispersion law when $f_{rel}<f_0$..... 62

Figure 4.4. Real part of A as calculated using Equation (34). 65

Figure 4.5. Imaginary part of A as calculated using Equation (38). 65

Figure 4.6. Complex permittivity modeling for 30% metal loading sample. 67

Figure 4.7. Complex permittivity modeling for 50% metal loading sample. 67

Figure 4.8. Complex permittivity modeling for 70% metal loading sample. 68

Figure 4.9. Complex permeability modeling for 30% metal loading sample. 68

Figure 4.10. Complex permeability modeling for 50% metal loading sample. 69

Figure 4.11. Complex permeability modeling for 70% metal loading sample. 69

Figure 5.1. Extracted (a) real and (b) imaginary part of relative permittivity of MD material. 73

Figure 5.2.Extracted (a) real and (b) imaginary part of relative permeability of MD material. 73

Figure 5.3. Microstrip patch antenna on MD material substrate. 75

Figure 5.4. Microstrip patch antenna on (a) MD and (b) FR4 substrate..... 75

Figure 5.5. Simulated return loss of (a) $PATCH_{MD}$, (b) $PATCH_{DH}$, (c) $PATCH_{DL}$ and (d) $PATCH_{FR4}$..... 77

Figure 5.6. Histogram bandwidth for four microstrip patch antennae..... 78

Figure 5.7. Histogram radiation efficiency for four microstrip patch antennae. 79

Figure 5.8. Histogram gain for four microstrip patch antennae. 79

Figure 5.9. Geometry of the proposed PIFA on MD material substrate (a) top view and (b) side view. 81

Figure 5.10. Antenna size comparison (a) $PIFA_{MD}$ and (b) $PIFA_{FR4}$ 82

Figure 5.11. Simulated return loss of (a) $PIFA_{MD}$, (b) $PIFA_{DH}$, (c) $PIFA_{DL}$ and (d) $PIFA_{FR4}$. 83

Figure 5.12. Histogram bandwidth for four PIFAs. 84

Figure 5.13. Histogram radiation efficiency for four PIFAs. 85

Figure 5.14. Histogram gain for four PIFAs. 85

Figure 5.15. Examples of SAR reduction using EBG structure (a) PIFA [48] and (b) Dual-band coplanar antenna [49]. 87

Figure 5.16. Examples of SAR reduction using metamaterials obtained by (a) split ring resonators (SRRs) [50] and (b) triangular split ring resonators (TSSRs) [51]. 88

Figure 5.17. Cellphone structure for SAR analysis. 89

Figure 5.18. xz-plane radiation patterns of (a) $PIFA_{MD}$, (b) $PIFA_{DL}$ and (c) $PIFA_{FR4}$. 90

Figure 5.19. Picture of human body model of (a) outline drawing [53], (b) SAM head and (c) leg. 92

Figure 5.20. Antenna orientation with SAM phantom mannequin. 93

Figure 5.21. Maximum SAR comparison. 95

Figure 5.22. Modeling of human leg and PIFA. 96

Figure 5.23. Maximum SAR distribution of (a) $PIFA_{MD}$, (b) $PIFA_{DL}$ and (c) $PIFA_{FR4}$. .. 97

Figure 5.24. Pictures of the planar inverted-F antenna on MD material substrate shown in Figure 5.9. 99
Figure 5.25. Picture of antenna under test in anechoic chamber for measurement. 100
Figure 5.26. Simulation and measurement of return loss of the PIFA in Figure. 5.24. .. 101
Figure 5.27. Simulated and measured radiation efficiency of the PIFA in Figure. 5.24. 102
Figure 5.28. Simulated and measured gain of the PIFA in Figure 5.24. 102
Figure 5.29. Simulated and measured radiation pattern of PIFA (a) perspective view, (b) xz-plane and (c) yz-plane. 103
Figure 5.30. Simulated and measured xy-plane radiation patterns in a polar coordinate. 104

SUMMARY

A global trend in the mobile device industry is toward smaller, lighter, and thinner devices. These popular demands have led to the miniaturization of components in a mobile system. The size of the antenna occupies a large part in mobile devices. Mobile devices these days are required to have multiple antennae in one device to cover multiple frequency ranges such as GSM, LTE, WiMAX, WLAN or Wi-Fi. Thus, small antennae with good performance are necessary to meet these demands.

However, decreasing antenna size is very challenging. Not only the antenna dimension is mainly determined by the electrical wavelength, but also the antenna performance is bounded by fundamental limits depending on the size. In this dissertation, magneto-dielectric material, which has both permittivity and permeability greater than unity, has been applied to address the miniaturization challenge. The magneto-dielectric material has captured the interests of antenna designers since this material can reduce the antenna size without deteriorating the antenna's performance significantly. Despite its ability, these materials are not readily available in nature and have to be synthesized by mixing magnetic metal particles with dielectric materials. These synthesized magneto-dielectric composite materials have frequency-dependent permittivity and permeability which determine the antenna performance. Therefore, an accurate method for magneto-dielectric material characterization is needed after material synthesis.

The objective of this dissertation is to develop a material characterization method for magneto-dielectric composite material, and to investigate RF antenna designs using the magneto-dielectric material for different applications. A novel characterization method has

been introduced in this dissertation, and it has been demonstrated through theories, simulations and measurements that it can be used to extract both electric and magnetic properties of the magneto-dielectric material using a single structure. Several antenna designs and configurations on the magneto-dielectric material substrate are discussed, and compared in terms of their performance with other antennae on high dielectric constant material and conventional FR-4 material substrate. An antenna on magneto-dielectric material shows better antenna performance than antenna on high dielectric constant material assuming the two have same antenna size and total material loss. In addition, the size of antenna on the magneto-dielectric material compared to the one on FR-4 material was significantly reduced. In this dissertation, the effect of magnetic loss characteristics on Specific Absorption Rate (SAR) reduction was also investigated. It has been shown that the natural loss characteristics of the magneto-dielectric material can help reduce the SAR of the antenna with no extra structures. Throughout this dissertation, the advantages of utilizing magneto-dielectric material on antenna miniaturization provide a step forward to achieve the global trend in the mobile device industry.

CHAPTER 1

INTRODUCTION

1.1 Background and Motivation

In a short period of time, hand-held mobile devices have become indispensable goods in the life of modern people. Living patterns have rapidly changed with the emergence of smartphones. Consumers can access the Internet in mostly any place along with the development of wireless communication technologies such as cellular communications (3G or LTE) and Wireless Local Area Networks (WLANs). Increasing demands for smaller and thinner mobile devices with a longer battery life and multi-functions have been pushing engineers to achieve integration and miniaturization of multiple parts in systems.

Antenna size is a major obstacle for reducing the overall size of a mobile device since the antenna size is governed by the electrical wavelength. Some mobile devices have multiple antennae in one device in order to translate signals in different frequency range such as GSM 850/900MHz or LTE 1700/2100MHz at once and, therefore, small antennae with good performance are necessary. Antenna miniaturization is very challenging because the antenna performance such as radiation efficiency, bandwidth and gain are limited by the antenna size [1]. These values are directly proportional to the size of antenna. Several methods have been introduced in the literature to reduce the antenna size and these can be separated into two categories. The first category includes the techniques that modify and optimize the antenna geometry to design small antennae. The second category includes the

techniques that load the antenna with high refractive index ($n=(\varepsilon_r \mu_r)^{1/2}$) material where ε_r and μ_r are relative permittivity and permeability respectively.

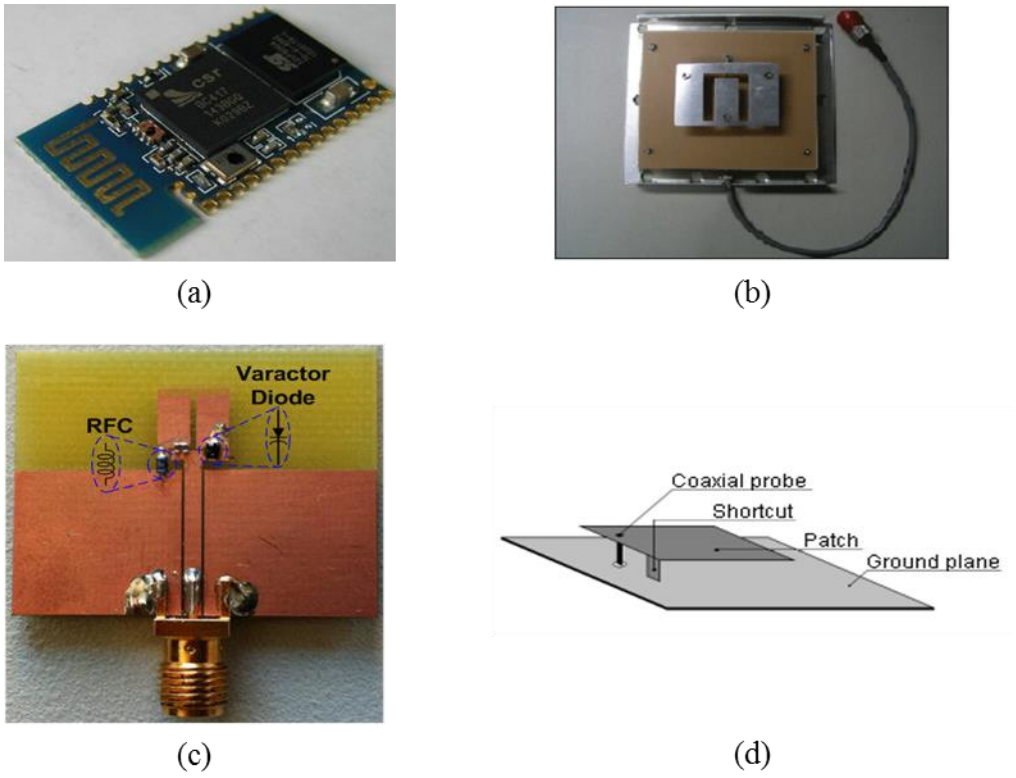

Figure 1.1. Examples of antenna miniaturization technique based on the shaping geometry (a) Meander antenna, (b) Slot antenna, (c) Lumped element loading antenna and (d) PIFA.

Examples of the first group are shown in Figure 1.1. Shaping is the most extensively used technique in antenna miniaturization and many shaping approaches have been considered [2]. Shaping geometry of antenna includes bending, folding, meandering and cutting. Meander line antennae, which reduce the area of antenna by meandering the current path [3], are widely used in many RF applications as shown in Figure 1.1 (a). Cutting slot in the metal patch also increases the current path and results in decreasing the resonant frequency of antenna, as shown in Figure 1.1 (b) [4]. Lumped elements of capacitor and/or inductor can also reduce the antenna size and help to increase the

bandwidth, as shown in Figure 1.1 (c) [5]. Placing a shorting pin next to the feed on planar inverted-F antenna (PIFA) is another technique for reducing the antenna size, as shown in Figure 1.1 (d). PIFA is usually a quarter wavelength resonant antenna, however, its size can be reduced further by properly positioning the shorting pin or folding the patch into multiple layers [2]. These techniques in the first category, however, require a lot of iterations to design the antenna, and the result is a long design period.

Antenna miniaturization techniques in the second category are based on the effect of electromagnetic parameters of material on the antenna size. The electrical wavelength, λ, is inversely proportional to the refractive index value as:

$$\lambda = \frac{c}{f_r \sqrt{\varepsilon_r \mu_r}}, \tag{1}$$

where c is the speed of light and f_r is the resonant frequency of the antenna. The material property can determine the size of the antenna for a given resonant frequency. High dielectric constant material for antenna substrate or superstrate has been used for antenna miniaturization in the literature [6]-[8]. Increasing the relative permittivity of the substrate material, however, suffers from narrow bandwidth and low efficiency. These disadvantages are derived from the fact that the electric field remains in the high permittivity region and does not radiate. The low characteristic impedance in the high permittivity medium results in a problem for impedance matching as well [9].

On the contrary, magneto-dielectric (MD) materials, which have ε_r and μ_r greater than one, can reduce the antenna size with better antenna performance compared to the antenna on a high dielectric constant material [10]. According to the work of Hansen and Burke in [11], properly increasing the relative permeability leads to efficient size reduction of microstrip antennas. The impedance bandwidth can be retained after the miniaturization.

Niamien *et al*. in [12] proposed closed-form formulae for calculating the radiation efficiency and bandwidth of the patch antenna over lossy MD material using the cavity model. Based on the formulae, relative permittivity has a negative impact on the radiation efficiency and bandwidth, while relative permeability has a positive impact on both of them. Various antenna designs on MD materials have been introduced in [13]-[16] and it was observed that the antenna size was reduced without losing the radiation efficiency and bandwidth of the antenna. These MD materials have therefore raised hope for antenna miniaturization without deteriorating antenna performance.

MD materials are not available readily in nature and they need to be realized through material synthesis. An accurate material property characterization method is necessary for the synthesized MD material since the antenna response is affected by the frequency dependent permittivity and permeability of the material. Both permittivity and permeability are complex numbers, which can be expressed as:

$$\begin{aligned} \varepsilon_r &= \varepsilon' - j\varepsilon'', \\ \mu_r &= \mu' - j\mu''. \end{aligned} \tag{2}$$

Separating the dielectric properties from the magnetic properties during measurements is challenging, and these MD material properties can be extracted using some conventional methods, as shown in Figure 1.2. Two different structures have been used to solve the challenge in [17], [18]. One of the two structures is mostly sensitive to the change in dielectric properties while the other is sensitive to changes in magnetic properties. The method discussed in [17] uses a commercially available impedance analyzer connected to a material fixture as shown in Figure 1.2 (a). A circular disk sample is used for the permittivity measurement, and a toroid shape sample is used for the permeability measurement. This method can give accurate MD material properties. It requires, however,

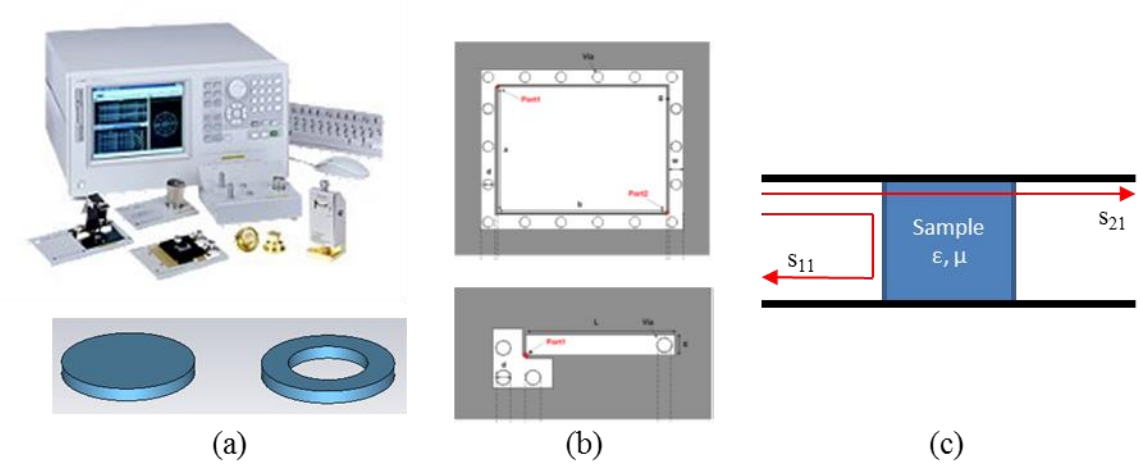

Figure 1.2. Examples of conventional material characterization methods (a) Impedance analyzer method, (b) Two structures method and (c) NRW method.

two different shape samples, and it can only measure up to a frequency of 1GHz. Altunyurt *et al*. in [18] also used the method with two different structures to extract the electric and magnetic properties of MD material, as shown in Figure 1.2 (b). MD material was used as the substrate of the parallel plate cavity resonator, which was used for the permittivity measurement, and a strip inductor was used for the permeability measurement. Another common method for material property measurement is called Nicolson-Ross-Weir (NRW) method [19]. This method is based on the S-parameter measurements of a loaded rectangular or circular waveguide as shown in Figure 1.2 (c). The normal reflection and transmission coefficients are measured with a sample located inside of the waveguide. The dielectric and magnetic properties of the sample is calculated using these coefficients. These methods, however, require machinable solid materials or a large amount of MD material sample to fabricate the substrate. As a result, accurate and simpler material characterization methods are required.

For antenna miniaturization, the MD material needs to have high and stable permeability with low loss in the frequency band of interest. Recently, MD composite

materials using ferrites/hexaferrites and their composites with polymer have been characterized for RF antenna applications [20]-[23]. Shin *et al*. have designed a monopole antenna using ferrite for 700 MHz LTE band [20]. The antenna showed a low radiation efficiency of 27.9% due to the high magnetic loss of 0.189. Y-type hexagonal ferrites with glass or polymer have been used to realize MD material in [21] and [22]. These MD composites showed permeability of ~2 with low magnetic loss at 0.8 ~ 1GHz. With this low loss, antennae in [21] and [22] showed improved radiation efficiencies of 43 and 65% respectively. Park *et al*. in [24] used a MD composite by blending ferrite powder and epoxy which showed permeability of 1.56 with loss of 0.035 at 800MHz. Around 47 - 82% radiation efficiency was measured over the frequency band of 748 – 960MHz. The high radiation efficiency can be due to small refractive index and low loss but it is not good for reducing antenna size. The thickness of MD composite materials were 3mm which is too thick for mobile devices. Therefore, antenna designs on thinner MD composite material with reasonable antenna performance are required. The MD material properties and antenna performance discussed in [20]-[23] are summarized in Table 1.

Table 1. Summary of the literature review for the MD material properties and antenna performance

Material	Permittivity ($\varepsilon_r/\tan\delta_e$)	Permeability ($\mu_r/\tan\delta_m$)	Frequency	Gain (dBi)	Radiation Efficiency (%)	Year
Ferrite compound	3.29/ 0.027	2.01/ 0.189	780MHz	-5.1	27.9	2010 [20]
Y-type hexagonal ferrite + glass	12.7/ 0.0065	2.1/ 0.0474	800MHz	-0.03	43	2012 [21]
Y-type hexagonal ferrite + polymer	5.07/ 0.004	2.01/ 0.03	1GHz	N/A	65 (Simulation)	2014 [22]
Ferrite + epoxy	4.18/ 0.022	1.56/ 0.035	748 – 960 MHz	2.12	82	2014 [23]

1.2 Contributions

The major contributions of the dissertation are the following:

1) Characterization of magneto-dielectric composite materials using a cavity perturbation technique with substrate integrated waveguide cavity resonators.
2) Development of a causal model for capturing the extracted magneto-dielectric properties from the proposed material characterization method.
3) Design and fabrication of planar inverted-F antenna on magneto-dielectric material substrate and analysis of antenna performance comparing antennae on different substrate.
4) Analysis of the reduction of specific absorption rate using magneto-dielectric materials for RF antenna applications.

1.3 Organization of the Dissertation

The rest of this dissertation is organized as follows: Chapter 2 describes magneto-dielectric material synthesis, and composite mixing rules to predict the electric and magnetic properties of synthesized composite materials. In Chapter 3, the cavity perturbation technique with a substrate integrated waveguide cavity resonator to extract material properties of the synthesized MD samples is presented. A fitting model for the measured MD material properties is developed and Kramers-Kronig relations are used to demonstrate the causality of the model in Chapter 4. Chapter 5 discusses antenna designs using magneto-dielectric material, and also the analysis of specific absorption rate for magneto-dielectric material based antenna is discussed. Finally, summary and conclusions of this dissertation are presented in Chapter 6.

CHAPTER 2

MAGNETO-DIELECTRIC COMPOSITE MATERIAL SYNTHESIS AND ANALYSIS

2.1 Introduction

This chapter presents a material synthesis procedure for realizing magneto-dielectric materials for RF antenna applications. Mixing rules that can estimate permittivity and permeability of the composite material from its components are described to find the right mixture of components for effective antenna miniaturization. As described in Chapter 1, materials with a relative permeability larger than one can offer better promise in antenna miniaturization than materials with a high dielectric constant only. In recent years, engineered metamaterials, which consist of periodic structures, have been used to obtain relative permeability greater than one. The metamaterials, however, suffer from undesired performance such as narrow bandwidth, and require extra substrate layers which make it bulky and oppose the miniaturization goal.

Researchers have been studying magneto-dielectric material synthesis to achieve the desired values of permittivity and permeability to achieve the goal of antenna size reduction without deteriorating antenna performance. In this chapter, first principles describing the methodology used for MD material synthesis are presented. A combination of mixing theories and models are used to find the correct mixture of composite material components in order to maximize the advantages of MD material usage for RF antenna applications.

2.2 MD Materials Modeling and Design Guidelines

The MD composite material which is not readily available in nature is realized through mixing magnetic materials with dielectric materials. In this chapter, nickel and cobalt were considered for the magnetic material and epoxy and fluoropolymer were considered for the dielectric materials. This section discusses how the right mixture of candidate components in the composite were chosen to achieve the desired MD composite material properties. To reduce antenna size with reasonable effect on antenna performance, the synthesized MD composite materials should be designed for high permeability and reasonable permittivity. In addition both electric and magnetic loss of the MD composite material should be low as possible. The properties of composites from their individual components can be predicted using "Effective Medium Theories" (EMTs) or mixing rules. These models can be used to estimate permittivity and permeability of MD composite materials containing metal and dielectric materials.

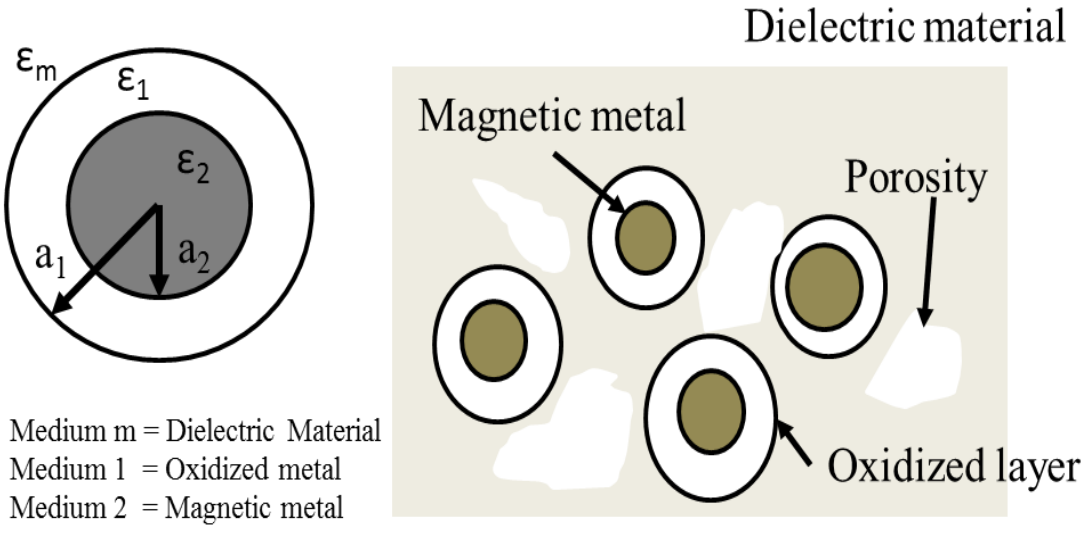

Figure 2.1. Geometry of (a) two-layer particle and (b) composite structure.

For the effective permittivity prediction, Sihvola and Lindell's mixing rule for an N-layer spherical filler particle, in which the Rayleigh mixing formula is generalized to deal with layered filler particles, can be used [24]. As shown in Figure 2.1 (a), the metal-dielectric material system was considered as a two-layer particle. The nano-sized metal particle is encapsulated with the metal-oxidation layer and it is mixed in a dielectric material, as shown in Figure 2.1 (b). Sihvola and Lindell's mixing rule for 2-layers can be expressed as:

$$\frac{\varepsilon_{eff}-\varepsilon_m}{\varepsilon_{eff}+2\varepsilon_m}=V_f\frac{(\varepsilon_1-\varepsilon_m)+(2\varepsilon_1+\varepsilon_m)\cdot g_2(\varepsilon_i,a_i)}{(\varepsilon_1+2\varepsilon_m)+(2\varepsilon_1-\varepsilon_m)\cdot g_2(\varepsilon_i,a_i)},i\in[1,2] \tag{3}$$

where V_f is the volume fraction of metal filler and

$$g_2=\frac{(\varepsilon_2-\varepsilon_1)}{(\varepsilon_2+2\varepsilon_1)}\left(\frac{a_2}{a_1}\right)^3. \tag{4}$$

This equation can be simplified for ε_{eff} as:

$$\varepsilon_{eff}=\frac{\varepsilon_m(1+2A)}{(1-A)}, \tag{5}$$

where A is the right-hand term in Equation (5). To estimate the permittivity of the metal particle (ε_2), a Drude model was used as:

$$\varepsilon_2=1-j\frac{\sigma}{\omega\varepsilon_0}, \tag{6}$$

where σ is the conductivity, and ω and ε_0 are the angular frequency and permittivity of free space, respectively.

All four possible combinations of metal-dielectric material using Ni, Co, epoxy and fluoropolymer were modeled using the Sihvola and Lindell mixing model to find a right combination that satisfies the material design specifications. Conductivity of Ni and Co

were assumed as 50 and 79 S/m and permittivity of nickel-oxide and cobalt oxide were assumed as 12 and 10, respectively. Permittivity of epoxy and fluoropolymer were estimated as 4 and 2 respectively. Loss tangent of the epoxy and fluoropolymer are around 0.011 and 0.005 respectively and they were assumed to be constant with frequency. Figure 2.2 shows the predicted effective permittivities and electric loss tangents of the four metal-dielectric material combinations.

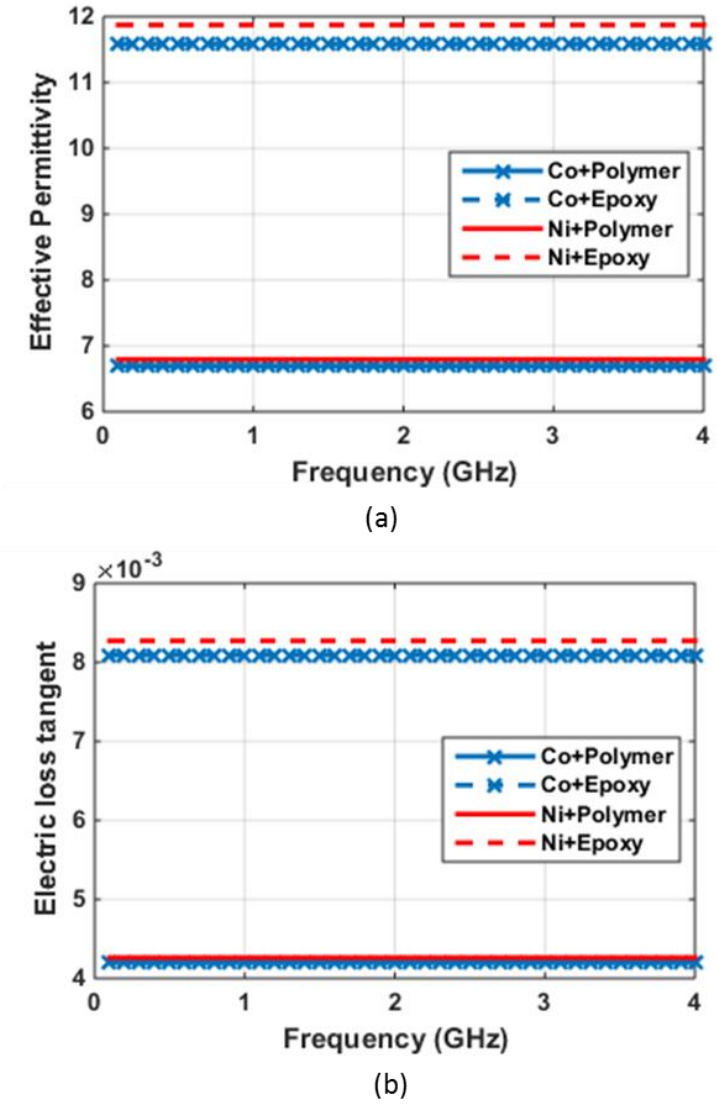

Figure 2.2. MD composite materials modeling (a) effective permittivity and (b) electric loss tangent.

Composite materials using the fluoropolymer shows lower effective permittivity and loss tangent than composite materials using epoxy, as shown in Figure 2.2. MD composite materials used show a permeability of ~2 in the RF frequency range and MD composite materials with permittivity close to permeability are preferable for antenna applications. Therefore the fluoropolymer material was selected as the dielectric in this work. Between Ni and Co, Co-fluoropolymer shows slightly lower effective permittivity and loss than Ni-fluoropolymer, as shown in Figure 2.2. So cobalt was selected as the metal particle. The cobalt metal particle is also preferable for achieving higher permeability than nickel metal particle, as discussed later.

Other design factors such as metal volume fraction and radii of particles that determine the effective permittivity of Co-fluoropolymer have also been studied. Figure 2.3 shows the effective permittivity of the composite material as a function of the volume fraction of filler. It is observed that the radius of the cobalt particle, a2 is directly proportional to the effective permittivity. On the other hand, when the oxidized layer, a1, increases, the effective permittivity of the composite material decreases, as shown in Figure 2.4. According to these figures, the effective permittivity of the composite is also directly proportional to the volume fraction of metal filler.

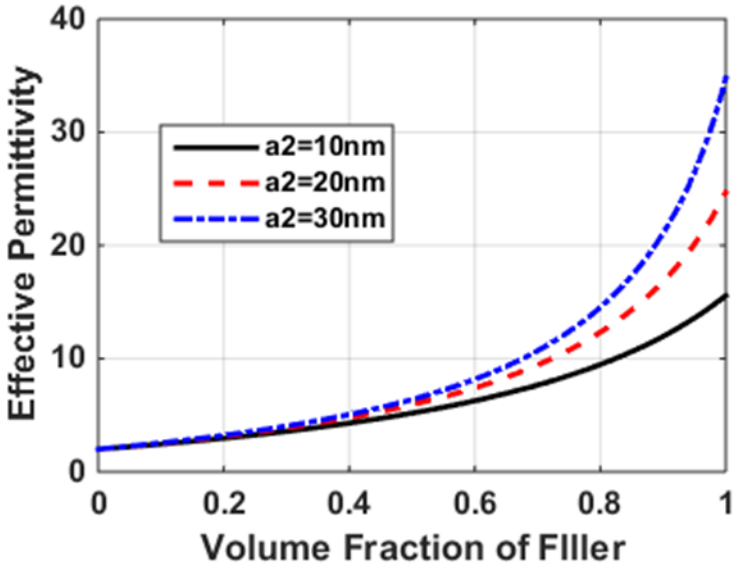

Figure 2.3. Effective permittivity of 2-layer composite from (3) with different core radii, a2, when the oxidized layer = 10nm.

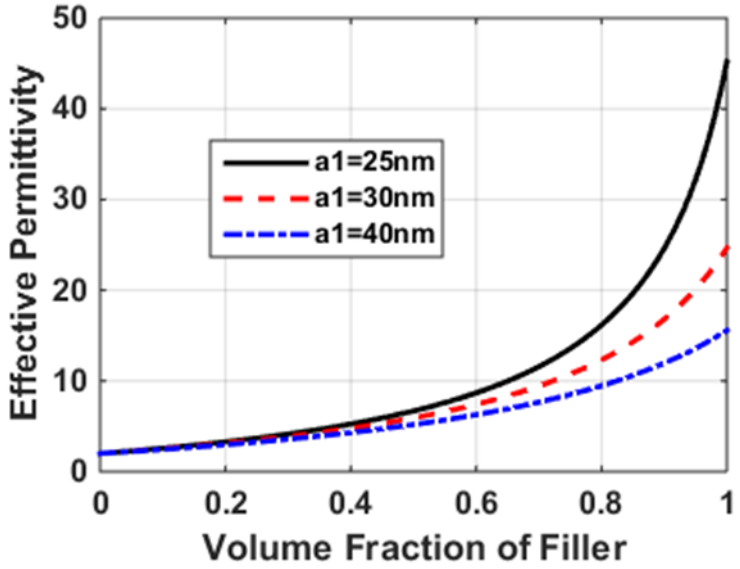

Figure 2.4. Effective permittivity of 2-layer composite from (3) with different oxidized layers, a1, when a2=20nm.

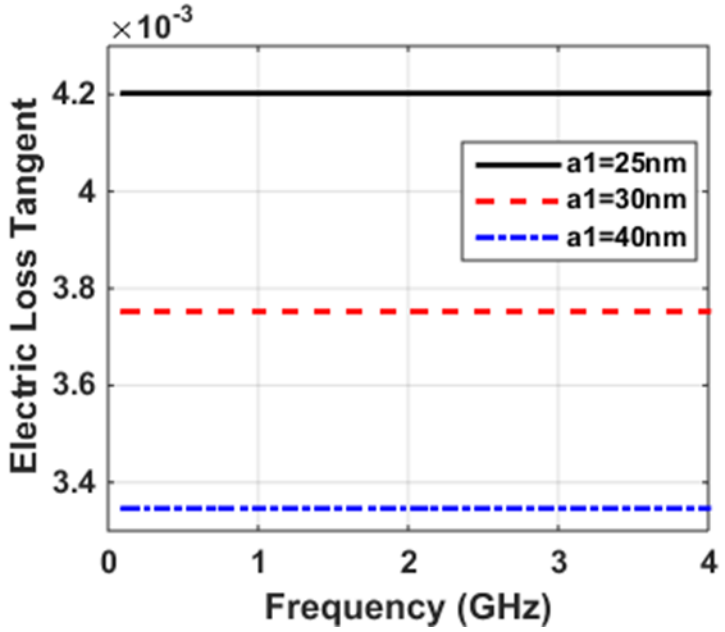

Figure 2.5. Electric loss tangent of 2-layer composite from (3) with different cobalt-oxide layers, a1, when a2=20nm.

Figure 2.5 shows the electric loss tangent of the composite materials as a function of frequency. It was observed that increasing the cobalt-oxide layer thickness decreases the electric loss tangent. According to these results, the effective permittivity of MD composite materials can be managed to desired values by controlling the metal volume fraction, size of the metal core particles, oxidization layer thickness and dielectric constant and loss tangent of the polymer matrix.

For effective permeability modeling, the most common mixing rules, namely Bruggeman's effective medium theory, was used [25], which is given by:

$$V_f \frac{\mu_a - \mu_{eff}}{\mu_a + 2\mu_{eff}} + \left(1 - V_f\right) \frac{1 - \mu_{eff}}{1 + 2\mu_{eff}} = 0, \tag{7}$$

where μ_a is the intrinsic permeability and Equation (7) can be simplified for μ_{eff} as:

$$\mu_{eff} = \mathrm{X} + \sqrt{\mathrm{X}^2 + \frac{\mu_a}{2}},$$
$$\mathrm{X} = \frac{3V_f\mu_a - 3V_f - \mu_a + 2}{4}. \tag{8}$$

The effective permeability of a composite material for various intrinsic permeabilities are shown in Figure 2.6. The effective permeability shows a direct relationship with the volume fraction of filler and higher intrinsic permeability results in higher effective permeability as well.

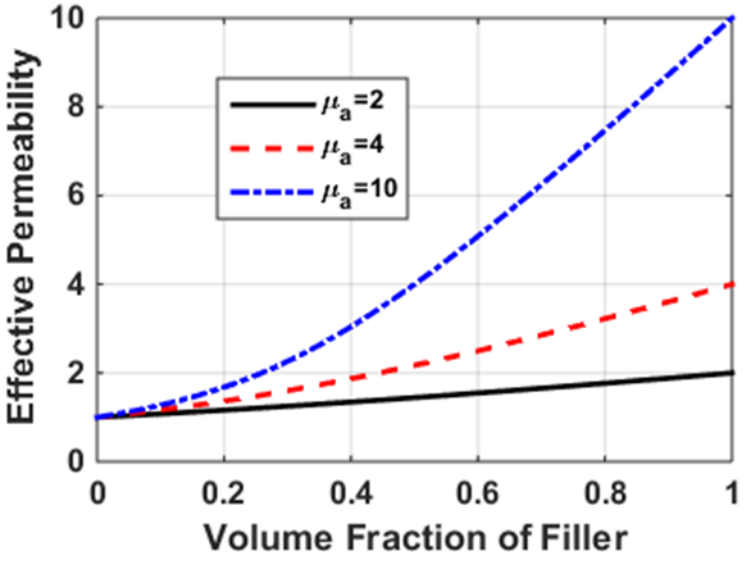

Figure 2.6. Effective permeability of composite from (8) with different intrinsic permeabilities.

A high saturation magnetization (Ms) is required to increase the permeability of MD composite materials. The ideal Ms for cobalt is 162 emu/gm while that for nickel is 58 emu/gm [26], therefore cobalt metal particle is better metal candidate than nickel metal particle for synthesizing the MD composite materials.

Reducing magnetic loss of MD composite materials is a huge challenge during MD material synthesis. The magnetic losses are attributed to various sources. For large metal

particles, eddy current losses significantly contribute to total losses. When the particle size exceeds a critical dimension, domain walls are formed within the particle. The domain wall resonance also contributes to losses. Losses are further increased as the frequency reaches the ferromagnetic resonance (FMR) [27]. These losses from eddy current and domain wall can be eliminated by reducing the particle size to nanoscale and for nanocomposites, the FMR is related to the effective field anisotropy, represented as [27]:

$$FMR = \frac{\gamma}{2\pi} H_{eff}, \tag{9}$$

where γ is the gyromagnetic ratio and H_{eff} is the effective field anisotropy. A magnetic metal needs to have high effective field anisotropy to increase the resonance. The FMR is estimated to reach 4GHz for cobalt nanocomposites while that for nickel it is 2GHz [27]. Based on these modeling results, MD composite material design guidelines can be provided, as summarized in Table 2.

Table 2. MD composite materials design guidelines

Specification	Design Guidelines
High permeability	Higher saturation magnetization (Ms) Higher filler volume fraction
Low magnetic loss tangent	Nanoparticle Higher effective field anisotropy
Reasonable permittivity	Low permittivity polymer matrix Moderate filler content
Low dielectric loss tangent	Low loss polymer matrix Finer particles

According to these guidelines, cobalt nanoparticle has been selected as the metal particle since it has high saturation magnetization and high effective field anisotropy while fluoropolymer is selected for dielectric polymer because it has low dielectric constant and

low loss. A particle size of 20~30 nm with a reasonable volume fraction of 30% or higher is desired.

2.3 Magneto-Dielectric Composite Material Synthesis and Characterization

The magneto-dielectric material investigated in this thesis is based on the metal-polymer composite that has been synthesized by the Packaging Research Center (PRC) at Georgia Tech. The MD material is synthesized by combining nano-sized cobalt metal particles in a fluoropolymer matrix. This MD composite material is a ferromagnetic material which is a permanent magnetic material without the external H field. Fluoropolymer has been selected since it has a low dielectric constant as well as low electric loss tangent which can help antenna performance. Magnetic nanocomposites provide several advantages for RF antenna applications such as: a) low eddy current and domain wall losses from nanoscale particle size and b) high frequency-stability because of various contributions from magnetic anisotropies that enhance the ferromagnetic resonance frequency (FMR). They also show enhanced permittivity with low loss for further antenna miniaturization and performance enhancement. They suffer, however, from several limitations which result in suppression of permeability and enhanced damping, leading to higher losses over a broad frequency range [27].

The synthesis process followed in this thesis is based on a sol-gel process where oxidized cobalt nanoparticles are milled with fluoropolymer to create a paste. Figure 2.7. shows a flow chart of the material synthesis and sample preparation process. The partially-oxide-passivated cobalt nanoparticles were obtained as an aggregated hard metal. The aggregated cobalt particles are broken down to their primary particle sizes of about

20~30nm using a ball-milling process. The received metal powders were suspended in anhydrous toluene solvent and milled for 10-15 hours with zirconia balls to break the

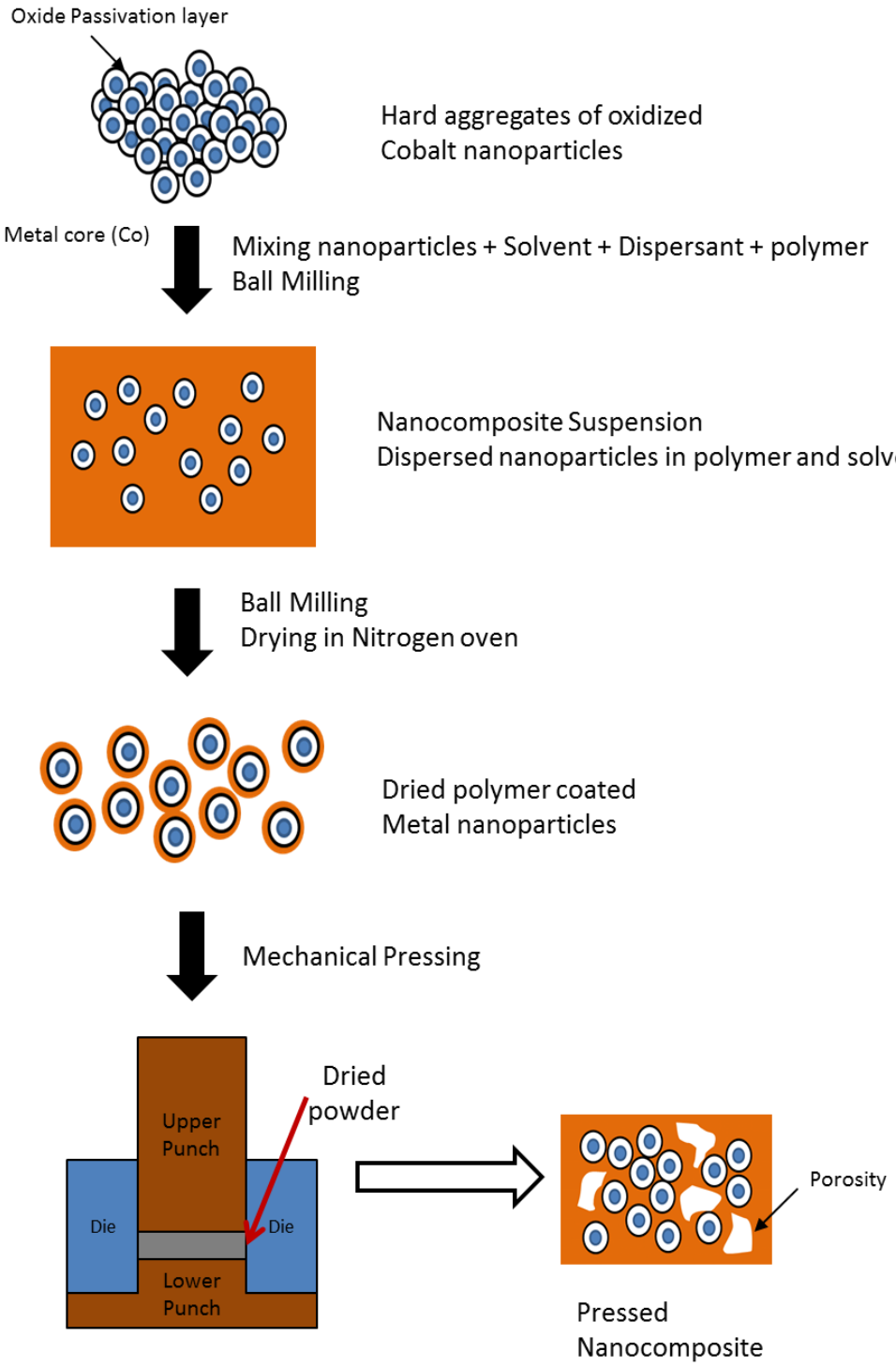

Figure 2.7. Process steps to synthesize MD material.

aggregates. The ALX fluoropolymer was then added to the suspension and milled again for 4-6 hours to ensure complete homogenization of the polymer and the metal particles. The final polymer-metal slurry was dried into a powder at 80 ℃ for 30 minutes in a nitrogen atmosphere. The dried metal-polymer composite powder was compacted using a mechanical hydraulic press. Several samples were fabricated with different mixtures of contents to demonstrate their effect on material properties. The characterization method used to extract the electric properties of the synthesized MD material is described in Chapter 3.

After material synthesis, the morphology and crystal structure were characterized through X-ray Diffraction (XRD) (Philips 1813 diffractometer) and Transmission Electron Microscopy (TEM) (TEM 100CX) to confirm the nanostructure [27]. The XRD spectrum of cobalt nanoparticles embedded in the polymer matrix is shown in Figure 2.8.

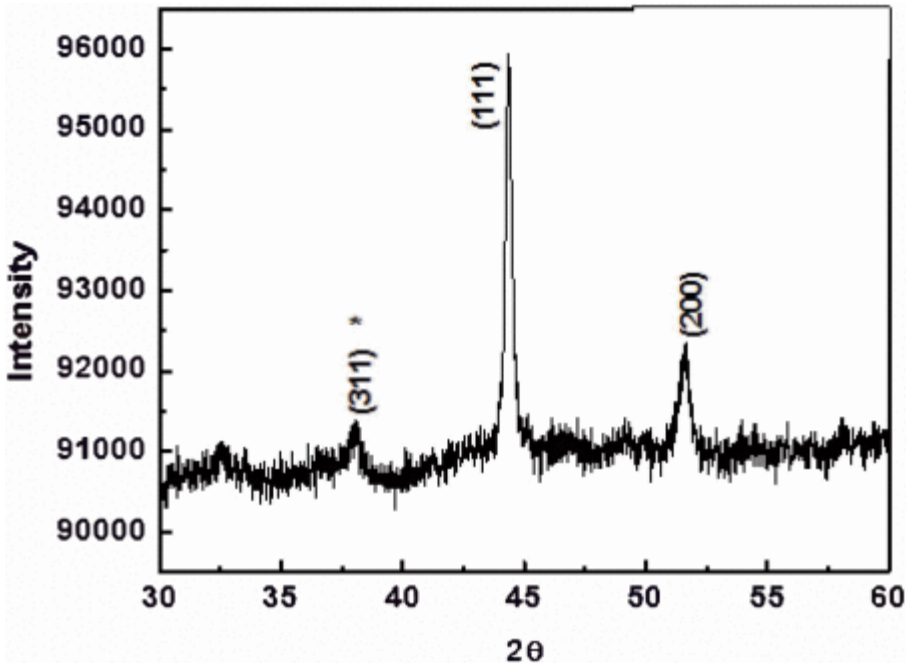

Figure 2.8. XRD spectrum of cobalt-polymer nanocomposites [27].

This spectrum indicates that the average crystallite size is 25~30 nm for cobalt particles. The peak matched with the (111), (200) and (220) planes of face-centered-cubic (fcc) metallic cobalt. A weak peak at 38 ° corresponds to cobalt oxide and it indicates a thin oxidized layer on the metal core. The size of the cobalt nanoparticles are consistent with the TEM images shown in Figure 2.9.

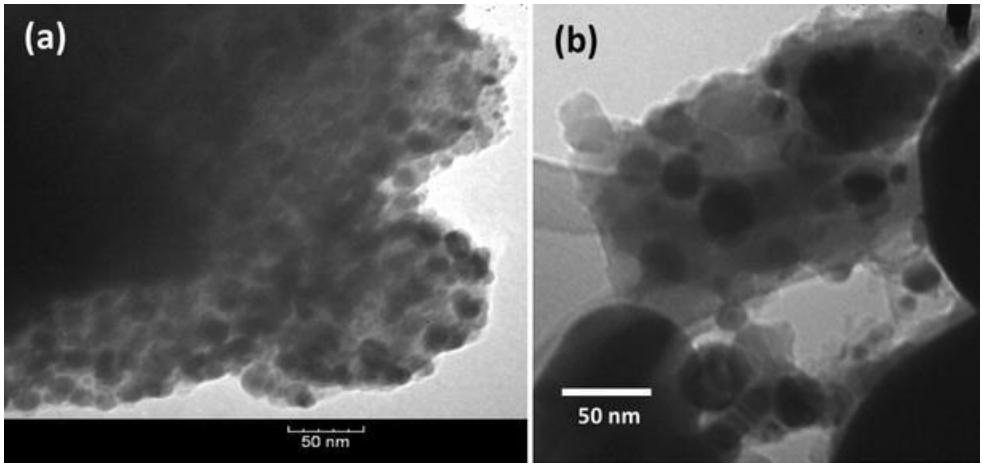

Figure 2.9. (a) and (b) TEM images of cobalt nanoparticles in cobalt-polymer nanocomposites [26].

The fine spherical cobalt nanoparticles were dispersed well in a polymer matrix and compacted to form a nanocomposite, as shown in Figure 2.9 (a). Certain levels of particle agglomeration are also observed from Figure 2.9 (b).

The hysteresis curve was measured with a vibration sample magnetometer (VSM) (Lakeshore 736 Series) to obtain the effective saturation magnetization (Ms) and coercivity, as shown in Figure 2.10 [27].

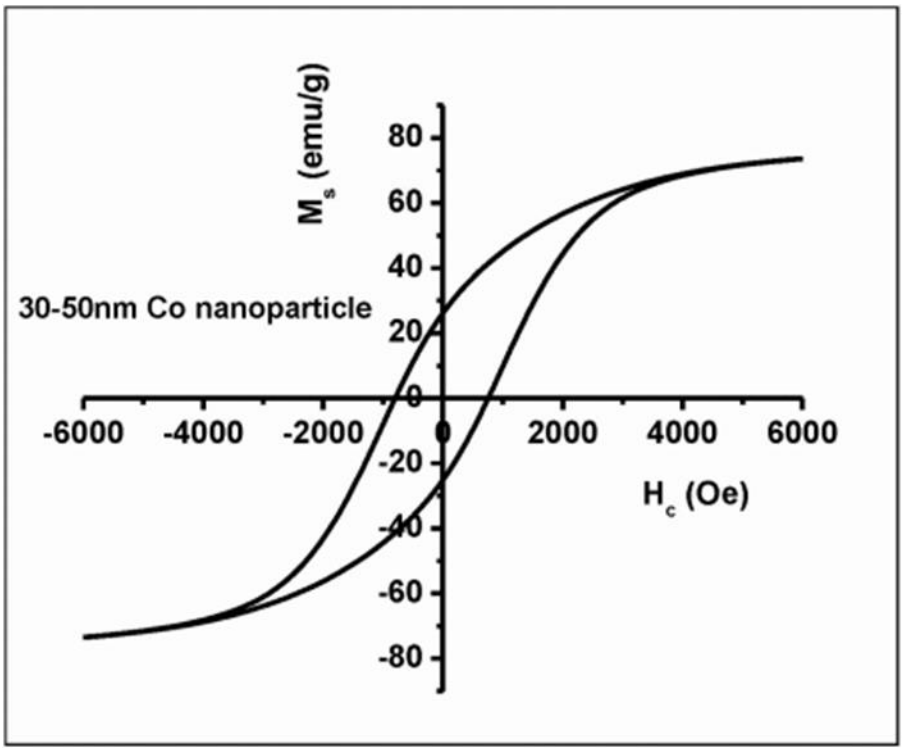

Figure 2.10. VSM measurements of hysteresis curve for cobalt-polymer nanocomposites [27].

The coercivity of 800 Oe and Ms of 70 emu/g were measured form the VSM measurements. The theoretical Ms of a nanocomposite with 90 wt.% metal is approximately 144 emu/g, and this indicates that approximately 50 wt.% of the powder weight is converted to cobalt oxide that does not contribute to the Ms. The cobalt oxide shell provide several benefits by acting as an insulating passivation that prevents eddy current losses [27].

Pulugurtha *et al*. in [26] have shown permeability and magnetic loss measurements of nanocomposite using various sizes of cobalt particles, as shown in Figure 2.11. When the size of the cobalt is 25-40 nm, the nanocomposite showed a stable response while 100 nm Ni nanoparticle composite showed an unstable response as frequency increased.

Therefore, Co nanoparticle is a good candidate for composite material especially at higher frequencies where stability of the material properties is desired.

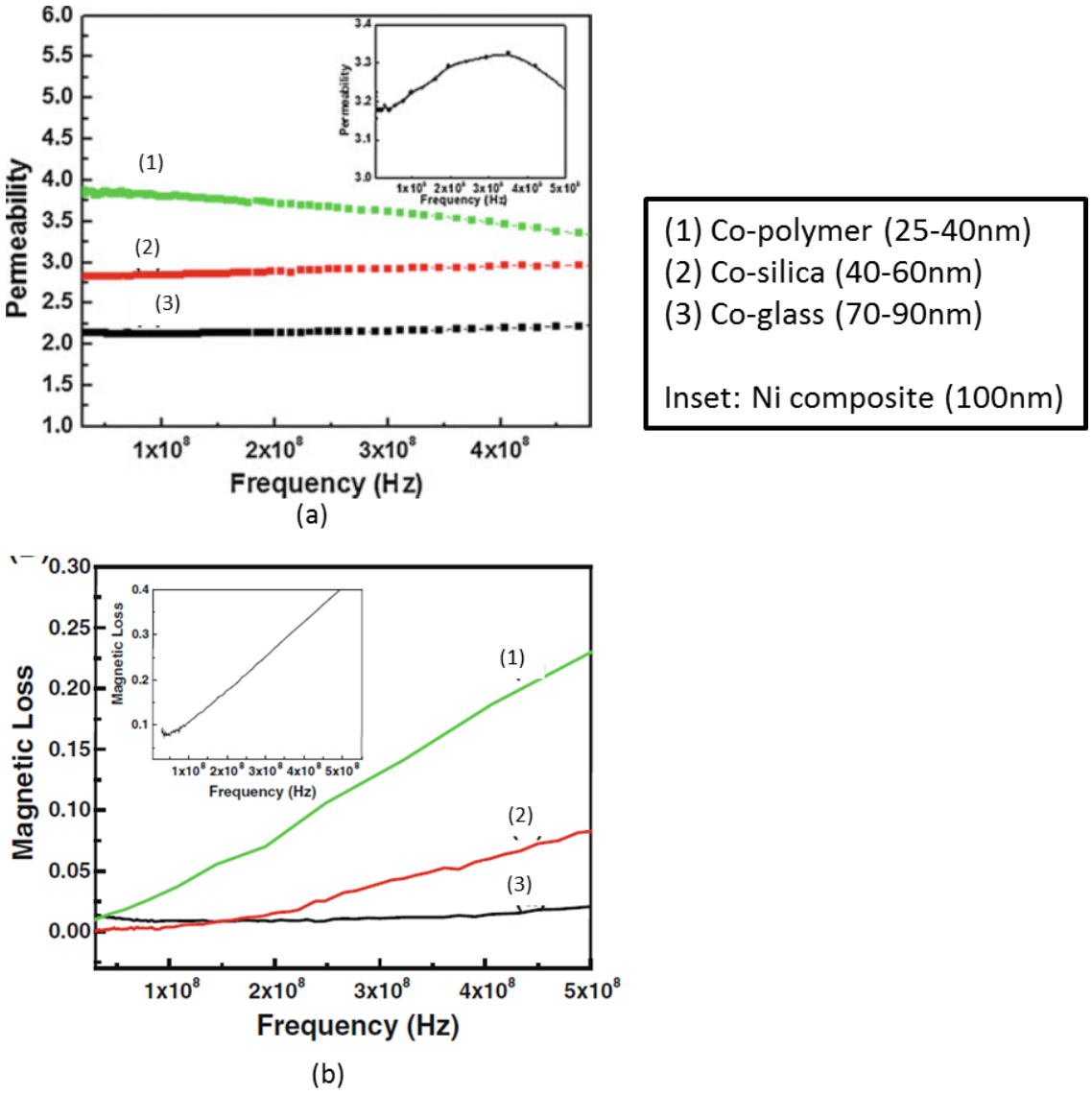

Figure 2.11. Effect of metal nanoparticle size on nanocomposite (a) permeability, (b) magnetic loss.

2.4 Summary

This chapter presents design guidelines and a material synthesis procedure to realize MD composite materials using metal-polymer composites. X-ray Diffraction (XRD) and Transmission Electron Microscopy (TEM) have been used to characterize the

microstructure of synthesized magneto-dielectric materials using cobalt-fluoropolymer. The average size of the cobalt nanoparticle is 25~40 nm and results from XRD and TEM showed good correlation. Hysteresis curves using Vibration Sample Magnetometer (VSM) have been measured to obtain the saturation magnetization (Ms) of the MD composite materials. The motivation for using cobalt nanoparticles in the nanocomposite arises from their superior effective field anisotropy and high saturation magnetization which directly relate to the frequency stability [26]. The Co nanoparticles can enhance the ferromagnetic resonance (FMR) with their high Ms property. The combination of Bruggeman's effective medium model and the Sihvola and Lindell model were used to understand the role of metal particle size, oxide passivation and volume fraction of metal filler for determining the material properties. Through theoretical modeling, it is shown that material properties of a cobalt-fluoropolymer composite can be predicted and controlled.

CHAPTER 3

CHARACTERIZATION OF MAGNETO-DIELECTRIC MATERIAL

3.1 Introduction

This chapter presents the characterization method of MD composite materials. MD materials have to be realized through material synthesis where magnetic metal particles are combined with dielectric materials, since they are not available readily in nature. As new composites are synthesized and since antenna response is determined by the frequency dependent properties (ε', ε", μ' and μ") of the material, an accurate measurement method is required to extract them. It is challenging to differentiate electric properties from magnetic properties during extraction. Conventional methods to achieve this task typically use two different structures [17], [18]. One of them is mostly sensitive to the change in electric properties while the other structure is sensitive to the change in magnetic properties of the material.

A novel material characterization method which is based on a cavity perturbation technique (CPT) with a substrate integrated waveguide (SIW) cavity resonator is presented for extracting the properties of MD materials. Throughout the simulations and measurement, it has been demonstrated that this method can extract both electric and magnetic properties with a single SIW structure. Effect of both metal loading and material density are discussed in this chapter. In addition, an analysis of the anisotropic property of composite materials along with details of sample size are described in this chapter.

3.2 Cavity Perturbation Technique (CPT)

The CPT material characterization method has been widely used for extracting electromagnetic properties of various materials. It works well for the measurement of low-loss and medium loss materials, however, this method is less useful for extremely low-loss samples [28]. This method is effective for MD material characterization since MD composite materials usually show moderate loss in the RF frequency band of interest. To apply the cavity perturbation technique for material characterization, a sample with permittivity, ε_2, and permeability, μ_2, is inserted into the cavity as shown in Figure 3.1.

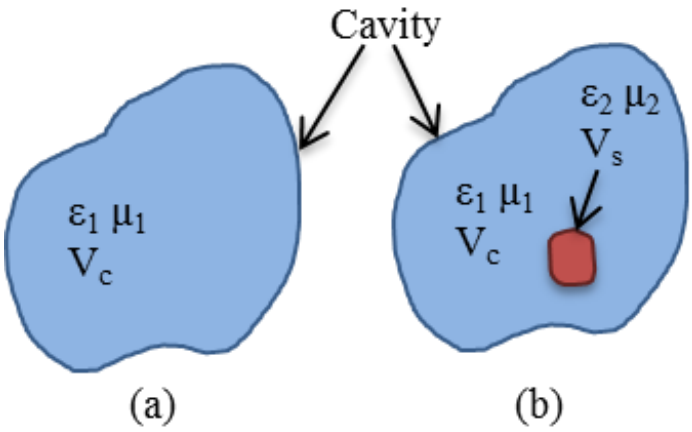

Figure 3.1. Small material perturbation (a) Original cavity and (b) perturbed cavity.

As the sample is introduced into a resonator, the properties of the sample can be extracted from changes in the resonant frequency and quality factor of the resonator caused by the sample. The fundamental expression of CPT is [28]:

$$\frac{f_2 - f_1}{f_1} = -\frac{\int_{V_s} \left(\Delta\varepsilon E_2 \cdot E_1^* + \Delta\mu H_2 \cdot H_1^* \right) dV}{\int_{V_c} \left(\varepsilon_1 E_2 \cdot E_1^* + \mu_1 H_2 \cdot H_1^* \right) dV}, \tag{10}$$

with

$$\Delta\varepsilon = \varepsilon_2 - \varepsilon_1, \tag{11}$$

$$\Delta\mu = \mu_2 - \mu_1, \tag{12}$$

where f_1 and f_2 are the resonant frequencies before and after the introduction of the sample, as shown in Figure 3.1. In (11) and (12), ε_1 and ε_2 are the complex permittivities of the original medium in the cavity and sample respectively, and μ_1 and μ_2 are the complex permeabilities of the original medium in the cavity and sample respectively. Likewise, E_1 and E_2 are the electric fields in the cavity before and after perturbation, and H_1 and H_2 are the magnetic fields in the cavity before and after perturbation, respectively. In (10), V_c and V_s are the volumes of the cavity and sample respectively.

For a complex permittivity measurement, the sample is introduced at a location where the electric field is maximum in the cavity. From [29], Equation (10) can be rewritten as a modified CPT formulae as:

$$\varepsilon_s' = \frac{A\varepsilon_r' V_c}{V_s}\left(\frac{f_o - f_s}{f_s}\right) + \varepsilon_r', \tag{13}$$

$$\varepsilon_s'' = \frac{BV_c}{V_s}\left(\frac{\varepsilon_r'^2 + \varepsilon_r''^2}{\varepsilon_r'}\right)\left(\frac{Q_o - Q_s}{Q_s Q_o}\right) + \frac{\varepsilon_s'\varepsilon_r''}{\varepsilon_r''}, \tag{14}$$

where ε'_s and ε''_s correspond to the real and imaginary parts of the permittivity of the sample, respectively; ε'_r and ε''_r are the real and imaginary parts of the relative permittivity of cavity medium, respectively; Q_o and Q_s are the quality factors of the empty cavity and the cavity with the loaded sample respectively; and f_o and f_s are the resonant frequencies before and after the sample perturbation, respectively. In (13) and (14), constants A and B are obtained through calibration using a standard sample with known permittivity.

Similarly, for complex permeability measurements, the sample is inserted where the magnetic field is maximum in the cavity and (15) and (16) can be used for calculating the complex permeability [28].

$$\mu_s' = \frac{CV_c}{V_s}\left(\frac{f_o - f_s}{f_s}\right) + 1, \tag{15}$$

$$\mu_s'' = \frac{DV_c}{V_s}\left(\frac{Q_o - Q_s}{Q_s Q_o}\right), \tag{16}$$

where μ'_s and μ''_s are the real and imaginary parts of the permeability of the inserted sample respectively. Constants C and D in equations (15) and (16) are also obtained from the measurement of standard sample with known permeability.

3.3 Substrate Integrated Waveguide (SIW) Cavity Design and Simulation

SIW technology was used to fabricate the cavity for CPT measurements. The SIW has been realized using a planar substrate and it has been used to measure the complex permittivity of liquid and dielectric materials in [29] and [30] with the advantage of obtaining high accuracy from high quality factor, low profile and minimum radiation effect. In this chapter, this method has been extended for measuring both complex permittivity and permeability of MD composite materials for the first time. A cavity resonator with SIW technology is designed as shown in Figure 3.2.

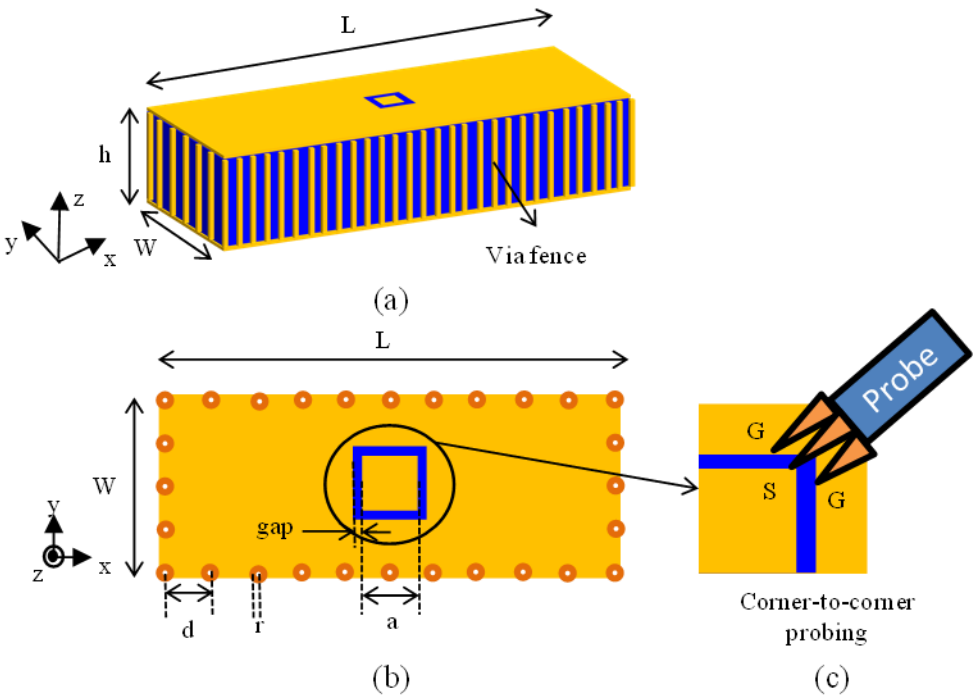

Figure 3.2. Details of SIW cavity resonator (a) perspective view, (b) top view and (c) corner-to-corner probing.

The resonant frequency of the TE_{m0k} mode in a SIW cavity is given by [29]

$$f_r = \frac{c}{2\sqrt{\varepsilon_r'\mu_r'}}\sqrt{\left(\frac{m}{W_{eff}}\right)^2 + \left(\frac{k}{L_{eff}}\right)^2}, \tag{17}$$

where c is the speed of light in free space, ε'_r and μ'_r are the relative permittivity and permeability of the SIW substrate medium respectively, and m, k are operation mode numbers. W_{eff} and L_{eff} represent the effective width and the effective length of the cavity respectively. Vias, with radius r, are used as the via fence with a spacing, d. The effective width and length W_{eff} and L_{eff} are given by [29]:

$$W_{eff} = W - \frac{4r^2}{0.95d}, \tag{18}$$

$$L_{eff} = L - \frac{4r^2}{0.95d}. \quad (19)$$

The resonators are excited at one of the maximum positions of the electric field in the cavity. A corner-to-corner probing method is applied for the excitation. As shown in Figure 3.2 (b) and (c), a square patch with length 'a' is patterned on the top plane with a gap and the signal tip of a Ground-signal-ground (GSG) probe is placed on the corner of the square patch with ground tips of the GSG probe on either side of the top plane. The corner-to-corner probing enables the excitation of the TE_{m0k} mode in the cavity. The size of the gap is determined by the pitch of the GSG probe and the length 'a' is optimized to maximize matching at resonance for the individual resonators. The SIW cavities can be designed with either the TE_{102} or TE_{103} resonant mode, where the TE_{102} mode can be used to measure material properties in the low frequency range since it can reduce the dimension of cavity resonator. Figure 3.3 and 3.4 show electric and magnetic field distributions of the SIW cavity at 1.5GHz with the TE_{102} resonant mode and at 2GHz with the TE_{103} resonant mode respectively. Light (red) and dark (blue) regions represent the highest and the lowest amplitude of field respectively. For a complex permittivity measurement, the sample is inserted at one of the maximum positions of the electric field, as shown in Figure 3.3 (a), 3.4 (a) ,while, for a complex permeability measurement, the sample is inserted at one of the maximum positions of the magnetic field, as shown in Figure 3.3 (b) and 3.4 (b).

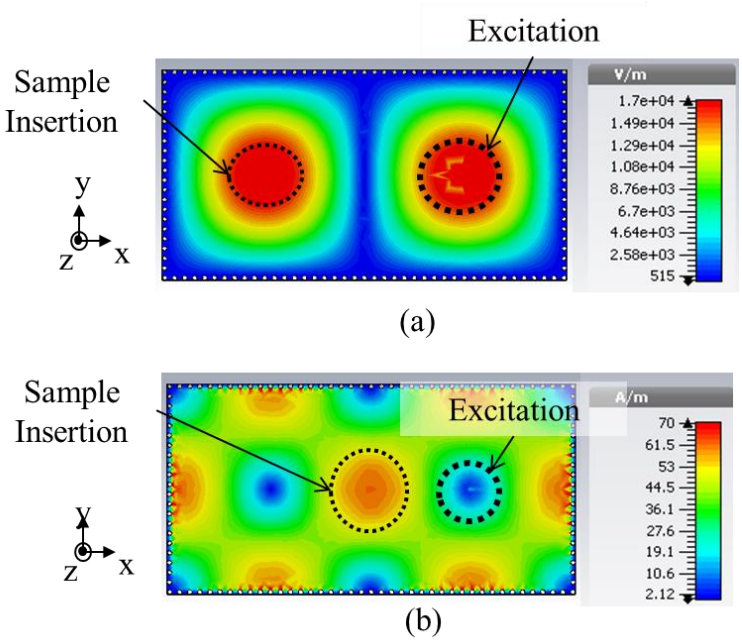

Figure 3.3. Field distribution of 1.5 GHz TE_{102} mode SIW cavity resonator and sample insertion location (a) E-field and (b) H-field.

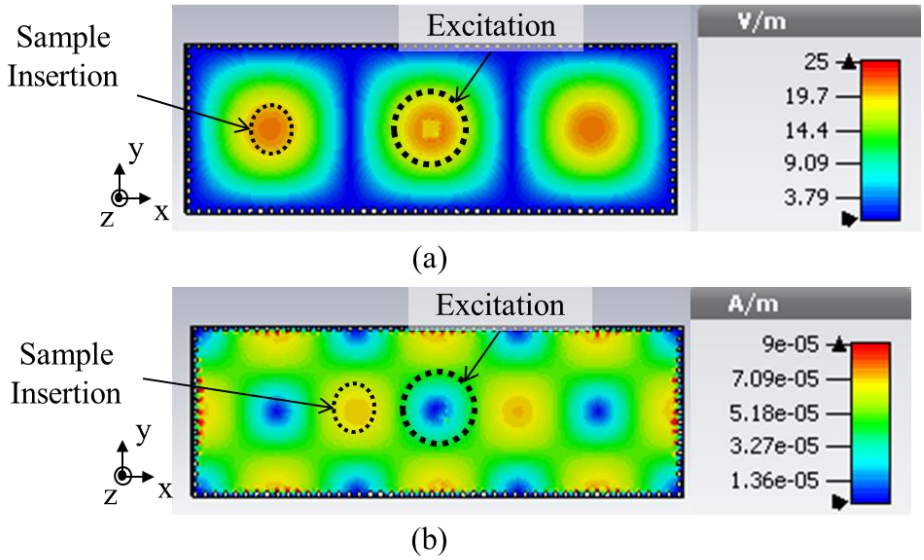

Figure 3.4. Field distribution of 2 GHz TE_{103} mode SIW cavity resonator and sample insertion location (a) E-field and (b) H field.

In the CPT, introducing the sample at either the E or H-field maximum position changes the resonant frequency and quality factor of the SIW cavity based on the sample's complex permittivity or permeability, respectively. During measurements, it is required that dielectric properties of the sample do not affect the complex permeability measurement while magnetic properties of the sample do not affect the complex permittivity measurement. To see the effect of dielectric and magnetic properties on the complex permittivity and/or permeability measurement, 3D EM simulation with CST microwave studio [31] has been used. A SIW cavity resonator using Rogers 3003 material [32] with ε'_r=3 and tanδ=0.0013 is modeled at 2 GHz with the TE_{103} resonant mode to analyze the CPT using SIW. Thickness of the substrate is 1.52mm. A cuboid sample with dimension of 6mm x 6mm x 1.52mm is inserted with material properties ε_r'=7, μ_r'=2 and electric loss tangent ($\tan\delta_e = \varepsilon_r''/\varepsilon_r'$) and magnetic loss tangent ($\tan\delta_m = \mu_r''/\mu_r'$) of 0.01 and 0.01, respectively. The ε'_r and μ'_r of the sample is varied between 6-8 and 1-3 respectively to see their effect on resonance. Similarly, $\tan\delta_e$ and $\tan\delta_m$ have also been varied between 0.01 – 0.03 and 0.05 – 0.3 to see their effect on Q factor. Q factor is determined by 3dB bandwidth of return loss, which can be expressed as:

$$Q = \frac{f_r}{f_{upper,3dB} - f_{lower,3dB}}, \tag{20}$$

where f_r is the resonant frequency and $f_{upper,3dB}$ and $f_{lower,3dB}$ represent the upper and lower limit of 3dB bandwidth, respectively.

Changes in resonance and Q factor based on the variations are listed in Table 3.

Table 3. SIW cavity response as varying permittivity/permeability with different sample location.

Sample Location	Permittivity				Permeability			
	ε_r	f_r (GHz)	Tanδ_e	Q	μ_r	f_r (GHz)	Tanδ_m	Q
E-field Maximum	6	1.949	0.01	174.73	1	1.945	0.05	184.16
	7	1.944	0.02	164.75	2	1.945	0.1	182.03
	8	1.94	0.03	156.47	3	1.944	0.3	180.08
H-field Maximum	6	1.957	0.01	183.58	1	1.961	0.05	172.23
	7	1.957	0.02	183.58	2	1.957	0.1	162.2
	8	1.957	0.03	183.58	3	1.953	0.3	138.08

When the sample is inserted at the electric field maximum position, variations of magnetic properties do not affect the resonance and Q factor of the cavity. Similarly, when the sample is located at the magnetic field maximum position, dielectric properties of the sample are not sensitive in changing the resonance and Q factor of the cavity, as shown in

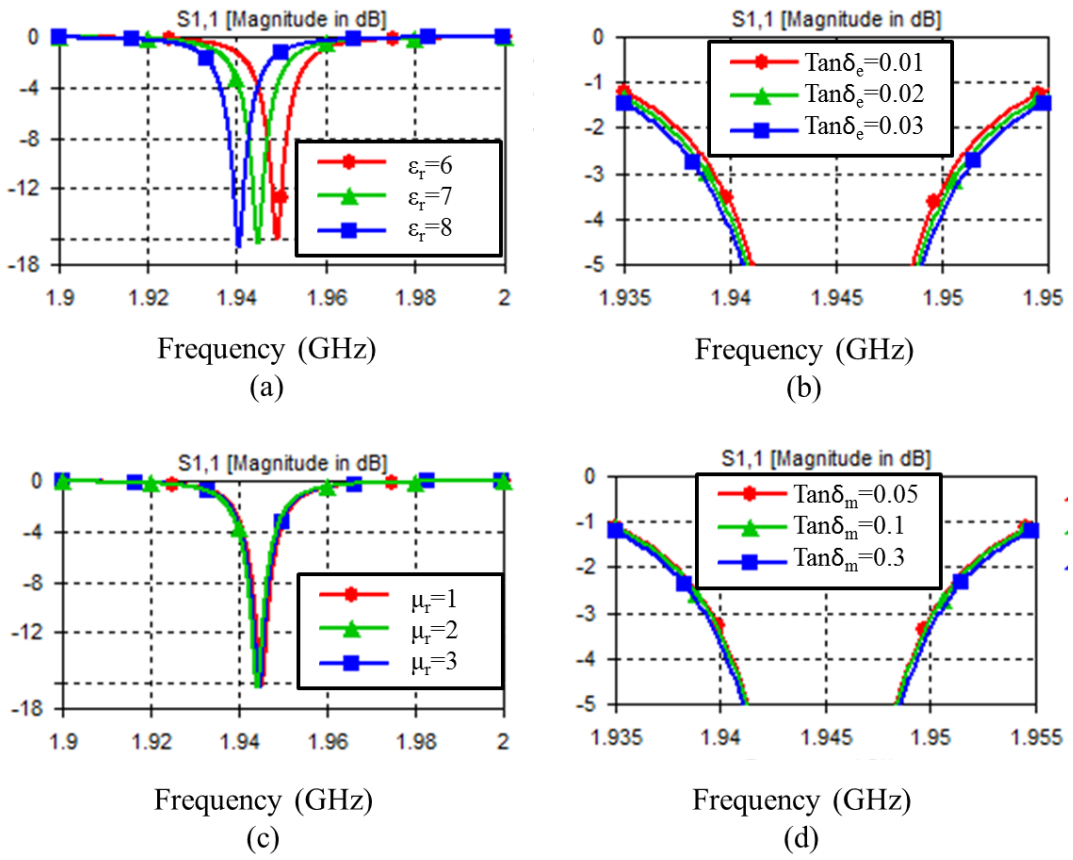

Figure 3.5. Return loss simulation with parameter sweep when the sample is at the E-field maximum position (a) ε'r, (b) μ'r, (c) electric loss tangent, and (d) magnetic loss tangent.

Table 3. Therefore, it can be concluded that CPT using SIW cavities can be used to characterize not only dielectric materials, but also MD materials with a single structure by using different sample locations. Figure 3.5 and 3.6 show return loss simulation results, (S11) by varying complex permittivity and complex permeability parameters of the inserted sample to demonstrate that these parameters are indeed isolated from each other.

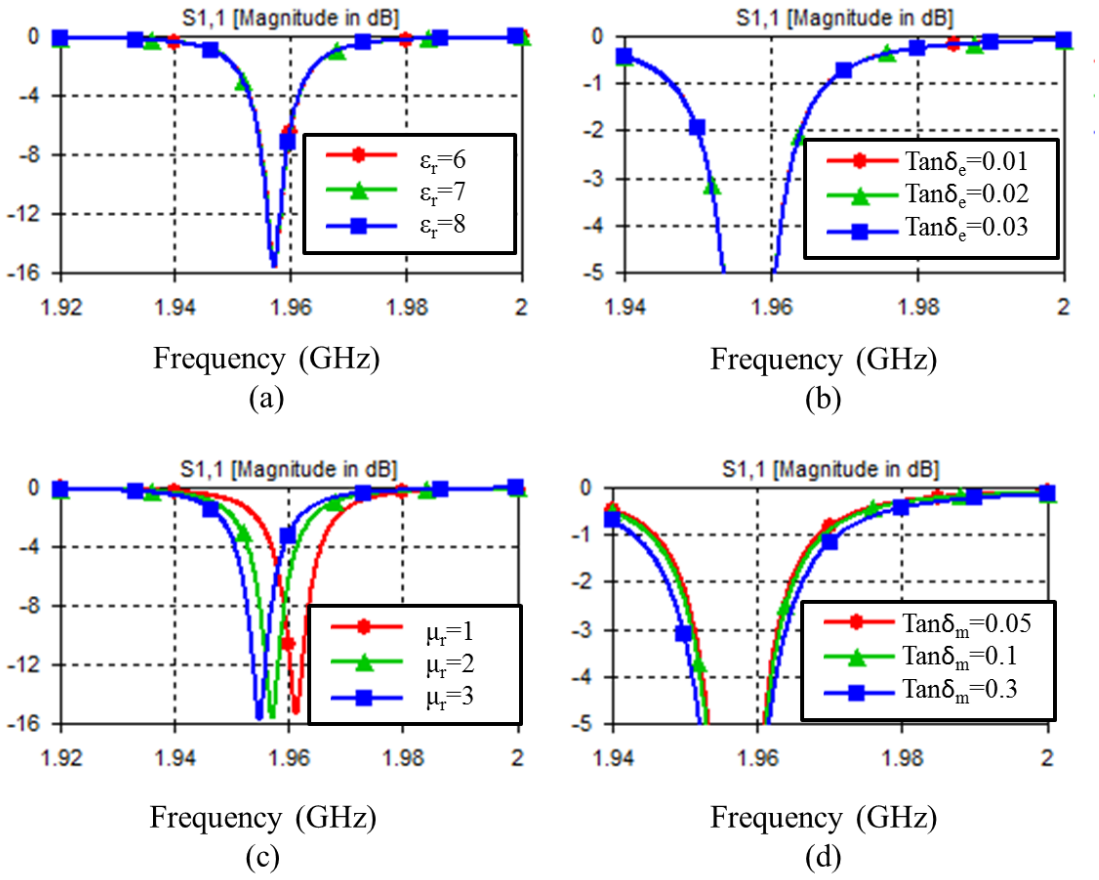

Figure 3.6. Return loss simulation with parameter sweep when the sample is at the H-field maximum position (a) ε'r, (b) μ'r, (c) electric loss tangent, and (d) magnetic loss tangent.

3.4 SIW Cavity Resonator Fabrication and Measurements

In order to measure the frequency dependent complex permittivity and permeability of the MD material, seven SIW cavity resonators were designed and fabricated with Rogers 3003 material, which was used for simulation in the previous section, to characterize the sample

in the frequency range 1-4 GHz. Figure 3.7 shows the fabricated SIW cavity resonators, and Table 4 shows their operating mode, resonant frequency and dimension.

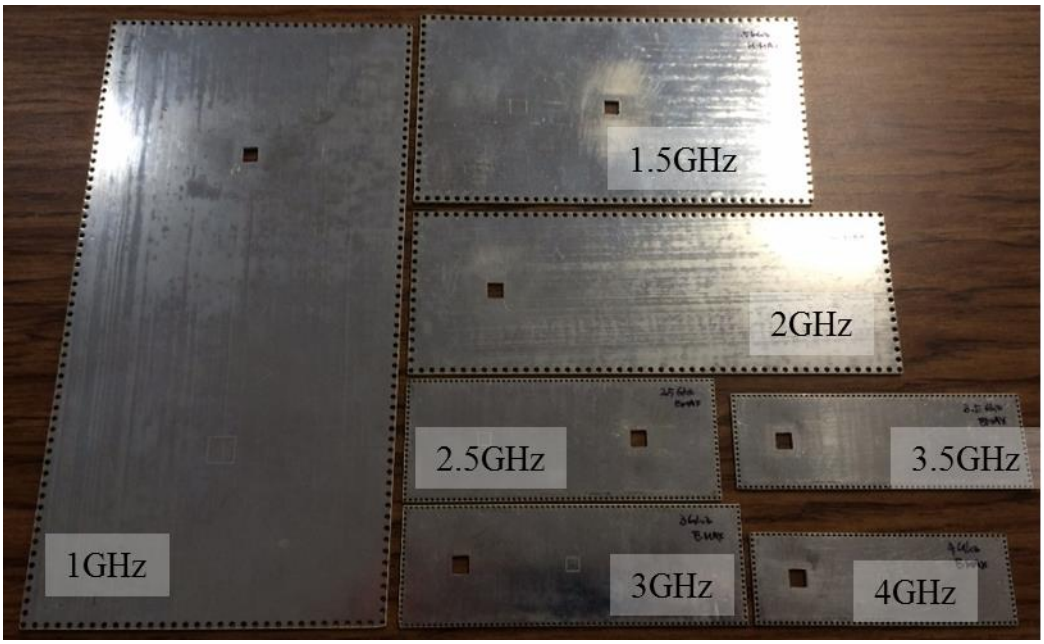

Figure 3.7. SIW cavity resonators.

Table 4. SIW Cavity Resonator Specification for Figure 3.2. (Units: mm)

f_r (GHz)	Mode	W	L	r	d	a
1	TE_{102}	242	126	1	4	9.5
1.5	TE_{102}	162	86	1	4	6.5
2	TE_{103}	190	66	1	4	6.6
2.5	TE_{102}	117	45	0.5	2	4.5
3	TE_{103}	123	41	0.5	2	4.5
3.5	TE_{103}	109	35	0.5	2	3.4
4	TE_{103}	93	31	0.5	2	3.2

A 6 mm x 6 mm square hole was drilled for sample insertion, as shown in Figure 3.8. The SIW cavity resonator in Figure 3.8 (a) has a hole at the E-field maximum position

for measuring complex permittivity only and another resonator in Figure 3.8 (b) has a hole at the H-field maximum position for measuring only the complex permeability. The location of both E and H-field maximum position is determined from a simulation of the E and H field distribution inside the cavities.

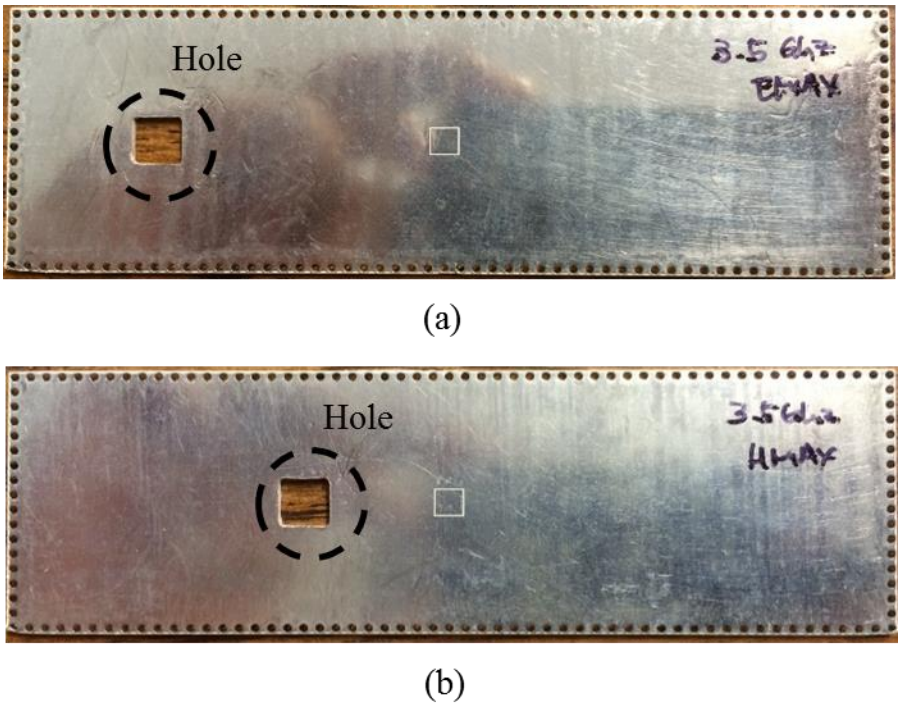

Figure 3.8. 3.5 GHz SIW cavity resonators with different hole locations for (a) permittivity and (b) permeability measurements.

Rogers dielectric material RO4360G2 [33] was chosen as the standard sample to obtain the constants A and B in (13) and (14) for each frequency while Cuming Microwave FLX-16 [34] magnetic absorber material was used to obtain the constants C and D in (15) and (16). All samples were prepared in a cuboid form with dimension of 6 mm × 6mm × 1.52 mm which is the same dimension that was used in the EM simulation, as shown in Figure 3.9. The cavity resonators were tested with a Vector network analyzer (VNA), Agilent Technologies E8363B, using Short, open, load and thru (SOLT) calibration. Figure

3.10 shows the corner-to-corner probing method for excitation and measurement. Samples were inserted in the hole and copper tape was used to cover the top and bottom of the sample. A GSG 500 probe from Cascade Microtech was used for the measurement.

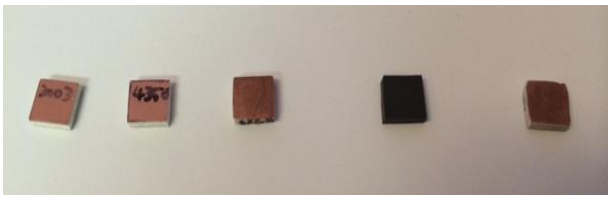

Figure 3.9. Picture of sample preparation.

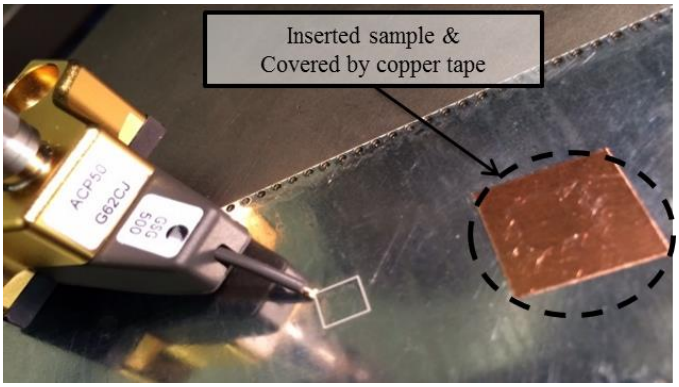

Figure 3.10. Corner-to-corner probe excitation.

The steps for the material property extraction process can be summarized as follows:

1. For permittivity measurement, insert a RO3003 sample (the same material as the SIW substrate) into SIW which has a hole at the E-field maximum and cover it with a copper tape.

2. Measure the return loss (S11) of the perturbed SIW cavity to obtain f_0 and Q_0 in equations (13) and (14).

3. Replace the RO3003 sample with a standard dielectric sample (RO4360G2 for this experiment) and measure the return loss to obtain f_s and Q_s in (13) and (14).

4. Substitute measured f_0, f_s, Q_0 and Q_s into the CPT equations, and find the A and B constants in (13) and (14) by matching calculated ε'_r and $\tan\delta_e$ with the properties of the standard sample.

5. Repeat the return loss measurements for other samples whose properties are well-known for validation.

6. Use the measured data to calculate the material properties and obtain a percentage error of the measurement by comparing the result with theoretical values provided by material suppliers.

7. Repeat steps 1 thru 6 with the SIW cavity which has the hole at the H-field maximum for permeability measurement. Find the C and D constants in equations (15) and (16) with a standard MD sample (FLX-16 for this experiment).

Figure 3.11 shows a return loss measurement of a SIW cavity (unloaded resonance at 2.5GHz), with various samples of different permittivity and permeability properties inserted in the hole. As shown in Figure 3.11 (a), the sample with higher permittivity shows a lower resonant frequency. It also can be observed that the sample with higher loss shows a wider 3dB bandwidth which corresponds to a lower Q factor. The resonant frequency and Q factor of the SIW cavity were changed negligibly when dielectric material samples were inserted at the H-field maximum position, as shown in Figure 3.11 (b). Magnetic absorber material, FLX-16, which has a permeability greater than 1 produces significant changes in the resonant frequency as well as the Q factor of the SIW cavity.

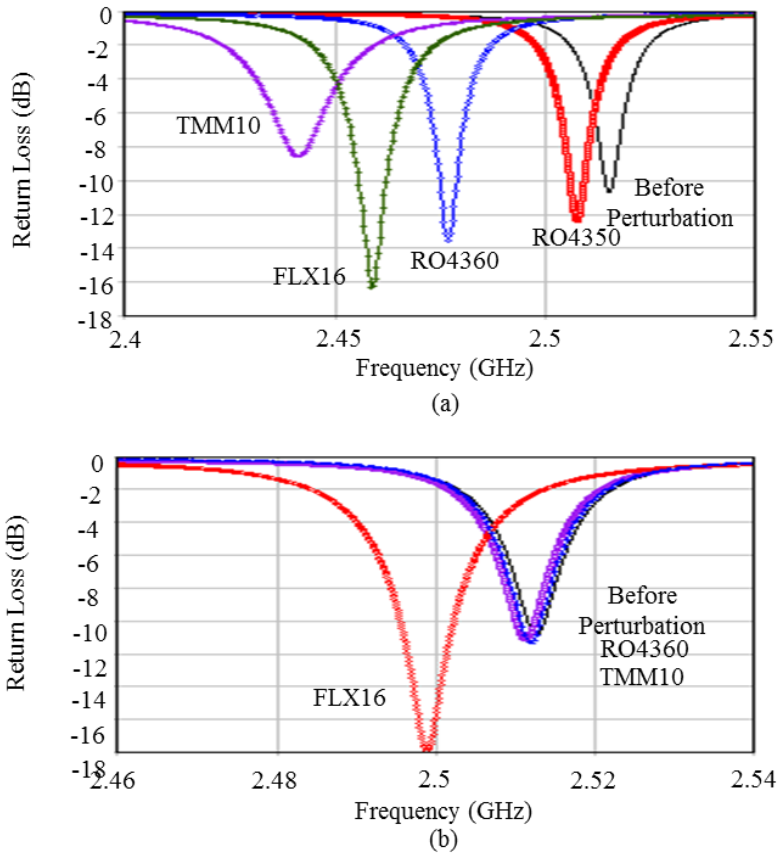

Figure 3.11. SIW cavity resonator measurements with various samples (a) E-field maximum position and (b) H-field maximum position.

Table 5 shows the measured material properties using the proposed CPT using SIW cavity (unloaded resonance at 2GHz). Both permittivity and permeability have been extracted and the results show that the measurements are very close to the theoretical values provided by material suppliers. The permittivity values of standard samples from material providers are very limited. Therefore, it is assumed that the permittivity of the standard sample is constant as provided by the supplier over the frequency range up to 4GHz for this paper. The error percentage of this method is obtained from these measurements by comparing the results with the values provided by the supplier for each frequency.

Table 5. Extracted permittivity and permeability of sample materials using measurements of 2GHz cavity.

Sample	ε_r		$\text{Tan}\delta_e$	
	Theoretical	Measured	Theoretical	Measured
RO4350 [35]	3.53	3.63	0.004	0.003
RO4360 [33]	6.4	6.39	0.0038	0.0038
TMM 6 [36]	6.3	6.33	0.0023	0.0029
TMM 10i [36]	9.9	10.3	0.002	0.0019
FLX-16 [34]	8	8.4	0.005	0.0057

Sample	μ_r		$\text{Tan}\delta_m$	
	Theoretical	Measured	Theoretical	Measured
RO4350 [35]	1	1.06	0.00	2e-4
RO4360 [33]	1	1	0.00	4.9e-9
TMM 6 [36]	1	1.01	0.00	2.24e-4
TMM 10i [36]	1	1.012	0.00	1.2e-4
FLX-16 [34]	2.5	2.49	0.2265	0.2285

3.5 Magneto-Dielectric Composite Synthesis and Properties Extraction

Metal-polymer (Cobalt-Fluoropolymer) nano-composite materials were synthesized to realize the MD material as shown in Figure 3.12 (a). Synthesizing an MD material having high permeability and low loss at high frequency is challenging and it can be achieved by reducing the particle size and separation between adjacent metal particles down to the nano-scale [27]. The material synthesis process that is introduced in Chapter 2 was performed to synthesize the MD material sample. The metal particles were milled with a dispersant in propylene glycol methyl ether acetate as the solvent medium and it was followed by another milling process with the polymer solution. After this milling process, the metal particle size was reduced to 20 – 30 nm and a metal-monomer slurry was produced. A TEM image of cobalt nanoparticles in the final nanocomposite is shown in Fig. 3.12 (b) [27]. The metal-monomer slurry was dried in a nitrogen oven to make a powder and excess solvent was evaporated. Dried powder was inserted in a die with size 6

mm x 6 mm and pressed with a uniaxial pressure to make the cuboid sample. The height of the magneto-dielectric sample was also controlled to have a height of 1.52mm.

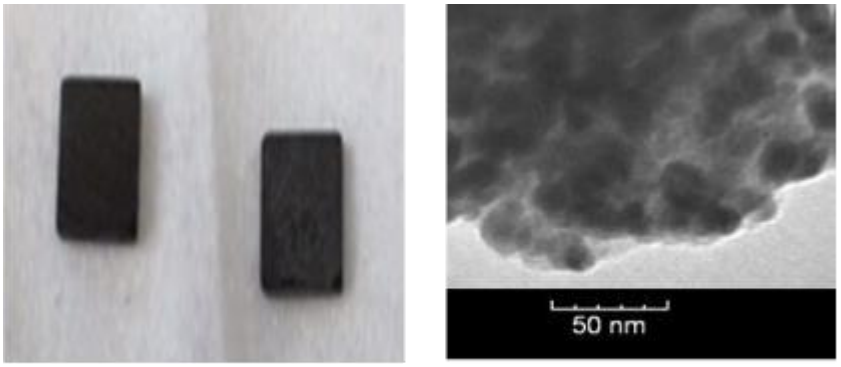

(a) (b)

Figure 3.12. (a) Picture of synthesized MD composite samples and (b) TEM image of cobalt in fluoropolymer matrix [27].

In this chapter, three MD material samples with different metal loading percentages 30%, 50% and 70% were synthesized in order to study the relationship between metal loading percentage in the composite material and the resulting material properties. Samples A, B and C represent 30%, 50% and 70% metal loading, respectively. Figures 3.13, 3.14, 3.15 and 3.16 show the extracted material properties of three MD composites using the seven SIW cavity resonators. Extracted values for seven frequencies are included in the plots as single data marks along with the curves corresponding to the 2nd order polynomial models fitted using these extracted data points. Figure 3.13 shows the results obtained for relative permittivity. All three samples show fairly constant ε'_r in the frequency range of 1-4 GHz but μ'_r decreases as the frequency increases, as shown in Figure 3.14. Sample C shows the highest ε'_r and μ'_r among the three samples. Sample A shows the lowest ε'_r and μ'_r among the three samples. Sample A showed $\varepsilon'_r = 9.5 \pm 0.5$ and μ'_r decreased from 2.18 to 1.7 in the frequency range 1-4 GHz. Sample B has ε'_r of 11.8 ± 0.6 and μ'_r of 2.18 @

1GHz and 1.8 @ 4GHz. Sample C showed ε'_r of 13.2±1 and μ'_r of 2.7 @ 1GHz and 2.1 @ 4GHz. Figures 3.15 and 3.16 show the results obtained for electric and magnetic loss tangent, respectively. As shown in these figures, a higher metal loading composite material shows higher loss for both $\tan\delta_e$ and $\tan\delta_m$ than a lower metal loading composite material. Changes in $\tan\delta_e$ were small but $\tan\delta_m$ increased significantly as the frequency increased. For $\tan\delta_e$, samples A, B and C have values of 0.004±0.0005, 0.004±0.001 and 0.005±0.0005 respectively. For $\tan\delta_m$, samples A, B and C have 0.018, 0.061 and 0.084 at 1GHz respectively. According to Snoek's law [37], higher initial permeability lowers ferromagnetic resonance (FMR), which is related to higher magnetic loss. This explains why the higher μ'_r sample shows higher $\tan\delta_m$.

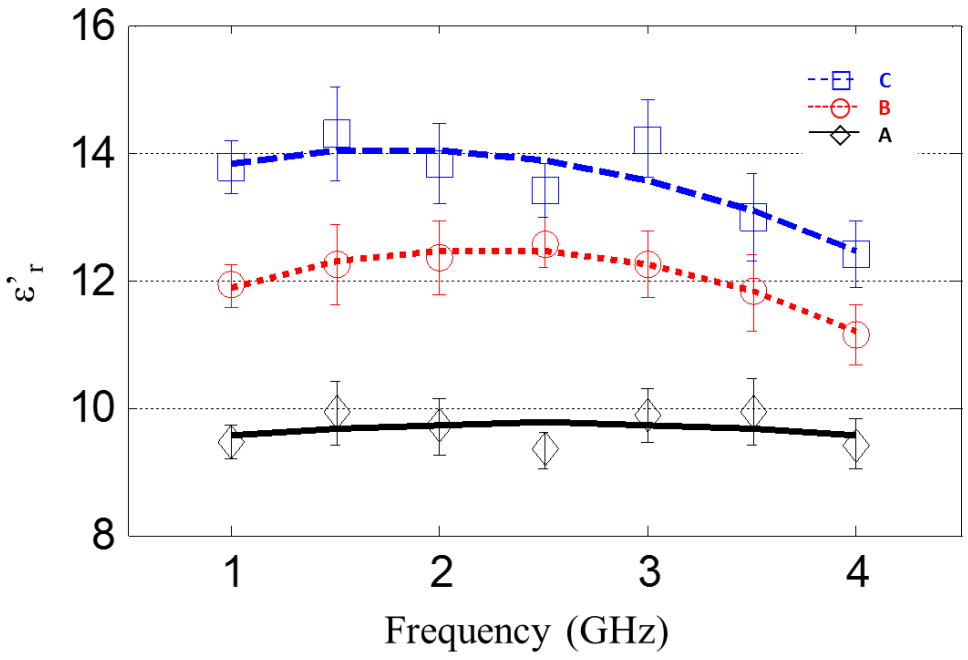

Figure 3.13. Extracted ε_r' using the CPT with SIW cavity resonators.

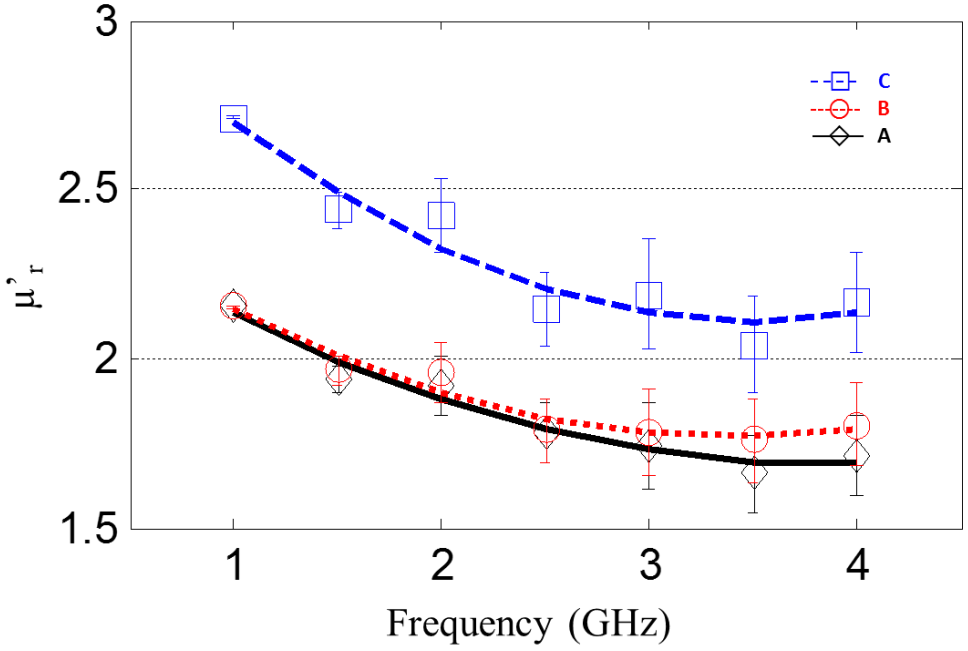

Figure 3.14. Extracted μ_r' using the CPT with SIW cavity resonators.

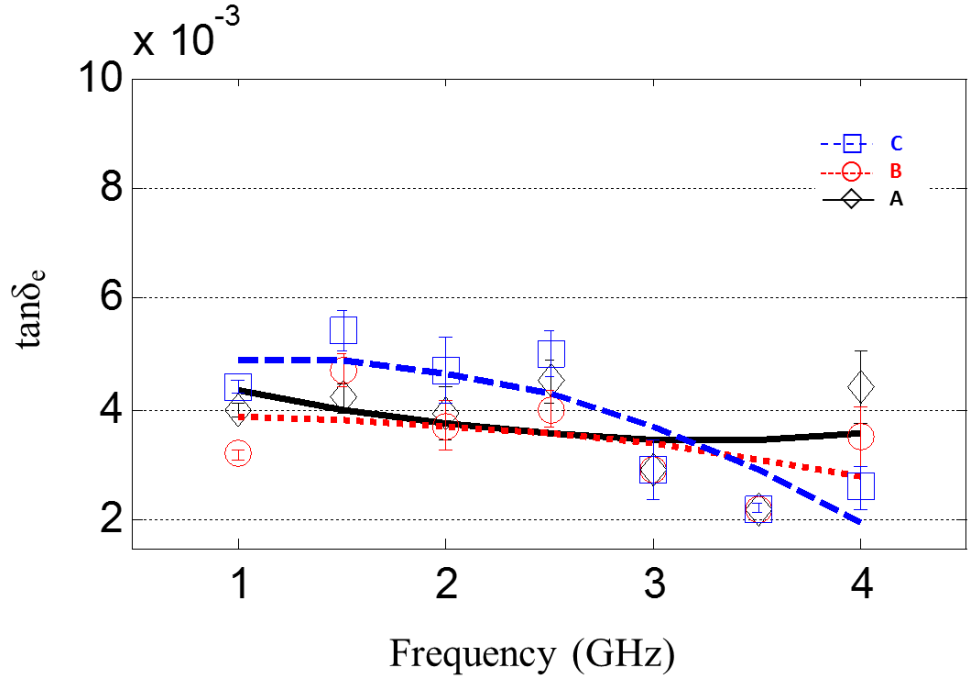

Figure 3.15. Extracted $\tan\delta_e$ the CPT with SIW cavity resonators.

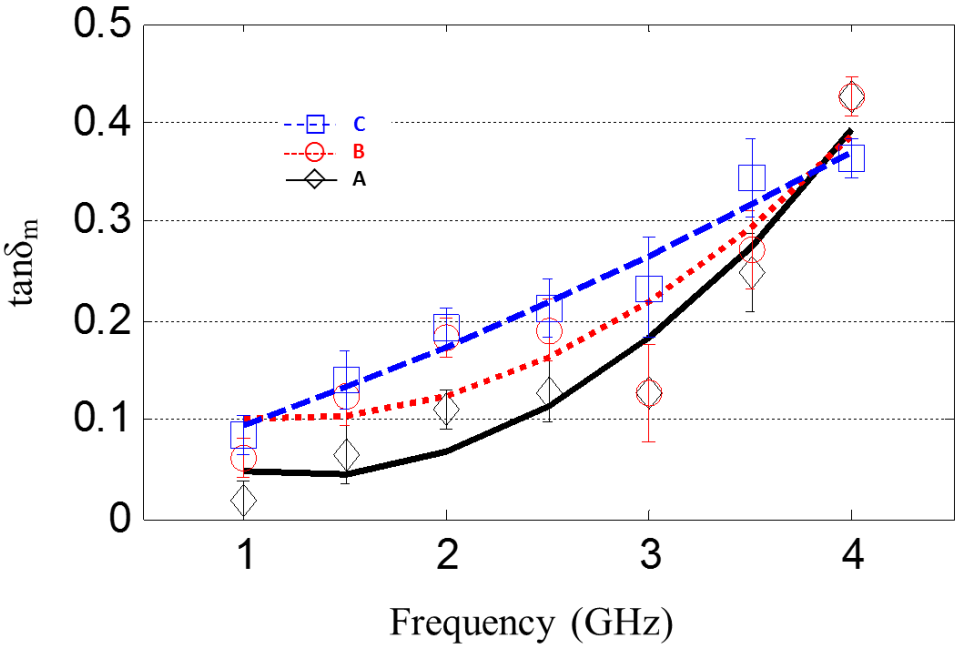

Figure 3.16. Extracted $\tan\delta_m$ the CPT with SIW cavity resonators.

Another sample, B', which has 50% metal loading, but a lower density than sample B, was also synthesized to study the relationship between the density of composite material and the resulting material properties. The density of samples B and B' were 3.65g/cm^3 and 2.75g/cm^3, respectively. Figures 3.17, 3.18, 3.19 and 3.20 show the comparison between the extracted material properties of samples B and B'. Sample B' showed $\varepsilon'_r = 6.5 \pm 0.2$ and μ'_r decreased from 1.8 to 1.4 in the frequency range 1-4 GHz. Comparing sample B and B', the lower density sample B' has a lower ε'_r and μ'_r than sample B. Lower density nano-composite can have higher porosity in the composite than higher density composite and this can cause increased distance between metal particles thereby decreasing both permittivity and permeability. From this, it can be concluded that MD, using metal-polymer system with desired permittivity and permeability values can be synthesized by optimizing metal loading percentage and density of nano composite material.

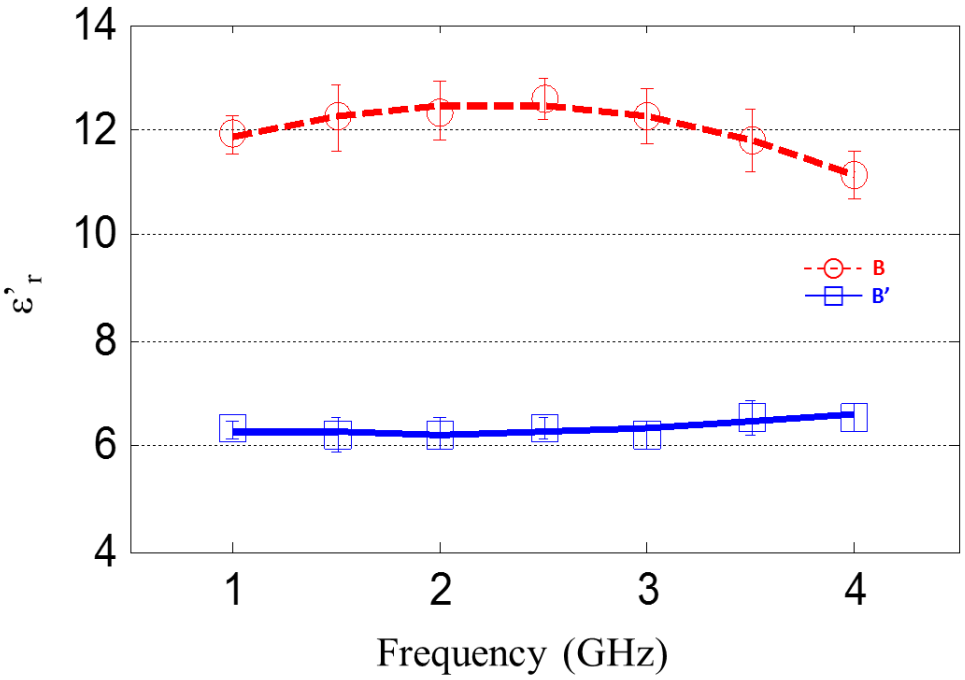

Figure 3.17. Extracted ε_r' for different density samples B and B'.

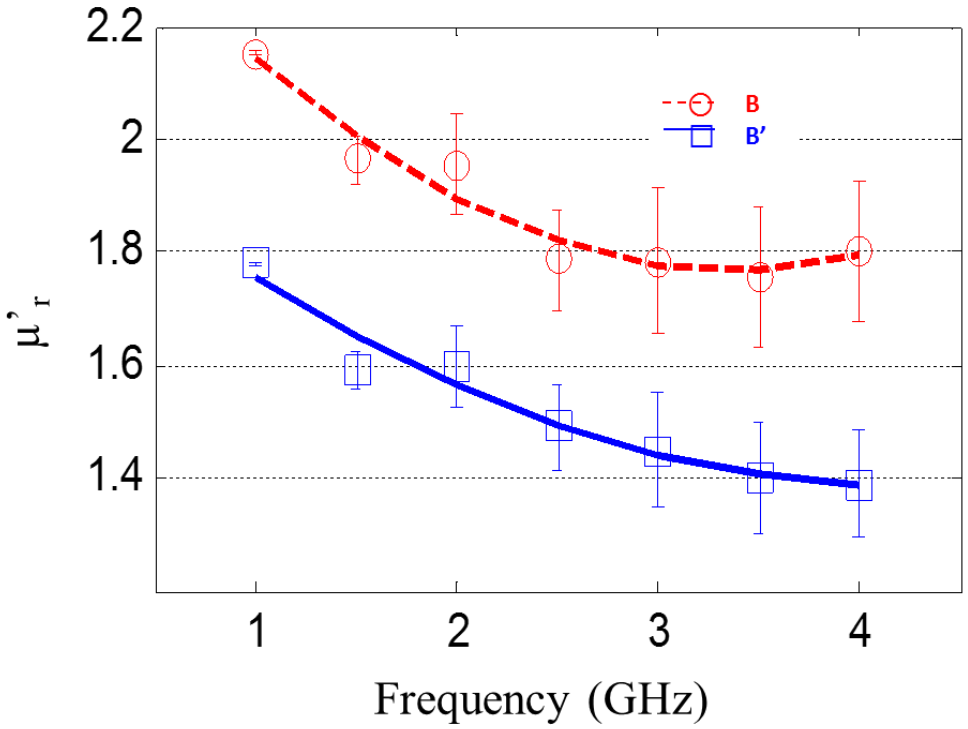

Figure 3.18. Extracted μ_r' for different density samples B and B'.

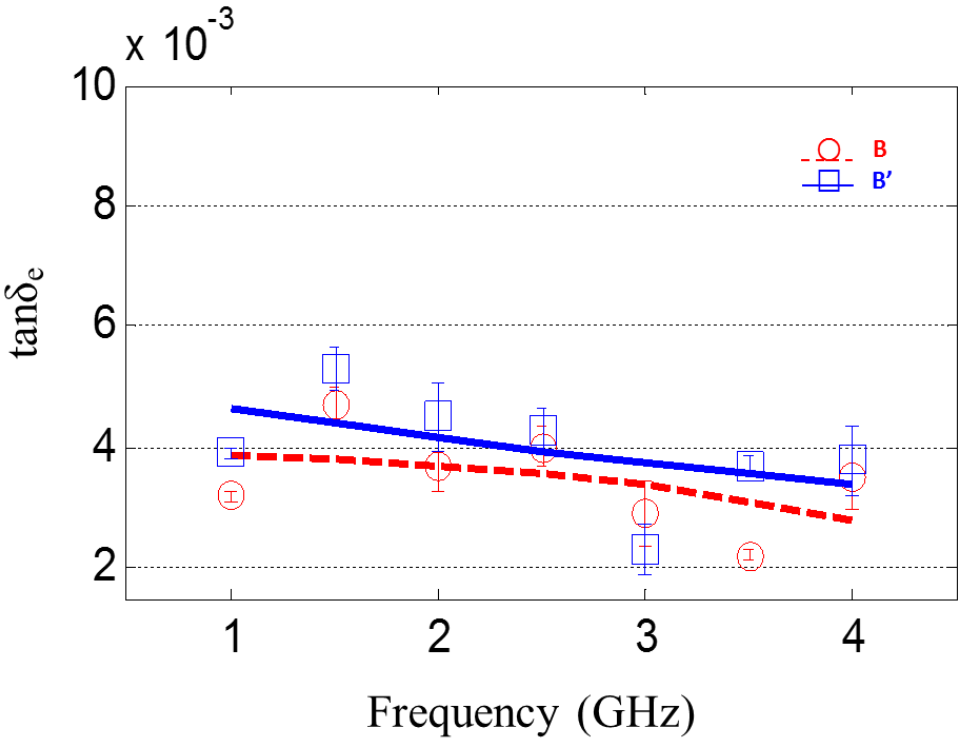

Figure 3.19. Extracted $\tan\delta_e$ for different density samples B and B'.

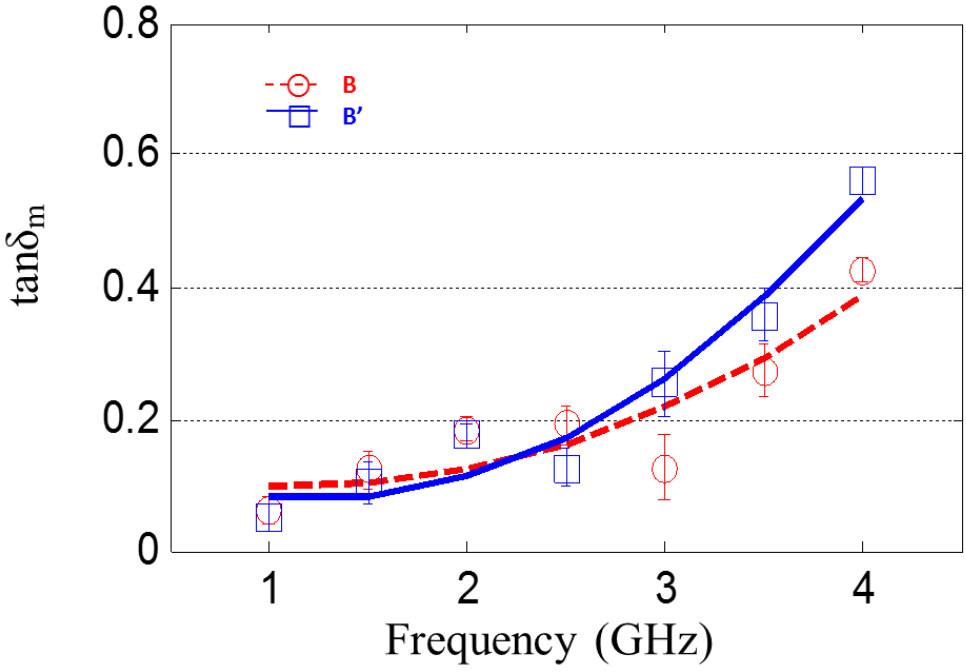

Figure 3.20. Extracted $\tan\delta_m$ for different density samples B and B'.

To validate these extracted properties, SIW cavity measurements were compared to CST simulations. Extracted properties of complex permittivity and permeability were used in CST for simulating the return loss of the SIW cavity. These simulations were compared to measurements as shown in Figures 3.21 and 3.22 for the seven cavities. The results indicate a high level of accuracy in the extracted properties of the sample.

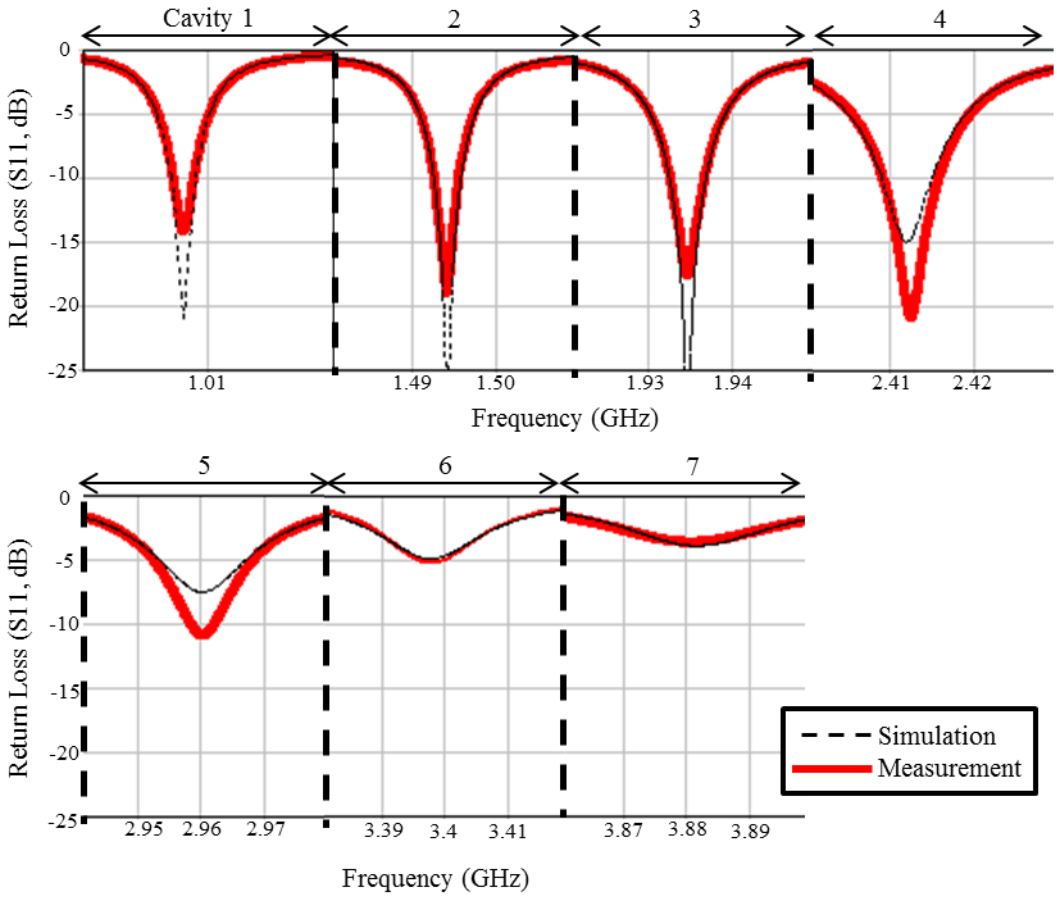

Figure 3.21. Correlation of return loss simulation and measurements of Sample B from permittivity measurements.

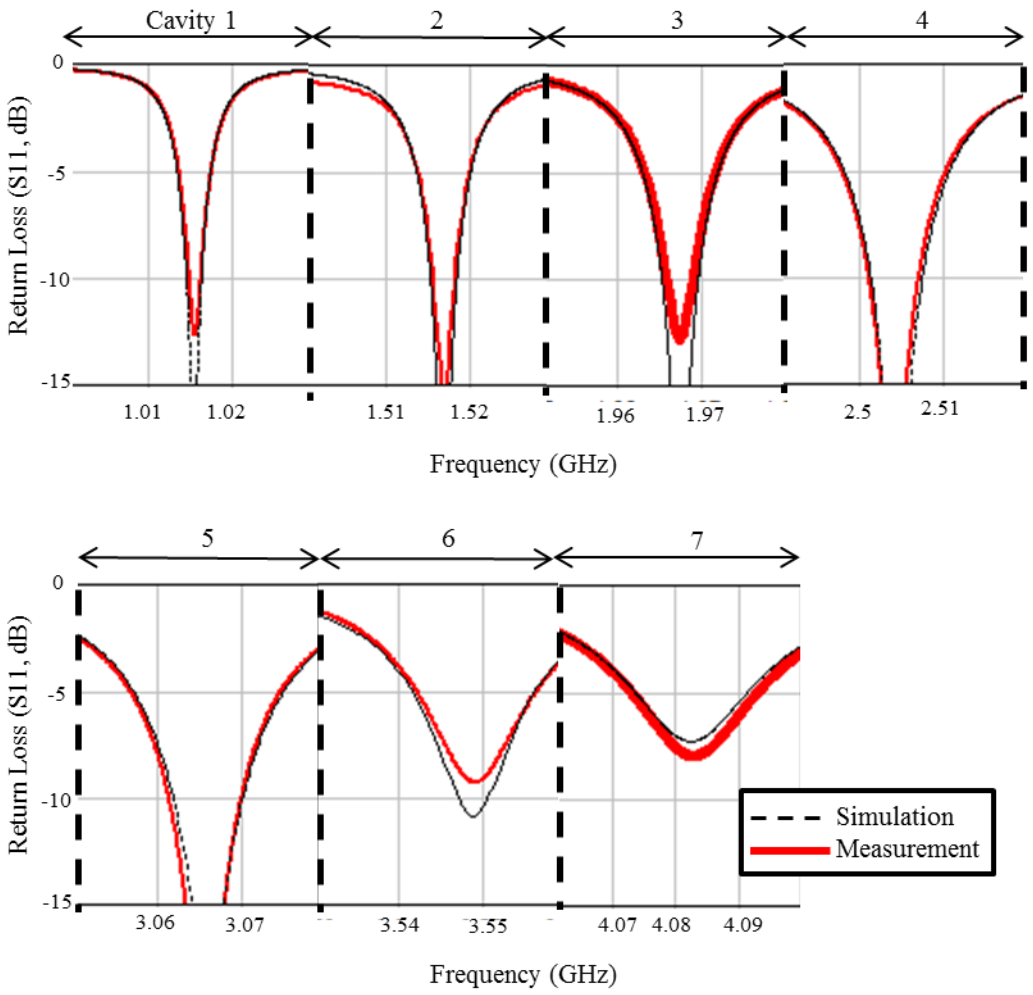

Figure 3.22. Correlation of return loss simulation and measurements of Sample B from permeability measurements.

3.6 Analysis of Anisotropic Property

The magnetic and dielectric properties of the MD material may exhibit anisotropy since the ferromagnetic material can have magnetocrystalline anisotropy (takes more energy to magnetize in certain directions than in others [38]). Therefore, the fields in the SIW cavity resonator are analyzed to illustrate the components of the dielectric and magnetic properties which have been measured. Electric and magnetic field distribution inside of the cavity resonator in vector form is shown in Figure 3.23. As shown in Figure 3.23 (a), only the E-

field along the z-direction is present where the electric field is maximum inside the cavity. Likewise, only the H-field along the y-direction is present where the magnetic field is maximum inside the cavity, as shown in Figure 3.23 (b).

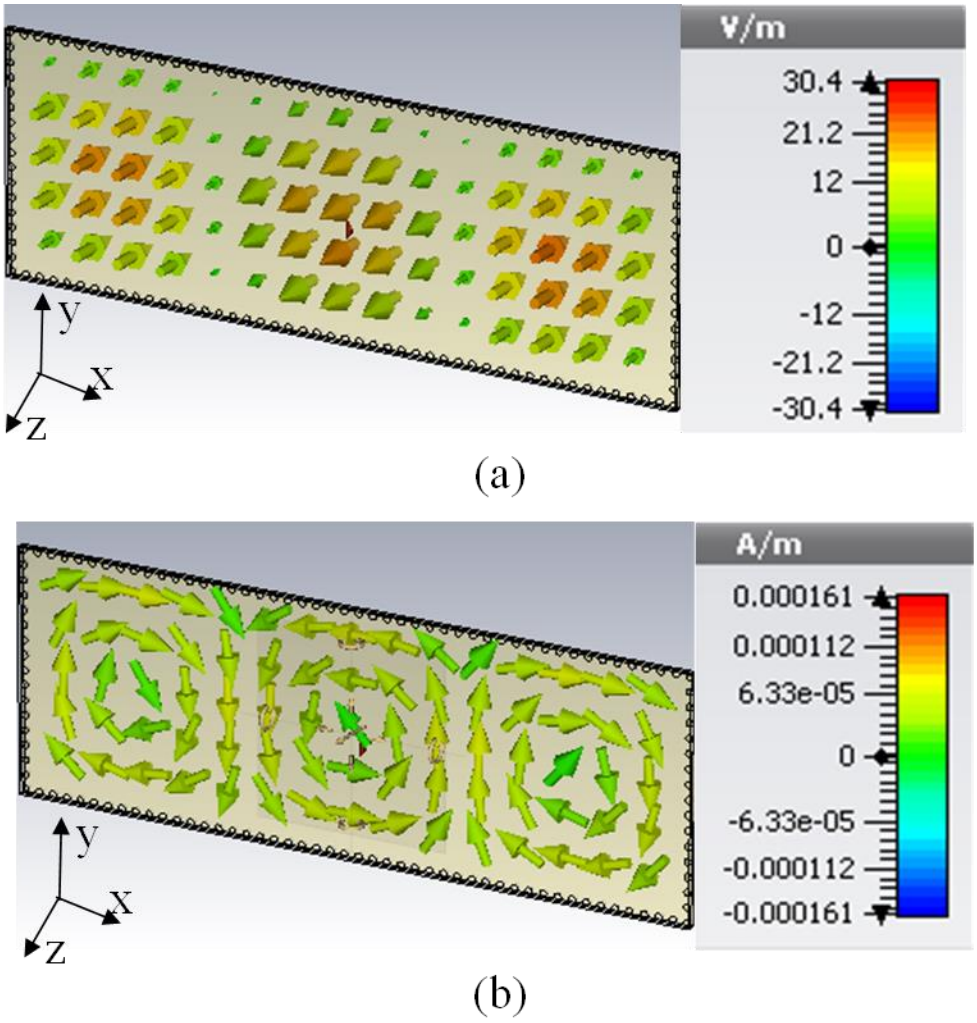

Figure 3.23. Field vector distribution in SIW cavity (a) E-field and (b) H-field.

To understand the effect of material properties on field distribution, the $\varepsilon_{x,y,z}$ of the sample is varied from 6 to 8 and the $\mu_{x,y,z}$ of the sample is varied from 1 to 3 to see their effect on the response of the cavity. Figure 3.24 shows that only ε_z and μ_y of the sample material changes the resonance, but the rest of the parameters have no effect. Since the

sample has an equal size along x and y direction, μ_x can also be measured by rotating the sample 90 degrees around the z-axis. Therefore, the CPT with SIW using the present setup can measure the ε_z and $\mu_{x,y}$ of the material as well.

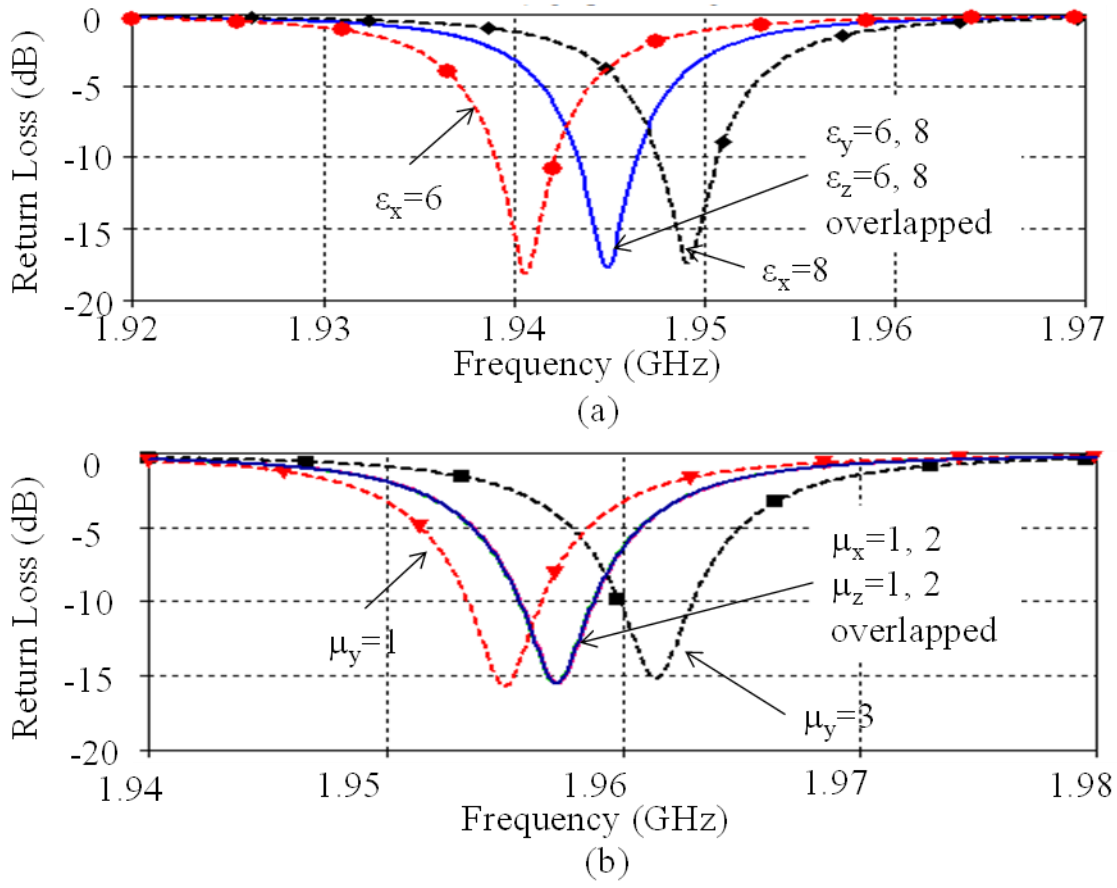

Figure 3.24. Return loss simulation with parameter sweep (a) $\varepsilon_{x,y,z}$ sweep when the sample is at E-field maximum, (b) $\mu_{x,y,z}$ sweep when the sample is at H-field maximum.

Sample C from the previous section was tested to measure μ_x and μ_y. The response of the SIW cavity was measured with the sample in one direction first and re-measured after rotating the sample 90 degrees along the z-axis. A 2 and 2.5 GHz SIW cavity resonator was used to measure μ_x and μ_y of sample C, as shown in Figure 3.25. In both cases, there

was no significant change in resonance and therefore, μ_x and μ_y are the same. It is therefore our conclusion that the material properties of the metal-polymer composite reported in this chapter pertain to ε_z and μ_x, μ_y. However, it is important to also note that all three components of the complex permeability and permittivity can be extracted using the SIW cavity designed in this chapter by fabricating the sample as a cube and rotating the sample.

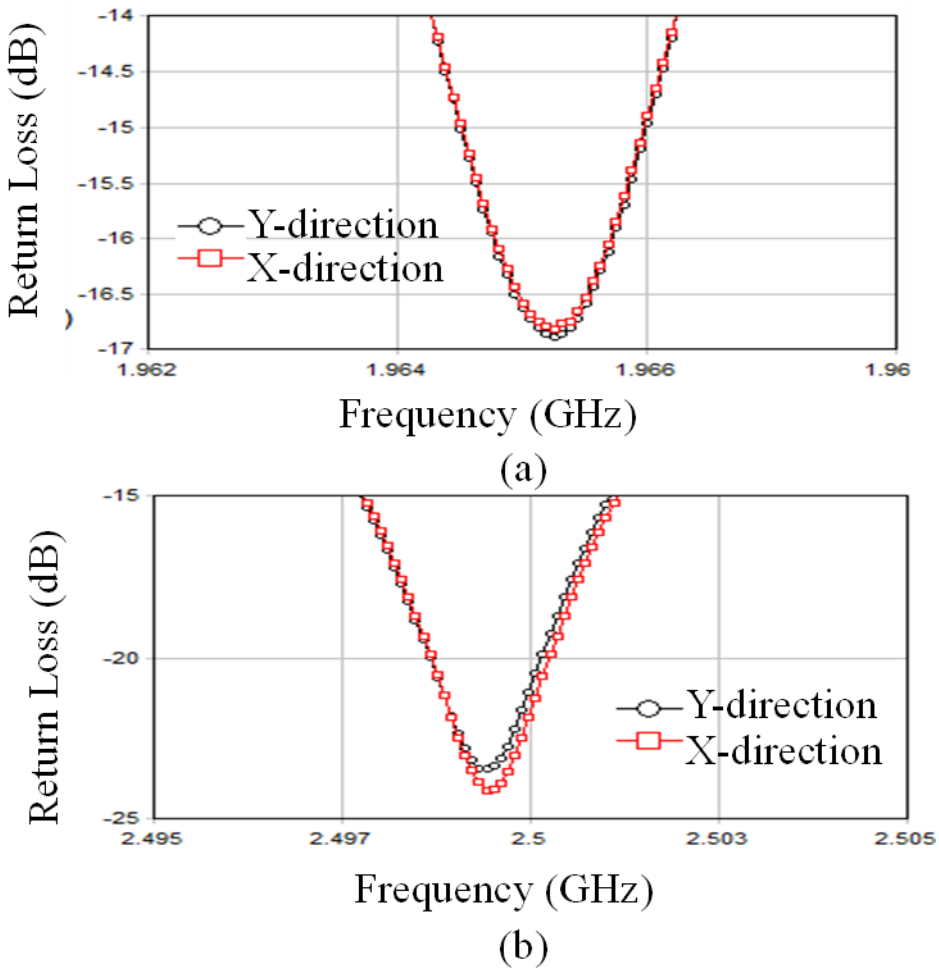

Figure 3.25. Return loss measurements of sample C in two directions with (a) 2GHz SIW cavity and (b) 2.5GHz SIW cavity.

3.7 Air Gap Analysis

The measurement result of CPT shown in sections 3.4 and 3.5 assumed that there were no air gaps around the inserted sample. When the sample is inserted into the hole in the SIW cavity, any air gap around the sample can alter its extracted properties. Hence special care was taken to ensure that the sample was suitably sized to fit exactly into the cavity. In this section we analyzed the error introduced due to the presence of any air gap, using simulation with CST. A Sample with ε_r=7, μ_r=2, tanδ_e=0.001 and tanδ_m=0.001 was used for analysis at 2GHz. The return loss of the SIW cavity with the inserted sample was simulated as the volume of the sample was decreased. From Figure 3.26, it can be seen that a reduction in sample volume of 5% resulted in a 4.2% error in the extracted relative permittivity. However, a similar reduction in volume resulted in only a 2.5% error for the extracted relative permeability.

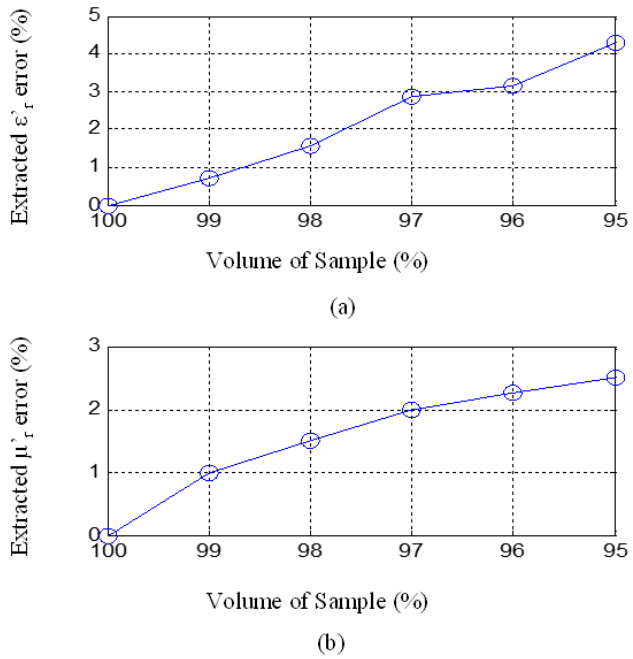

Figure 3.26. Effect of air gap (a) permittivity measurement and (b) permeability measurement.

3.8 Summary

This chapter presented a Cavity Perturbation Technique using SIW cavity resonators that can extract material properties of MD materials. The frequency dependent complex permittivity and permeability of MD materials were measured. A single SIW cavity resonator can be used to extract both properties by changing sample insertion location inside of the cavity. For a complex permittivity measurement, the sample was inserted at the E-field maximum and for a complex permeability measurement, the sample was inserted at the H-field maximum. The isolation between electric and magnetic measurement was shown through simulation and experiments. Cobalt-Fluoropolymer was used to synthesize magneto-dielectric materials and was measured in the frequency range 1-4GHz in this study. Three different metal loading composites were measured in order to analyze their effects on material properties. As the metal loading in the composite material increased, both real permittivity and permeability values increased as well along with the loss. For instance, the extracted permittivity and permeability of a 30% metal loading MD sample are 9.5-j0.038 and 2.18-j0.039 at 1GHz, respectively. A Magnetic loss tangent of 0.018 at 1Ghz is the best property reported in this frequency for metal nano-composite material.

Another magneto-dielectric sample with different density was also synthesized and characterized. By reducing the density of the sample, the permittivity and permeability decreased even though the sample had the same metal loading percentage. An anisotropic material measurement has also been considered and the CPT with SIW cavity resonator characterization method described in this chapter was able to measure ε_z and $\mu_{x,y}$ of magneto-dielectric samples. The synthesized MD composite materials are, however,

expected to be isotropic since the shape anisotropy is non-existent and effect of crystal anisotropy is small due to randomness. Effect of air gap around inserted sample is also analyzed using an EM solver and it was observed that controlling the sample dimension as close to the dimension of hole in the SIW cavity is very important. Based on simulations, less than 5% error in the estimation of material properties occurs with a 5% air gap (based on volume).

CHAPTER 4

CAUSAL MODEL DEVELOPMENT FOR EXTRACTED MD MATERIAL PROPERTIES

4.1 Introduction

This chapter introduces a fitting model for extracted magneto-dielectric material properties using the method introduced in Chapter 3. In general, a material cannot polarize instantaneously in response to an applied field and this fact leads to frequency dependence of the permittivity and permeability. The response, which should be causal, must always arise after the applied field and it can be validated using Kramers-Kronig relations. According to their relations, the real part of electric/magnetic susceptibility, which is a measure of how easily material polarizes in response to an applied field, can be calculated from the imaginary part of the electric/magnetic susceptibility and vice versa. The extracted complex permittivity and permeability have to satisfy the Kramers-Kronig relations; otherwise, the extracted data would be non-causal and can provide inaccurate results when used in an antenna simulation [39].

The extracted material properties from resonators are obtained at discrete frequency points. Seven discrete frequency points were measured in the frequency range 1-4 GHz in this study. Extrapolation of the data is necessary to estimate the material properties outside the frequency range of the resonances of the cavities to analyze the performance of the antenna. In this chapter, a causal fitting model for extracted complex permittivity and permeability of MD composite materials is presented and the Kramers-Kronig relations are used to verify the causality.

4.2 Kramers-Kronig Relations

In electromagnetism, the electric susceptibility, X_e, indicates the degree of polarization of a dielectric material in response to an applied electric field and is given by [40]:

$$P = \varepsilon_0 X_e E\,, \tag{21}$$

where P is the polarization density, ε_0 is the electric permittivity of free space and E is the electric field. The electric susceptibility is also related to the polarizability of individual particles in the medium and it is related to its relative permittivity, ε_r by

$$X_e = \varepsilon_r - 1, \tag{22}$$

Similarly, the magnetic susceptibility, X_m is a proportionality that indicates the degree of magnetization of a material in response to an applied magnetic field and is given by the following relationship [41]:

$$M = \mu_0 X_m H\,, \tag{23}$$

where M is the magnetization of the material, μ_0 is the permeability of vacuum and H is the magnetic field. The magnetic susceptibility is related to its relative permeability, μ_r as

$$X_m = \mu_r - 1, \tag{24}$$

In general, a material cannot polarize and magnetize instantaneously in response to an applied electric and magnetic field. The polarization is a function of time:

$$P(t) = \varepsilon_0 \int_{-\infty}^{t} X_e(t-t')E(t')\,dt'\,. \tag{25}$$

The polarization is a convolution of the electric field at previous times with time-dependent susceptibility given by $X_e(\Delta t)$ and so it is more convenient to take the Fourier transform

and rewrite it as a function of frequency. The integral (25) becomes a simple product as follows:

$$P(\omega) = \varepsilon_0 X_e(\omega) E(\omega). \tag{26}$$

This frequency dependent electric susceptibility leads to a frequency dependent permittivity and the shape of this susceptibility determines the dispersion properties of the material. The fact that the polarization can only depend on the applied electric field at previous times is a consequence of causality, which imposes Kramers-Kronig constraints on the real and imaginary parts of the susceptibility. Since the magnetization correlates to polarization, magnetic susceptibility is also dependent on frequency and should satisfy the causality condition.

The Kramers-Kronig relations describe how the real part of the susceptibility is related to the imaginary part of susceptibility and vice versa. The susceptibility can be expressed in complex form as [42]:

$$X(\omega) = X'(\omega) - jX''(\omega), \tag{27}$$

and since the polarization and magnetization is a measurable quantity, we have:

$$X(\omega) = X^*(-\omega). \tag{28}$$

Substituting equation (28) into Equation (27) gives two subsequent relations:

$$X'(\omega) - jX''(\omega) = X'(-\omega) + X''(-\omega), \tag{29}$$

and these relations result in:

$$\begin{aligned} X'(\omega) &= X'(-\omega), \\ X''(\omega) &= -X''(-\omega), \end{aligned} \tag{30}$$

where, the real part of the susceptibility is an even function of ω and the imaginary part of the susceptibility is an odd function of ω.

The X’ (ω) can be derived from X” (ω) using the Kramers-Kronig relations by considering the integral:

$$I = \oint_C \frac{\omega X(\omega) d\omega}{\omega^2 - \omega_0^2}. \tag{31}$$

The contour of the integration is shown in Figure 4.1.

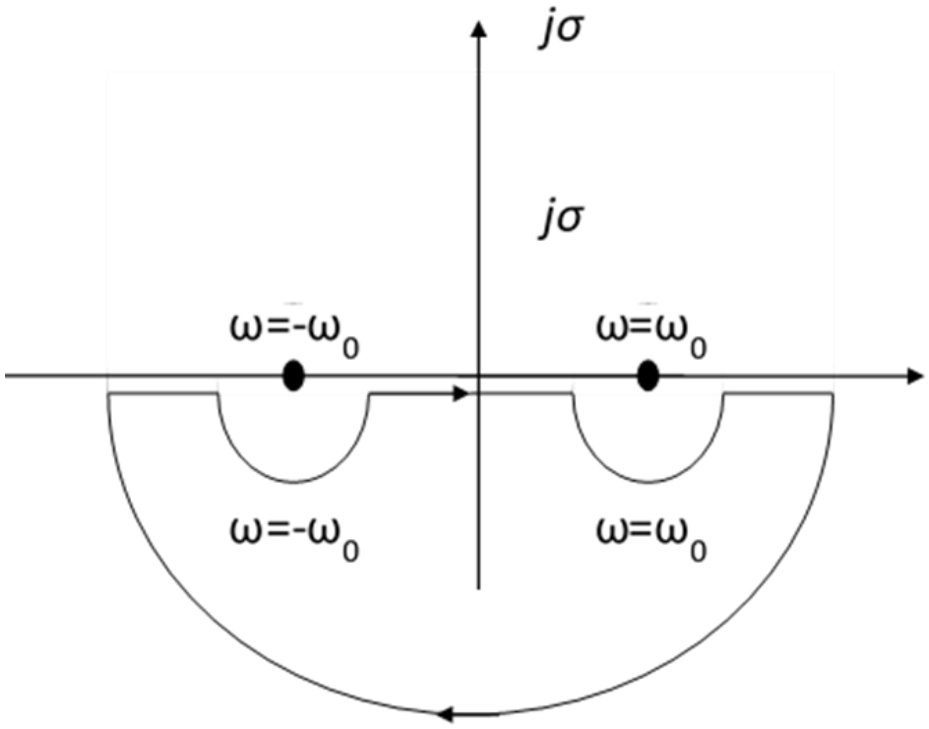

Figure 4.1. Contour of integration for Equation (31).

This integral simplifies to the following:

$$\begin{aligned} I &= P\int_{-\infty}^{\infty}\frac{\omega X(\omega)d\omega}{\omega^2-\omega_0^2}-\frac{\pi j}{2}\left[X(\omega_0)+X(-\omega_0)\right]=0, \\ &\Rightarrow P\int_{-\infty}^{\infty}\frac{\omega X(\omega)d\omega}{\omega^2-\omega_0^2}=\frac{\pi j}{2}\left[2X'(\omega_0)\right], \\ &\Rightarrow P\int_{-\infty}^{\infty}\frac{\omega\left(X'(\omega)-jX''(\omega)\right)d\omega}{\omega^2-\omega_0^2}=\pi jX'(\omega_0). \end{aligned} \tag{32}$$

where P is the Cauchy principle value. According to equation (30), ωX' (ω) is an odd function of ω because X' (ω) is an even function of ω, however, ωX" (ω) becomes an even function of ω since X" (ω) is an odd function of ω. Therefore the integral part in (32) can be separated into two parts and their relation can be described as:

$$\begin{aligned} \int_{-\infty}^{\infty}\frac{\omega X'(\omega)d\omega}{\omega^2-\omega_0^2}&=0, \\ \int_{-\infty}^{\infty}\frac{-j\omega X''(\omega)d\omega}{\omega^2-\omega_0^2}&=-2j\int_0^{\infty}\frac{\omega X''(\omega)d\omega}{\omega^2-\omega_0^2}. \end{aligned} \tag{33}$$

Combining above result with Equation (32), the real part of susceptibility can be expressed by a function of the imaginary part of susceptibility as follows:

$$X'(\omega_0)=-\frac{2}{\pi}P\int_0^{\infty}\frac{\omega X''(\omega)d\omega}{\omega^2-\omega_0^2}. \tag{34}$$

There is an inverse relation for X" (ω). This relation can be derived by considering the following integral:

$$I=\oint_C\frac{X(\omega)d\omega}{\omega^2-\omega_0^2}. \tag{35}$$

After applying the same integration contour in Figure 4.1, equation (35) can be simplified to the following:

$$I = P\int_{-\infty}^{\infty} \frac{X(\omega)d\omega}{\omega^2-\omega_0^2} - \frac{\pi j}{2}\left[\frac{X(\omega_0)}{\omega_0} - \frac{X(-\omega_0)}{\omega_0}\right] = 0,$$
$$\Rightarrow P\int_{-\infty}^{\infty} \frac{X(\omega)d\omega}{\omega^2-\omega_0^2} = \frac{\pi X''(\omega_0)}{\omega_0}. \quad (36)$$

Since X' (ω) is an even function of ω and X" (ω) is an odd function of ω, the integral in Equation (36) can be separated into two parts and their relations can be rewritten as:

$$\int_{-\infty}^{\infty} \frac{X'(\omega)d\omega}{\omega^2-\omega_0^2} = 2\int_{0}^{\infty} \frac{X'(\omega)d\omega}{\omega^2-\omega_0^2},$$
$$\int_{-\infty}^{\infty} \frac{X''(\omega)d\omega}{\omega^2-\omega_0^2} = 0. \quad (37)$$

Finally, X" (ω) can be described as a function of X' (ω) as:

$$X''(\omega_0) = \frac{2\omega_0}{\pi} P\int_{0}^{\infty} \frac{X'(\omega)d\omega}{\omega^2-\omega_0^2}. \quad (38)$$

Equation (34) and (38) are referred to as the Kramers-Kronig relations. Extracted material properties should satisfy these relations in order to be causal.

4.3 Modeling of Magneto-Dielectric Material Property

The Lorentzian dispersion law for permittivity modeling is a well-known method for a single-domain material which is given as [43]:

$$\varepsilon(f) = \varepsilon_\infty + \frac{\Delta\varepsilon}{1 + j\,f/f_{rel} - \left(f/f_0\right)^2} - \frac{j\sigma_e}{2\pi f \varepsilon_0}, \quad (39)$$

where ε_∞ is optic region permittivity; $\Delta\varepsilon=\varepsilon_s-\varepsilon_\infty$ and ε_s is static dielectric constant; f_0 and f_{rel} are resonance and relaxation frequency respectively; f_{rel} is also used as Debye resonance frequency. These parameters determines the loss peak and the shape of the dispersion curve. The third term in equation (39) is related to the conductivity loss, where σ_e is the

direct current electric conductivity of the material, and ε_0 is the permittivity of free space [43]. Usually, the third term is removed to simplify the equation, because it is only important at frequencies below ~100Hz. The dispersion law for permeability modeling is also similar to equation (39) with no conductivity term. An example in Figure 4.2 shows the permittivity dispersion curve obtained by equation (39) without the third term. The dispersion curve is calculated with f_0= 5 GHz and f_{rel} =2, 4, 6 and 8 to see the effect of the relaxation frequency on the shape of dispersion. ε_∞ is 1 and $\Delta\varepsilon$ is 1 for this example. As f_{rel} increases, the imaginary part of the permittivity shows a peak at the resonance frequency and the loss tangent also increases as shown in Figure 4.2. The distribution of loss is also getting sharper as the relaxation frequency is increased.

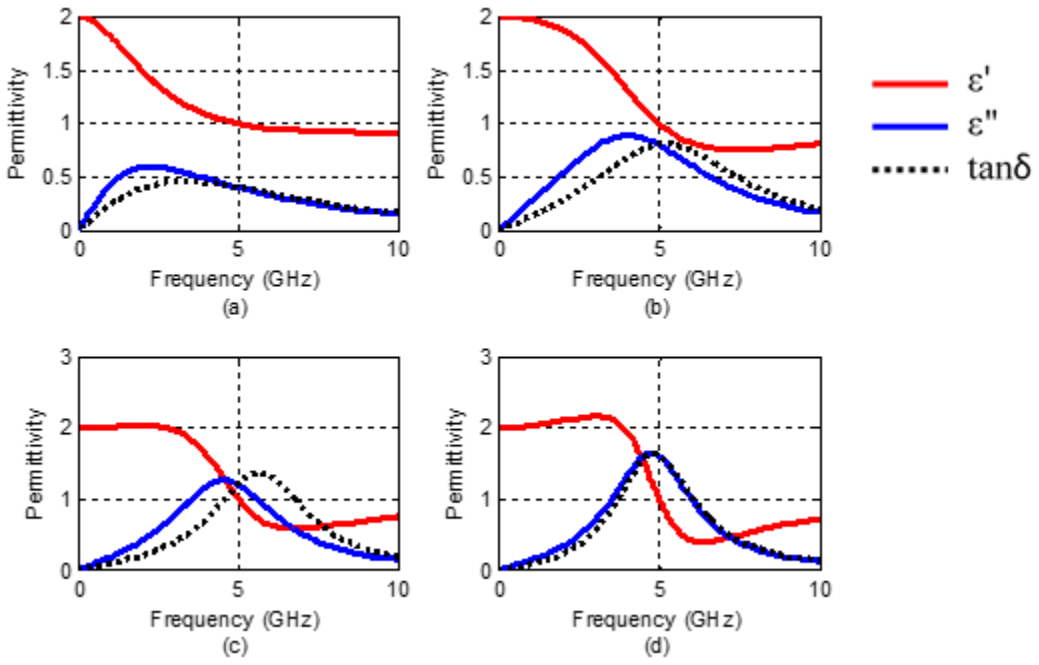

Figure 4.2. Frequency dependence of permittivity calculated with Lorentzian dispersion law with f_{rel} = (a) 2GHz, (b) 4GHz, (c) 6GHz and (d) 8GHz.

The Debye dispersion law is also a popular method for permittivity modeling and it is a particular case of the more general form of equation (39), when $f_0 \rightarrow \infty$. The Debye model describe the comparatively low-frequency behavior of a medium associated with dipolar polarization of molecules in dielectrics, or with domain wall movement in some magnetic materials [44]. The resonance frequency of composite material depends on the particle's shape and orientation and therefore a distribution of resonance frequencies is dependent on the composition and technology of the material. In most actual magnets, the resultant magnetic dispersion curve is still of the Lorentzian shape but the width of the spectrum increases greatly, being a function of inhomogeneity of the sample rather than being a function of the Gilbert damping parameter, which determines the relaxation frequency in equation (39) [44]. If the distribution of resonance frequencies is wide, then $f_{rel} < f_0$ and the dispersion law is close to the Debye dispersion law as shown Figure 4.3.

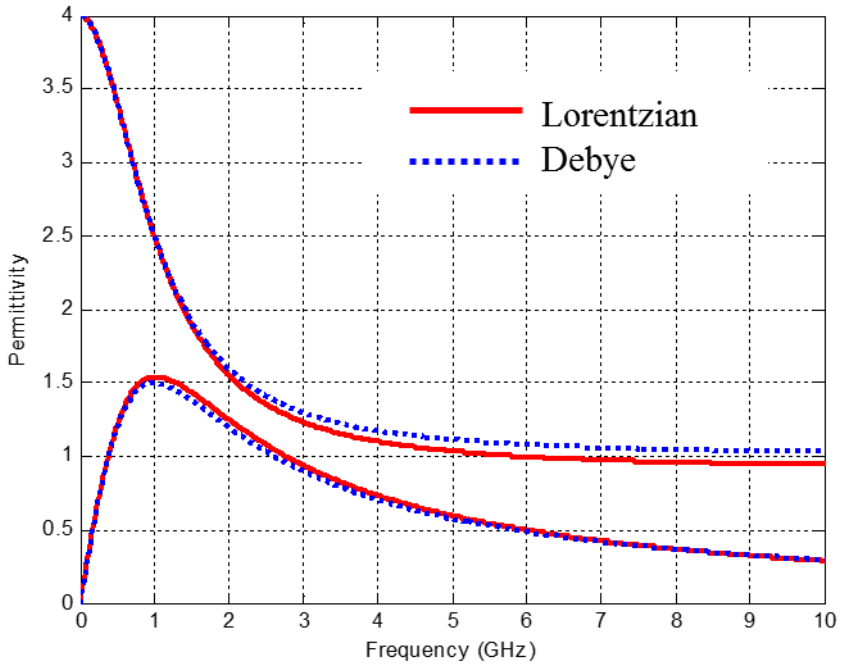

Figure 4.3. Comparison of Lorentzian and Debye dispersion law when $f_{rel} < f_0$.

Both the Lorentzian and Debye dispersion model describe well the dipolar relaxation behavior of individual molecules, however, most synthesized composite materials do not follow those models. The actual behavior of the synthesized composite materials may contains several loss peaks rather than a single peak due to inhomogeneity of particles inside of composition and several different physical mechanisms contributing to the dispersion in a magneto-dielectric material [44]. The dispersion relation for several resonances based on the Lorentzian dispersion model can be expressed as:

$$A = A'_{\infty} + \sum_{i=0}^{n} \frac{\Delta A'_i}{1 - \left(f / f_{1,i} \right)^2 + j\left(f / f_{2,i} \right)}. \tag{40}$$

where A represents either ε or μ; $\Delta A'_i$ represents amplitude change of the response at the *i*th peak; $f_{1,i}$ and $f_{2,i}$ are resonance and relaxation frequency at the *i*th peak, respectively. With a properly chosen sum of several resonances, any actual dispersion dependence can be fitted.

To fit the extracted material properties from Chapter 3, the three resonance model is chosen. The three pole Lorentzian dispersion model is given by:

$$A = A'_{\infty} + \frac{\Delta A'_1}{1 - \left(\frac{f}{f_1} \right)^2 + j\left(\frac{f}{f_2} \right)} + \frac{\Delta A'_2}{1 - \left(\frac{f}{f_3} \right)^2 + j\left(\frac{f}{f_4} \right)} + \frac{\Delta A'_3}{1 - \left(\frac{f}{f_5} \right)^2 + j\left(\frac{f}{f_6} \right)}. \tag{41}$$

Before finding the unknown variables in equation (41) that fits the extracted results in Figures 3.13 – 3.16, the three pole Lorentzian dispersion model needs to be checked to ensure causality using the Kramer-Kronig relations. To use the Kramers-Kronig relations in equation (34) and (38), equation (41) needs to be separated into real and imaginary parts. The real part of the three pole Lorentzian dispersion model can be expressed as:

$$\mathrm{Re}(A) = A'_{\infty} + \frac{\Delta A'_1\left(1-\left(\frac{f}{f_1}\right)^2\right)}{\left(1-\left(\frac{f}{f_1}\right)^2\right)^2+\left(\frac{f}{f_2}\right)^2} + \frac{\Delta A'_2\left(1-\left(\frac{f}{f_3}\right)^2\right)}{\left(1-\left(\frac{f}{f_3}\right)^2\right)^2+\left(\frac{f}{f_4}\right)^2} + \frac{\Delta A'_1\left(1-\left(\frac{f}{f_5}\right)^2\right)}{\left(1-\left(\frac{f}{f_5}\right)^2\right)^2+\left(\frac{f}{f_6}\right)^2}, \tag{42}$$

and the imaginary part as:

$$\mathrm{Im}(A) = -\frac{\Delta A'_1\left(1-\left(\frac{f}{f_2}\right)\right)}{\left(1-\left(\frac{f}{f_1}\right)^2\right)^2+\left(\frac{f}{f_2}\right)^2} - \frac{\Delta A'_2\left(1-\left(\frac{f}{f_4}\right)\right)}{\left(1-\left(\frac{f}{f_3}\right)^2\right)^2+\left(\frac{f}{f_4}\right)^2} - \frac{\Delta A'_1\left(1-\left(\frac{f}{f_6}\right)\right)}{\left(1-\left(\frac{f}{f_5}\right)^2\right)^2+\left(\frac{f}{f_6}\right)^2}. \tag{43}$$

The causality of this model can be verified by substituting equations (42) and (43) into the integral in equations (34) and (38) and comparing the result from the integration with analytic solution from equations (34) and (38). Figures 4.4 and 4.5 show the real and imaginary parts of A as calculated using equations (34) and (38). The results from the Kramers-Kronig relation and analytic solution show good correlation, and therefore, the three pole Lorentzian dispersion model is causal.

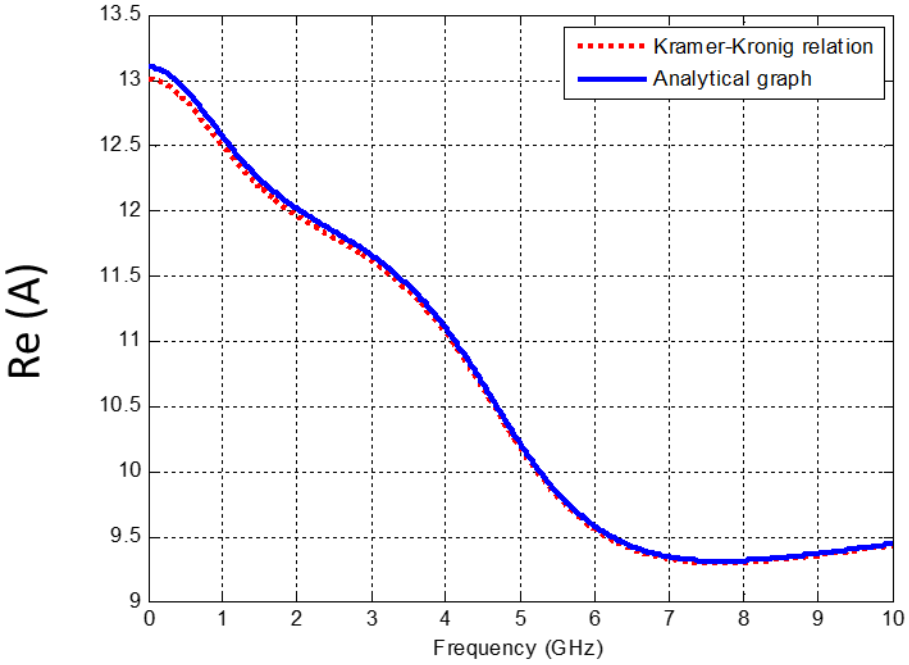

Figure 4.4. Real part of A as calculated using Equation (34).

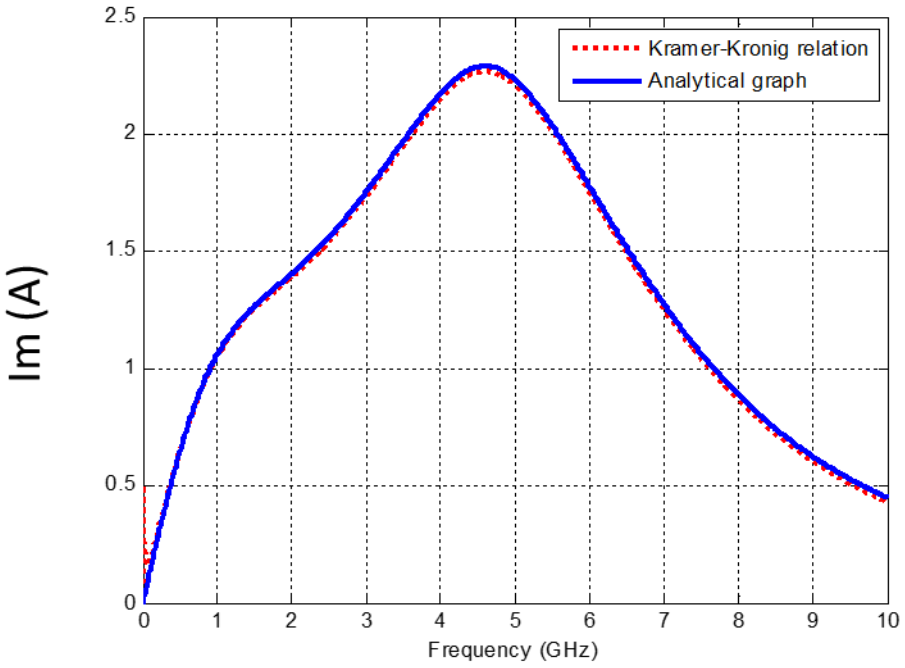

Figure 4.5. Imaginary part of A as calculated using Equation (38).

The extracted permittivity and permeability of MD materials from Chapter 3 are fitted using the three pole Lorentzian dispersion model. The unknown parameters in equation (41) are found empirically and they are summarized in Table 6 for permittivity and in Table 7 for permeability. As shown in Figures 4.6 thru 4.11, all extracted material properties for 30%, 50% and 70% metal loading samples show good correlation with the three pole Lorentzian dispersion model. The extracted material properties, therefore, from the CPT with SIW cavity resonators are causal.

Table 6. Parameters of Equation (41) for complex permittivity model.

Sample	A'_∞	ΔA_1	ΔA_2	ΔA_3	f_1	f_2	f_3	f_4	f_5	f_6
A	9.7	0.027	0.02	0.022	1.23	1.33	2.51	3.51	4.82	10
B	12	0.036	0.021	0.02	1.46	1.6	2.7	3.61	4.1	9.1
C	13.8	0.043	0.028	0.037	1.37	1.68	2.8	3.7	4.6	6.5

Table 7. Parameters of Equation (41) for complex permeability model.

Sample	A'_∞	ΔA_1	ΔA_2	ΔA_3	f_1	f_2	f_3	f_4	f_5	f_6
A	1.2	-4	0.01	0.58	0.23	0.3	2	2.6	5.3	7
B	1	-8	0.07	0.8	0.2	0.11	2	3.6	5.5	7.8
C	1.7	-3	0.22	0.4	0.4	1.5	2.2	3	4	7.5

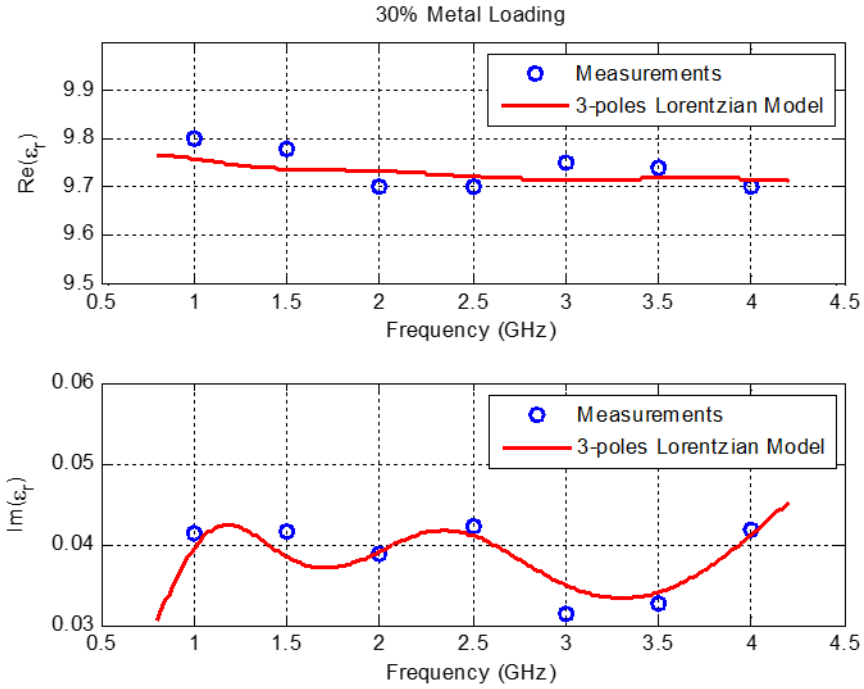

Figure 4.6. Complex permittivity modeling for 30% metal loading sample.

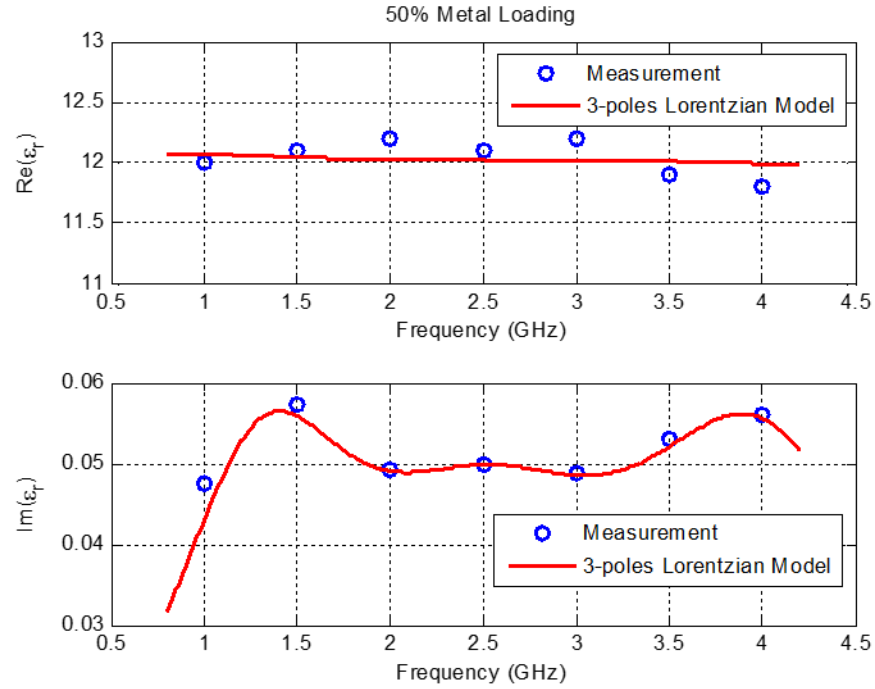

Figure 4.7. Complex permittivity modeling for 50% metal loading sample.

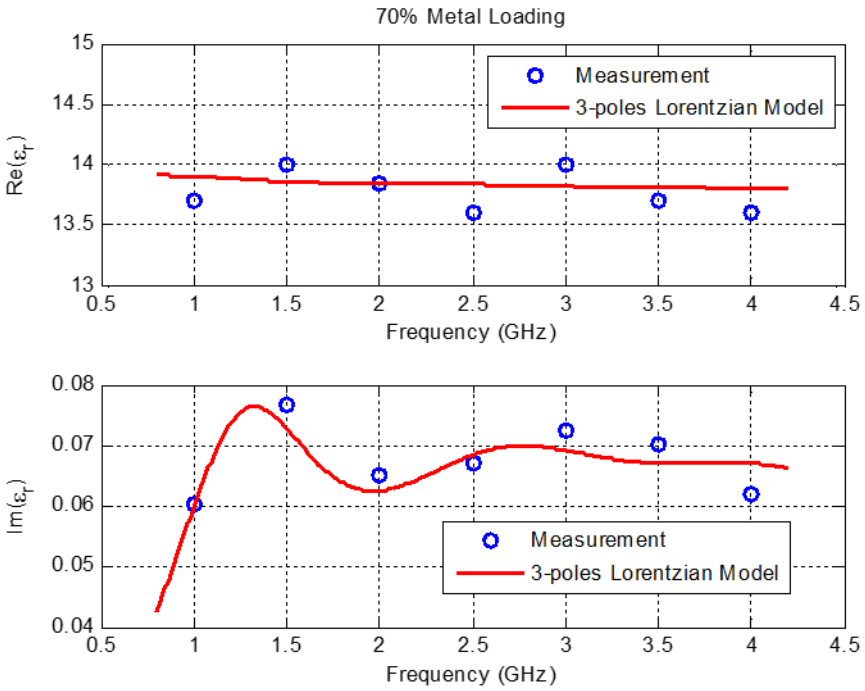

Figure 4.8. Complex permittivity modeling for 70% metal loading sample.

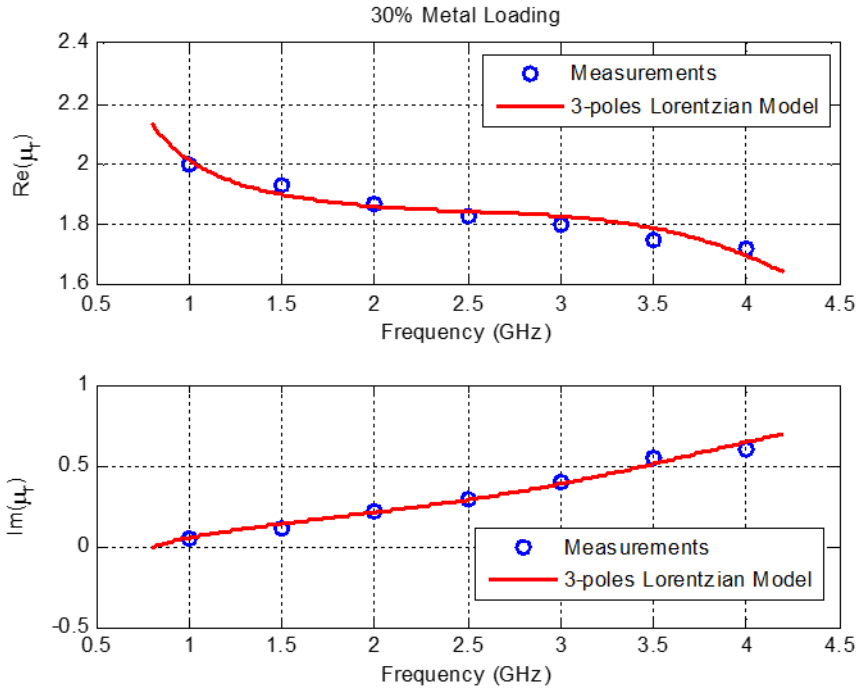

Figure 4.9. Complex permeability modeling for 30% metal loading sample.

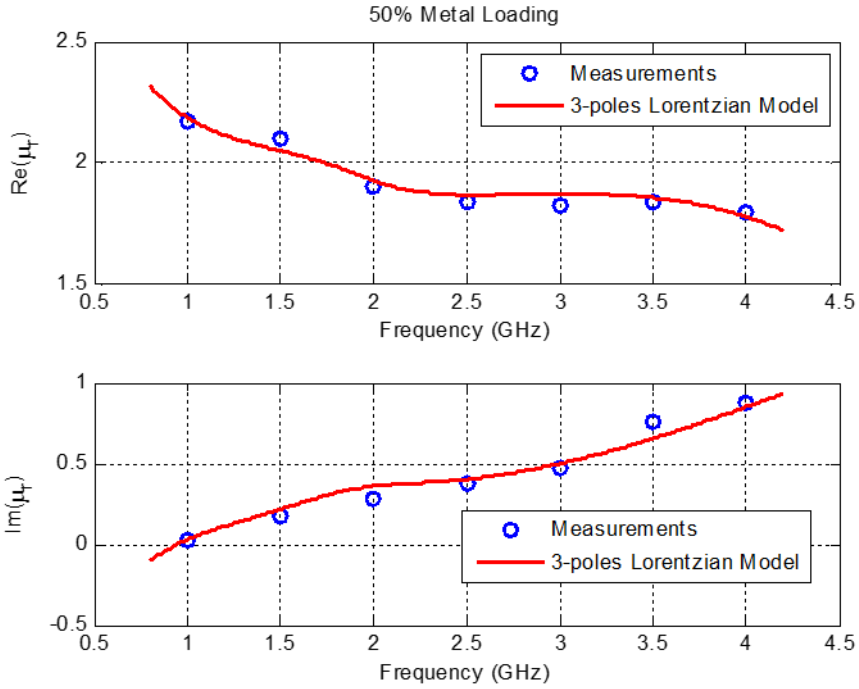

Figure 4.10. Complex permeability modeling for 50% metal loading sample.

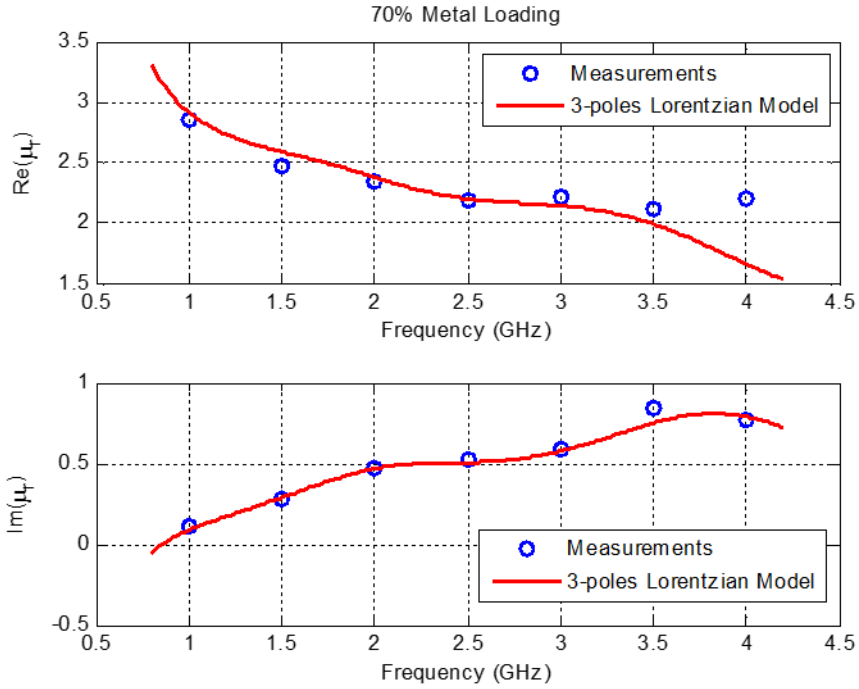

Figure 4.11. Complex permeability modeling for 70% metal loading sample.

4.4 Summary

The three pole Lorentzian dispersion model for fitting extracted material properties of MD materials has been presented. Characterized material properties should be causal and their casualty can be verified using the Kramers-Kronig relations. If the fitting curve model satisfies the Kramers-Kronig relations, it is a causal function, and therefore, the extracted material properties are also causal. In this chapter, the three pole Lorentzian dispersion model has been introduced to fit the extracted MD material properties and the error between the fitted model and extracted data is very small. The error for real permittivity and permeability is less than 2%. Less than 4% and 10% of error have been achieved for fitting the imaginary part of extracted permittivity and permeability, respectively. The fitted model has been shown to satisfy Kramers-Kronig relations, which demonstrates that the extracted MD material properties from the CPT with SIW cavity resonator are causal.

CHAPTER 5

ANTENNA MINIATURIZATION AND SAR REDUCTION

5.1 Introduction

In this chapter, magneto-dielectric material is used as RF antenna substrate to study its merit in the miniaturization of planar antennae. Planar antennae are highly preferred in mobile devices because of their characteristics such as ease of fabrication and integration, compactness and low profile. Microstrip patch antenna and planar inverted-F antenna (PIFA) on magneto-dielectric materials are considered in the following sections.

Through simulations, the performance of the antennae on the magneto-dielectric substrate have been compared with two antennae, one on high dielectric constant material substrate and the other on FR4 material substrate, to demonstrate the advantages of MD material for antenna miniaturization. To investigate effect of material loss on the performance of antennae, the high dielectric constant material is considered for two cases: one with high electric loss tangent and the other with low electric loss tangent. A 900 MHz PIFA on a substrate containing the MD material (using metal polymer system) has been fabricated and its performance measured. The material properties of the synthesized MD material has been extracted using the method discussed in Chapter 3, which were used for antenna simulation. The simulation result was compared to measurements to demonstrate the accuracy of the characterization method.

In addition, the effect of loss characteristics of magneto-dielectric materials on Specific Absorption Rate (SAR) reduction has been studied. Although, the synthesized MD

material using metal-polymer system has reasonable losses by following the design guidelines described in Chapter 2, these losses are in general larger than other low loss dielectric materials. However, the higher losses of MD composite material can help reduce SAR. SAR is a measure of the rate at which energy is absorbed by the human body when exposed to a radio frequency (RF) electromagnetic field [45]. Since the absorbed energy from the RF electromagnetic fields may cause heating of human tissue with potentially dangerous effects, various techniques that can help reduce SAR have been introduced in the literature and they have been reviewed in this chapter. Most of these techniques require extra parts or extra structures between the mobile device and human body, however, an antenna on MD material can achieve the goal without them. In this chapter, SARs of PIFA on different material substrates are compared. The PIFA on MD composite material produced the lowest SAR with antenna performance that meets the requirements of practical handheld devices.

5.2 Magneto-Dielectric Composite Properties

For an antenna substrate, magneto-dielectric composite is synthesized by combining nanosized cobalt metal particles with a fluoropolymer matrix as described in Section 3.5. The synthesized MD material has a metal to polymer volume ratio of around 50:50 and the average crystallite size is 30nm. The frequency dependent dielectric and magnetic properties of the MD material were measured to extract its complex relative permittivity and permeability, with the results shown in Figures 5.1 and 5.2.

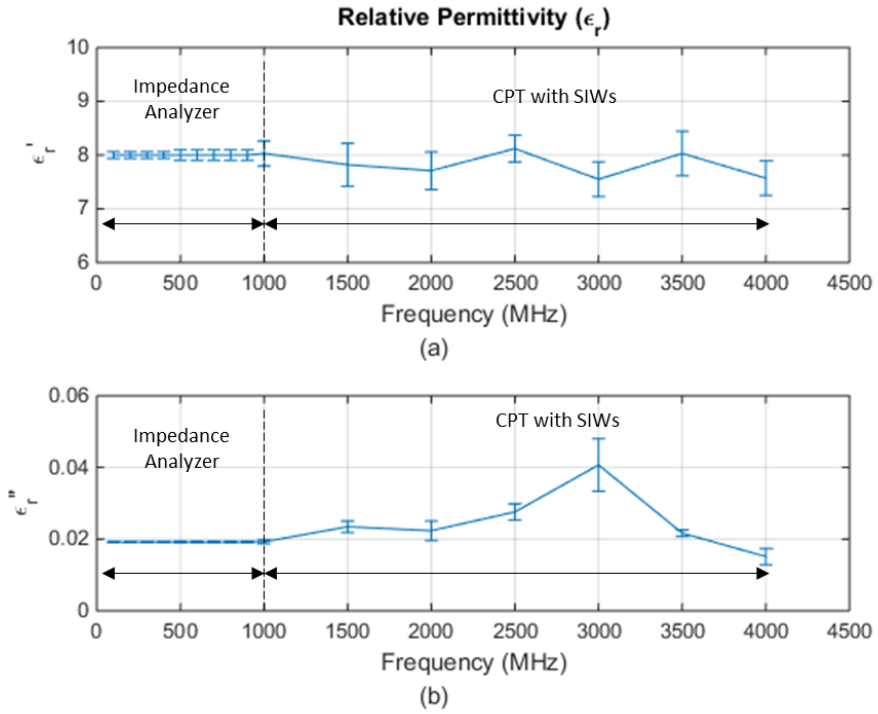

Figure 5.1. Extracted (a) real and (b) imaginary part of relative permittivity of MD material.

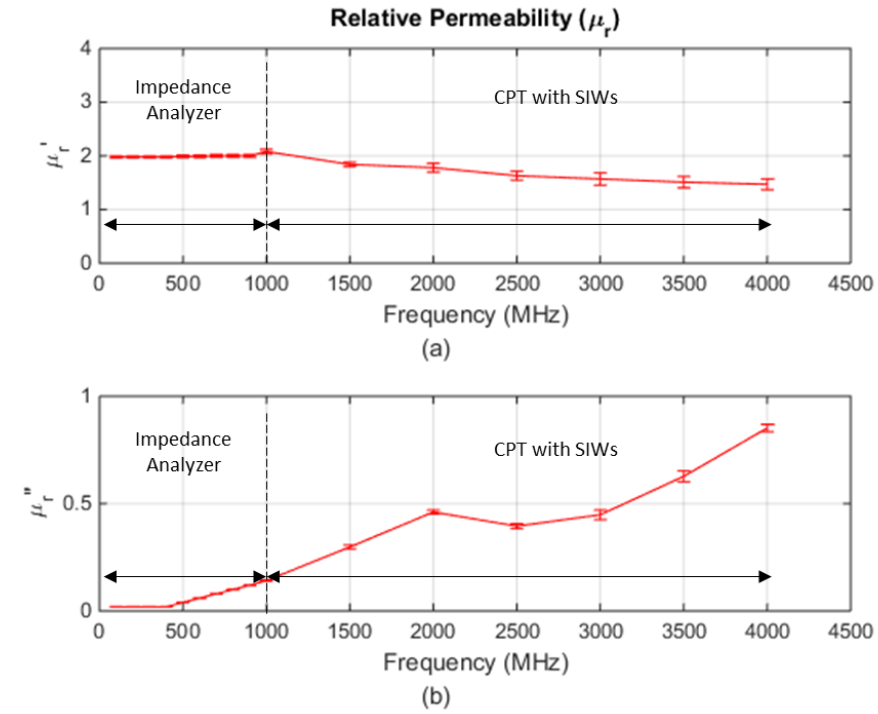

Figure 5.2.Extracted (a) real and (b) imaginary part of relative permeability of MD material.

For material property measurements, an Agilent 4291B impedance analyzer [46] was used up to 1GHz and CPT, which is described in Chapter 3, was used in the frequency range of 1-4GHz. The real part of the relative permittivity is approximately 8, which is fairly constant over the frequency range up to 4GHz. The electric loss tangent shows a maximum value of 0.0054 at 3GHz with a value around 0.0024 at ~1GHz. The real part of the relative permeability is around 2 at ~1 GHz and gradually decreases as the frequency increases as shown in Figure 5.2. As the frequency increases, the magnetic loss tangent value increases. From Figure 5.2, the magnetic loss tangent is below 0.1 up to 1.2 GHz, suggesting a possible use of this material around 1 GHz [47]. These material properties are used for the substrate of the antenna around 1GHz.

5.3 Microstrip Patch Antenna Design

A Microstrip patch antenna is a popular antenna structure when the application requires a broadside radiation pattern with high front-to-back ratio. A 1 GHz microstrip patch antenna on MD material substrate ($PATCH_{MD}$) was designed using CST, as shown in Figure 5.3. The relative permittivity and permeability of the MD material used is 8 and 2 respectively. The electric and magnetic loss tangents of the MD material are 0.0024 and 0.068 at 1GHz respectively. The height of the substrate is 1.52mm. The length of the patch is 36.2 mm and the width of the patch, set as 1.5 times the length of the patch for good radiation, is 54.3 mm. The ground plane was extended 20 mm beyond each side of the patch. The microstrip patch antenna was designed such that only the TM_{10} mode is dominant, and a 50Ω coaxial feed was used for excitation. Another microstrip patch antenna on FR4 substrate ($PATCH_{FR4}$), which has the same resonant frequency of 1GHz, was also designed

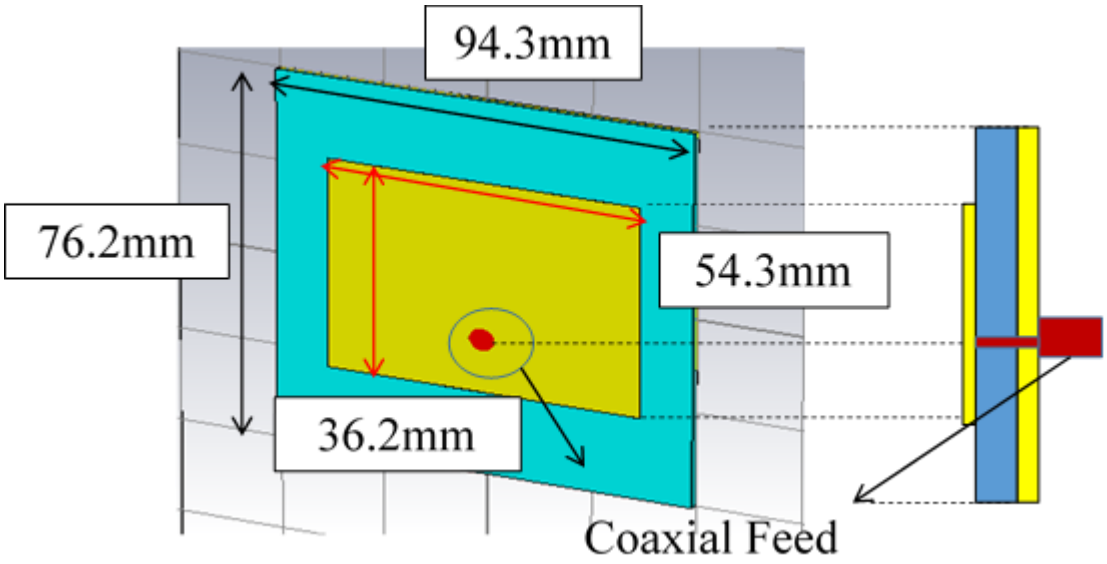

Figure 5.3. Microstrip patch antenna on MD material substrate.

to demonstrate how much the size of the patch antenna is reduced by using the MD material. The relative permittivity of FR4 is 4.3 with a loss tangent of 0.02. As shown in Figure 5.4, the area of the patch antenna on MD substrate is 73.2% smaller than the patch antenna on FR4 substrate. The length and width of the microstrip patch antenna on FR4 substrate is 70 and 105 mm respectively.

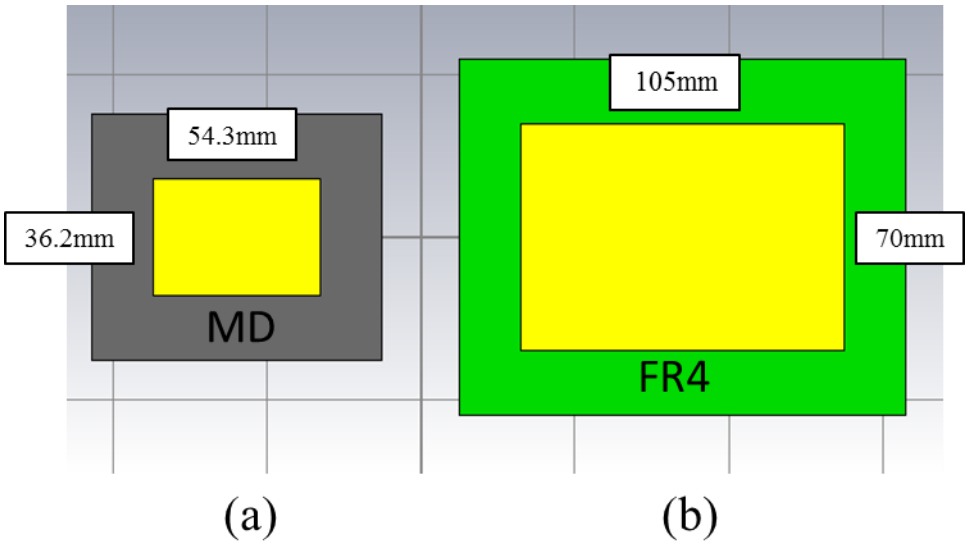

Figure 5.4. Microstrip patch antenna on (a) MD and (b) FR4 substrate.

The performance of $PATCH_{MD}$ was compared to similar patch antennae designed on high dielectric material substrates ($PATCH_{DH}$ and $PATCH_{DL}$) and $PATCH_{FR4}$ to investigate the effect of MD material on the microstrip patch antenna. The relative permittivity of both $PATCH_{DH}$ and $PATCH_{DL}$ was chosen as 15.5 to make sure that the antennae have the same resonant frequency of 1GHz, without changing the dimensions of the patch. The loss tangent of $PATCH_{DH}$ was chosen as 0.0704 which is the sum of the electric and magnetic loss tangent of the MD material, and the loss tangent of $PATCH_{DL}$ was selected as 0.002 (virtual material). DH and DL represents high dielectric constant materials with high and low loss respectively. Two different losses of patch antennae on the same dielectric constant material were used to see the effect of loss on antenna performance. The position of the coaxial feed was optimized to ensure that all antennas work with the best matching condition.

Bandwidth, efficiency and gain of the four antennas were compared. Figure 5.5 shows the simulated return loss for all antennae.

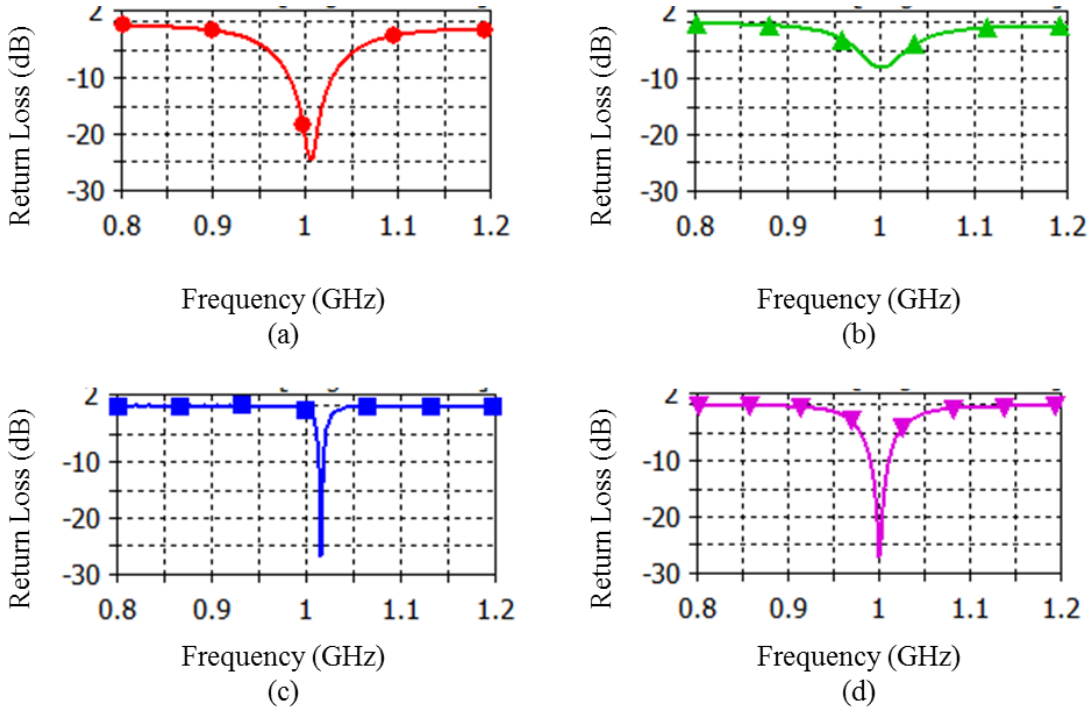

Figure 5.5. Simulated return loss of (a) $PATCH_{MD}$, (b) $PATCH_{DH}$, (c) $PATCH_{DL}$ and (d) $PATCH_{FR4}$.

For the bandwidth comparison, VSWR=3:1 (~6dB) was considered since the $PATCH_{DH}$ could not satisfy the VSWR=2:1 condition. As shown in Figure 5.5, $PATCH_{MD}$ shows the widest bandwidth of 7.9% among all four antennae. As discussed earlier, increasing the permittivity of substrate material reduces the bandwidth which has been demonstrated through these simulation results. The patch antenna on MD substrate shows wider bandwidth than the patch antenna on FR4 substrate. The microstrip patch antenna inherently shows narrow bandwidth but this bottleneck can be resolved by using MD material. The bandwidth of VSWR=3:1 of the four antennae are shown in Figure 5.6.

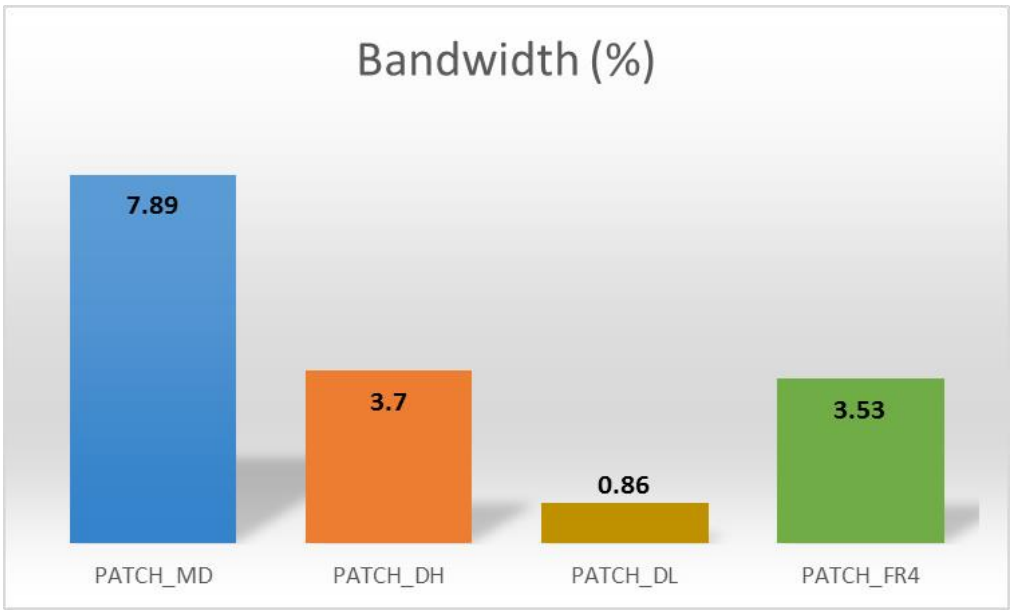

Figure 5.6. Histogram bandwidth for four microstrip patch antennae.

The simulation results of the radiation efficiency and peak gain are presented in Figures 5.7 and 5.8 respectively. The patch antenna on MD substrate shows radiation efficiency and gain of 8.2% and -6.746 dBi. $PATCH_{MD}$ shows higher radiation efficiency and gain than $PATCH_{DH}$. A high dielectric constant in the substrate results in higher stored energy inside of the substrate between top patch and bottom ground, and therefore, the $PATCH_{DH}$ radiation efficiency and gain are much lower compared to the patch antenna on MD material. $PATCH_{DL}$ shows 37.53% radiation efficiency which is about 4 times higher than that of $PATCH_{MD}$. As the loss tangent of the high dielectric constant material substrate reduces to 0.002 from 0.0704, the performance of the patch antenna improved significantly. Based on the comparison, it is necessary to reduce the loss of MD material to increase its

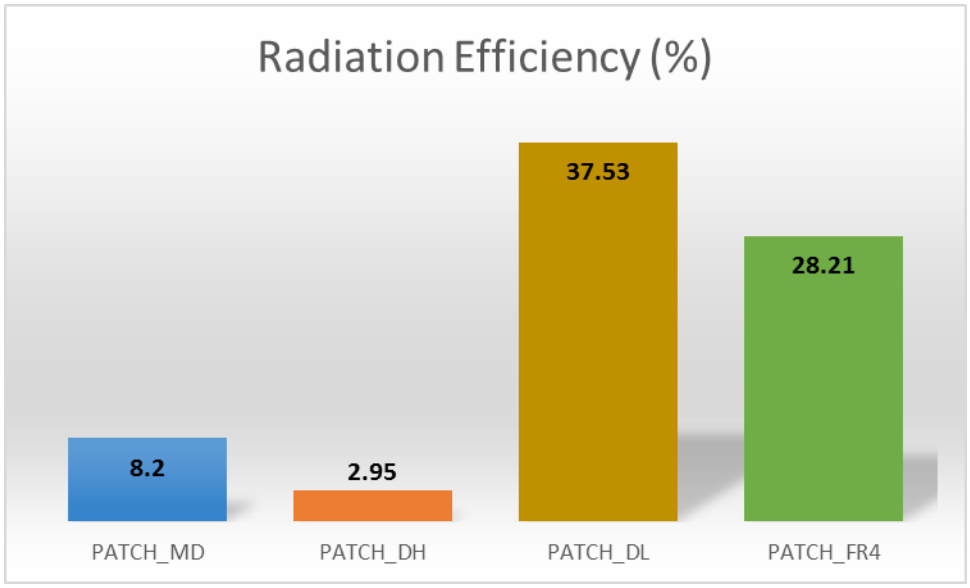

Figure 5.7. Histogram radiation efficiency for four microstrip patch antennae.

benefit for antenna miniaturization. If the total loss of the MD material is improved using enhanced material synthesis, antennae on MD material substrates can show better radiation efficiency and gain than antennae on high dielectric constant materials with low loss. $PATCH_{FR4}$ shows the best gain amongst the four antennae and this can be attributed to low permittivity with moderate loss, but with the largest antenna area.

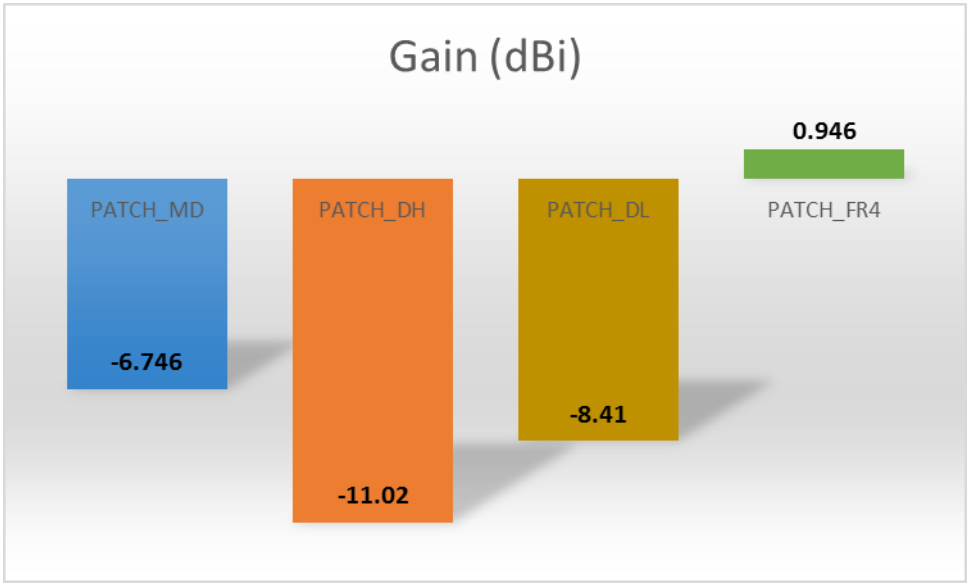

Figure 5.8. Histogram gain for four microstrip patch antennae.

5.4 Planar Inverted-F Antenna (PIFA) Design

Although microstrip patch antennae have merits for mobile application, it usually shows low radiation efficiency due to a conductor backed ground plane. In this section, MD material is applied to another popular kind of antenna known as the planar inverted-F antenna (PIFA). PIFA is very similar to the microstrip patch antenna except for shorting the patch to ground. By introducing this shorting pin, a quarter-wavelength size patch in PIFA can resonate at the same frequency as a half-wavelength size microstrip patch antenna.

A meander PIFA working at 900 MHz was designed on MD material substrate as shown in Figure. 5.9. The relative permittivity and permeability of the MD material used for design were 8 and 2 at 900MHz respectively, based on the measured values from Figure 5.1 and 5.2. $Tan\delta_e$ and $Tan\delta_m$ of the MD material used were 0.0024 and 0.068 at 900MHz respectively. Figure 5.9 shows the geometry of the proposed antenna on the MD material substrate above an FR4 PCB with a relative permittivity of 4.3 and $tan\delta_e$ of 0.02. The overall size of the FR4 PCB substrate is 60 mm x 120 mm x 1mm. The size of the MD material substrate is 20 mm x 20 mm x 1 mm where the meander copper trace was patterned on top of the substrate. The meander top plane was shorted to ground with 2mm width copper tape at the top left corner of the antenna. A 50Ω coaxial feed was connected to the top metal plane for excitation and the distance between the shorting pin and feed was optimized to have good impedance matching using CST simulation. No extra matching network was used in order to minimize components.

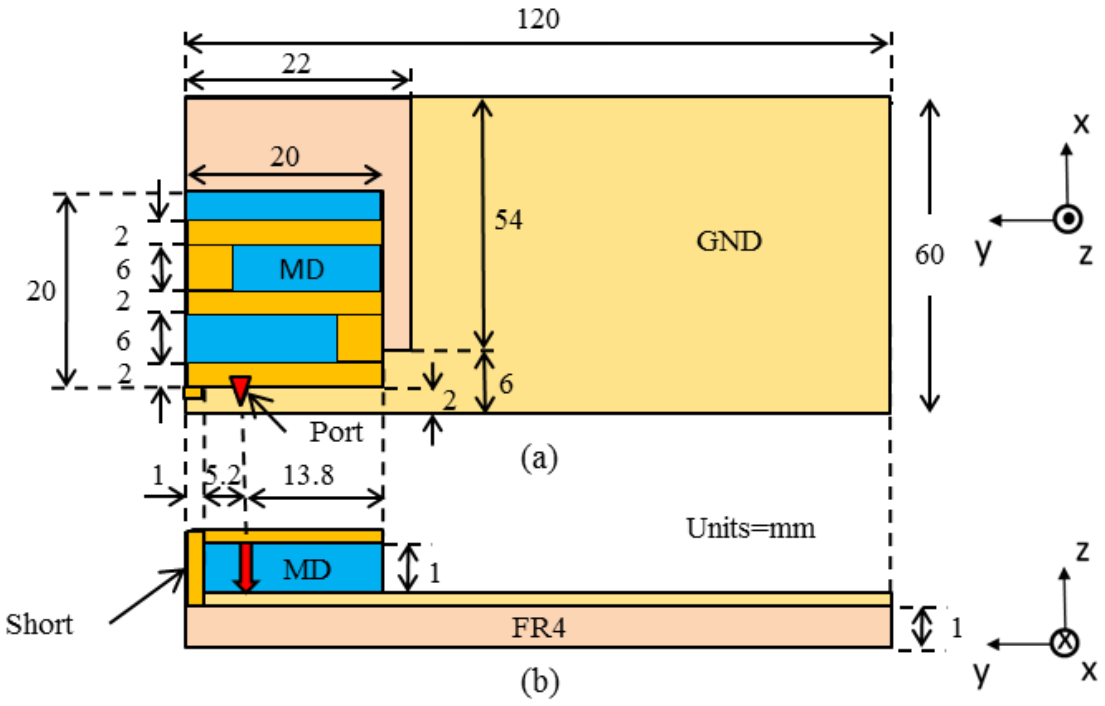

Figure 5.9. Geometry of the proposed PIFA on MD material substrate (a) top view and (b) side view.

The PIFA on the MD material substrate ($PIFA_{MD}$) was compared to similar antennae designed on high dielectric material substrates ($PIFA_{DH}$ and $PIFA_{DL}$) and FR4 substrate ($PIFA_{FR4}$), to compare the effect of MD on antenna performance. The relative permittivity of both $PIFA_{DH}$ and $PIFA_{DL}$ was chosen as 15.1 to ensure that the antennas resonated at the same frequency as $PIFA_{MD}$ without having to change the dimensions of the antenna. $Tan\delta_e$ of $PIFA_{DH}$ was chosen as 0.0704 which is the sum of the electric and magnetic loss tangent of MD material at 900MHz. $Tan\delta_e$ of 0.002 was used for $PIFA_{DL}$ to determine the effect of high dielectric constant with low loss on antenna performance. DH and DL represent high dielectric materials with high and low loss respectively. The relative permittivity of $PIFA_{FR4}$ was 4.3 with a loss tangent of 0.02 and the antenna size was

optimized to make the antenna resonate at 900 MHz as well. As shown in Figure 5.10, the area of the $PIFA_{MD}$ is 20 x 18 = 360mm^2 and the area of the $PIFA_{FR4}$ is 20 x 28 = 560mm^2. The size of antenna on MD material substrate is 39% smaller than FR4 substrate. It was observed that antenna size reduction ratio is smaller for the PIFA type than the patch antenna type. This is because the effective permittivity and permeability of the MD material substrate in PIFA case would be smaller than the MD material substrate for patch antenna since there is no conductor ground backing for PIFA. Removing the conductor ground backing, however, can help increase the radiation efficiency and gain of the antenna.

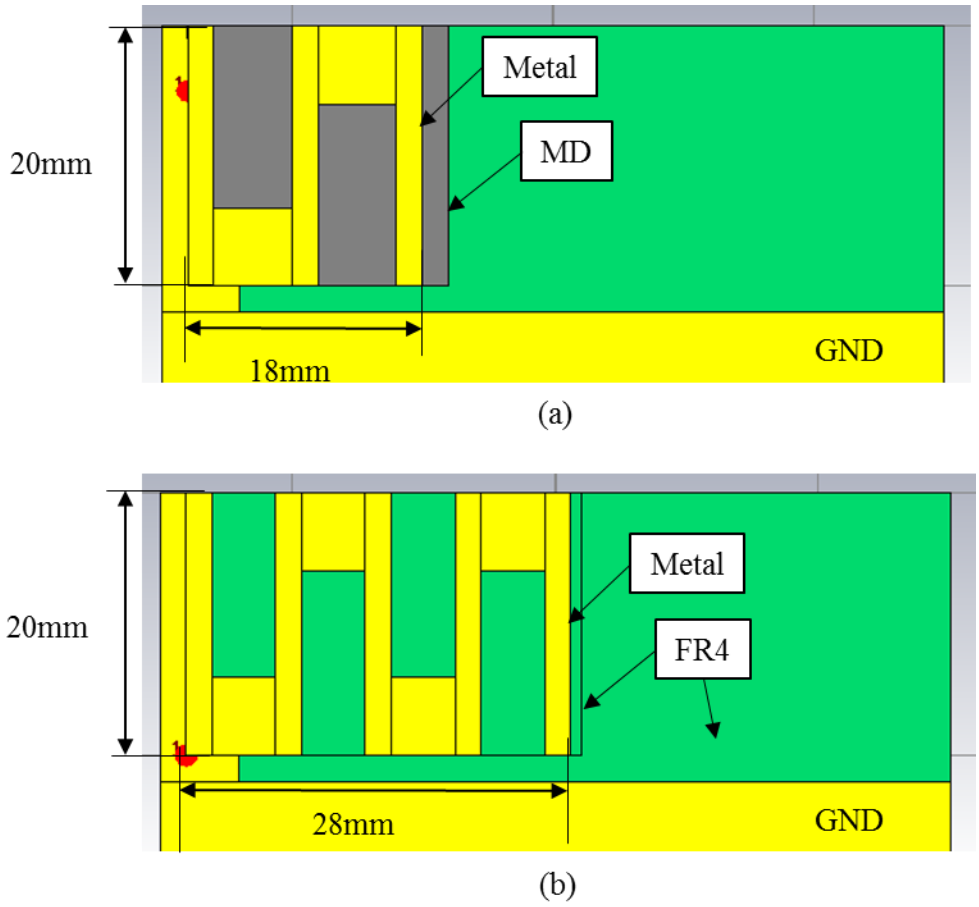

Figure 5.10. Antenna size comparison (a) $PIFA_{MD}$ and (b) $PIFA_{FR4}$.

Bandwidth, efficiency and gain of the four antennae were compared. Figure 5.11 shows the simulated return loss for all antennae.

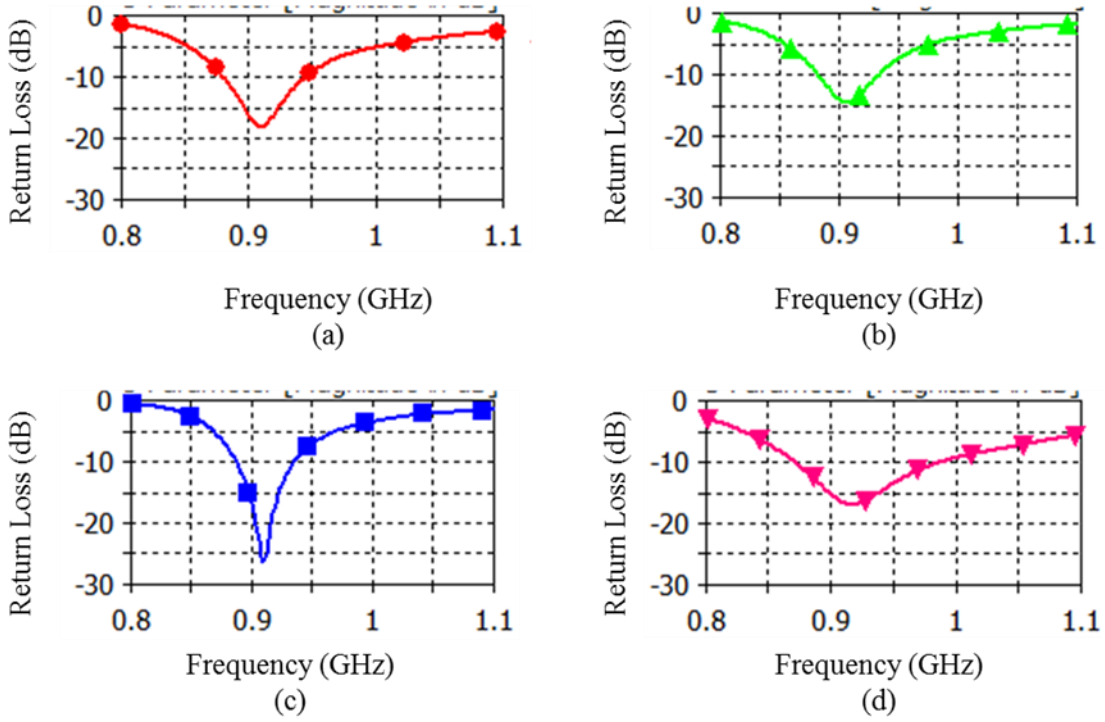

Figure 5.11. Simulated return loss of (a) $PIFA_{MD}$, (b) $PIFA_{DH}$, (c) $PIFA_{DL}$ and (d) $PIFA_{FR4}$.

A VSWR=2:1 condition was applied to compare the bandwidth and it was observed that antennae on high dielectric material substrates, $PIFA_{DH}$ and $PIFA_{DL}$, showed narrow bandwidth as compared to $PIFA_{MD}$. $PIFA_{MD}$ shows 7.24% bandwidth while $PIFA_{DH}$ and $PIFA_{DL}$ showed 5.5% and 5.14% bandwidth, respectively, as shown in Figure 5.12. The bandwidth is proportional to the material loss, however, $PIFA_{MD}$ shows wider bandwidth than $PIFA_{DH}$ even though they have the same total loss. It was observed that $PIFA_{MD}$ shows better bandwidth than $PATCH_{MD}$ (4.41% when VSWR=2:1) due to the removal of the conductor ground backing.

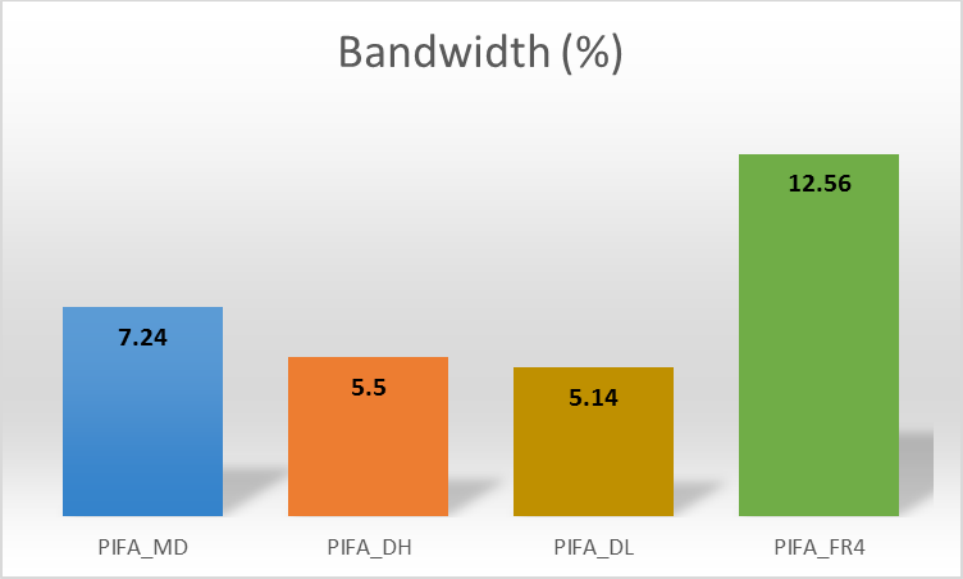

Figure 5.12. Histogram bandwidth for four PIFAs.

The simulation results of the radiation efficiency and peak gain are presented in Figures 5.13 and 5.14 respectively. A similar trend as that shown in section 5.3 is also observed. $PIFA_{MD}$ shows higher radiation efficiency and gain than $PIFA_{DH}$. Increased stored energy inside of the high dielectric material of $PIFA_{DH}$ results in lower radiation efficiency and gain than $PIFA_{MD}$. Therefore, an antenna on an MD material substrate provides better antenna performance than an antenna on a high dielectric material substrate when they have the same total loss. On the other hand, $PIFA_{DL}$ shows 15% higher radiation efficiency and 0.5 dBi better gain than $PIFA_{MD}$. The low loss in the substrate of $PIFA_{DL}$ increases the antenna performance and this performance gap between $PIFA_{DL}$ and $PIFA_{MD}$ can be decreased by reducing the loss of the MD material. However, such low loss is difficult to achieve for MD materials due to the presence of the metal particles. $PIFA_{FR4}$ showed the widest bandwidth as well as the highest radiation efficiency and gain among all four antennae. The best antenna performance of $PIFA_{FR4}$ can be due to the lowest

permittivity with low loss and larger antenna area. It has been shown that antenna performance deterioration is inevitable when the antenna size is reduced. MD material, however, can be used to minimize this problem during antenna miniaturization.

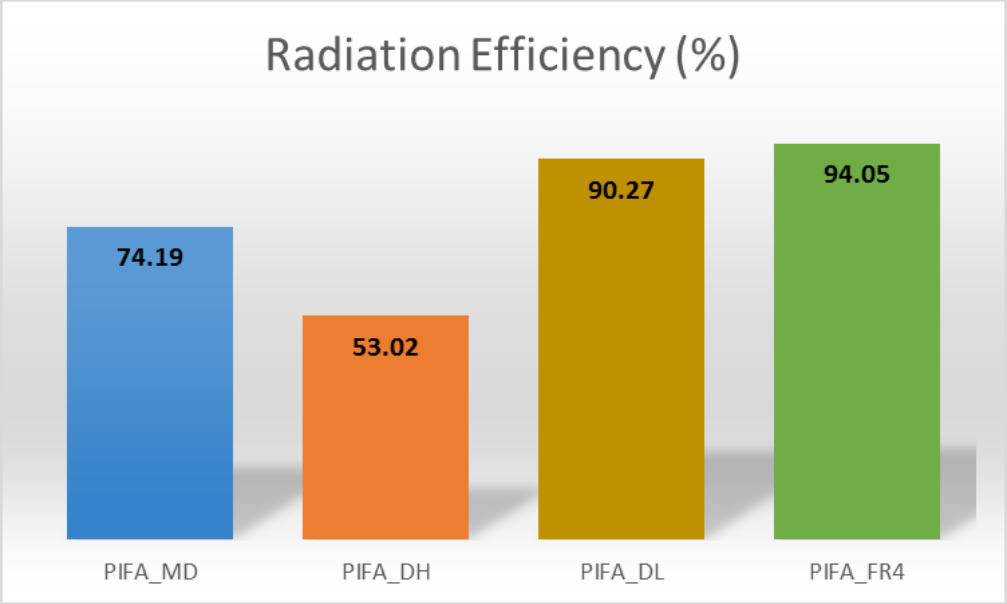

Figure 5.13. Histogram radiation efficiency for four PIFAs.

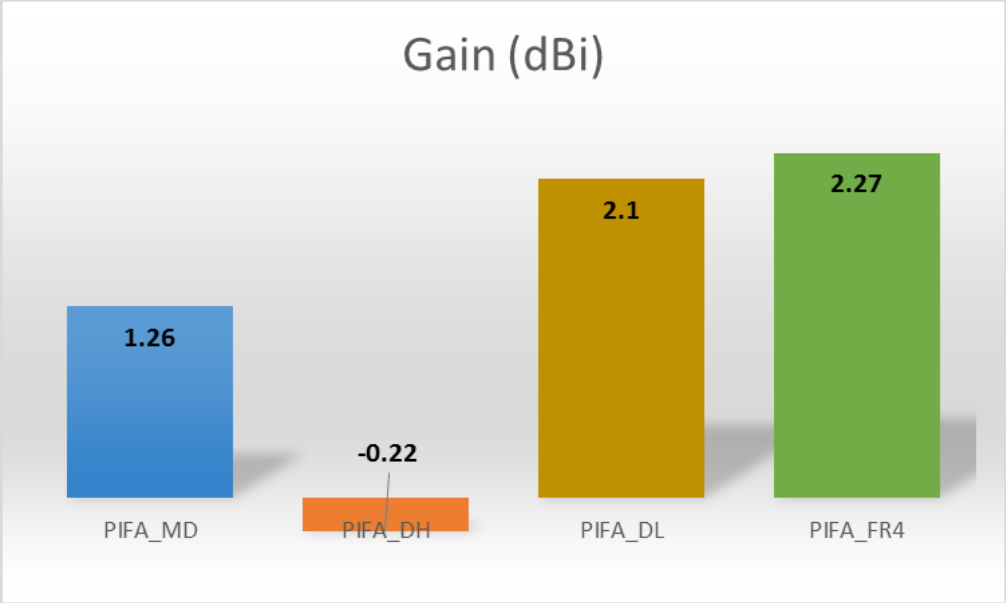

Figure 5.14. Histogram gain for four PIFAs.

5.5 Specific Absorption Rate (SAR) reduction techniques

The Specific Absorption Rate (SAR) is a parameter for calculating the amount of power from EM field that is absorbed in human tissue. SAR has units of watts per kilogram (W/Kg) and it is usually averaged either over the whole body, or over a small sample volume (typically 1g or 10g of tissue) [45]. It can be expressed as:

$$SAR = \int_{sample} \frac{\sigma(r)\left|E(r)\right|^2}{\rho(r)} dr, \tag{44}$$

where σ is the sample electrical conductivity, E is the RMS electric field, and ρ is the sample density. SAR measures exposure to fields between 100 kHz and 10 GHz. The value depends heavily on the geometry of the part of the body that is exposed to the RF energy, and on the exact location and geometry of the RF source. Thus testing is required for each specific source at the intended position of use [45].

In order to reduce SAR in the human tissue, structures such as electromagnetic bandgap (EBG) structures [48], [49] have been integrated between the antenna and ground plane or metamaterials can be used by arranging periodic resonators [50], [51] which have been placed between the human head and the antenna. Figure 5.15 shows SAR reduction techniques that use EBG structures.

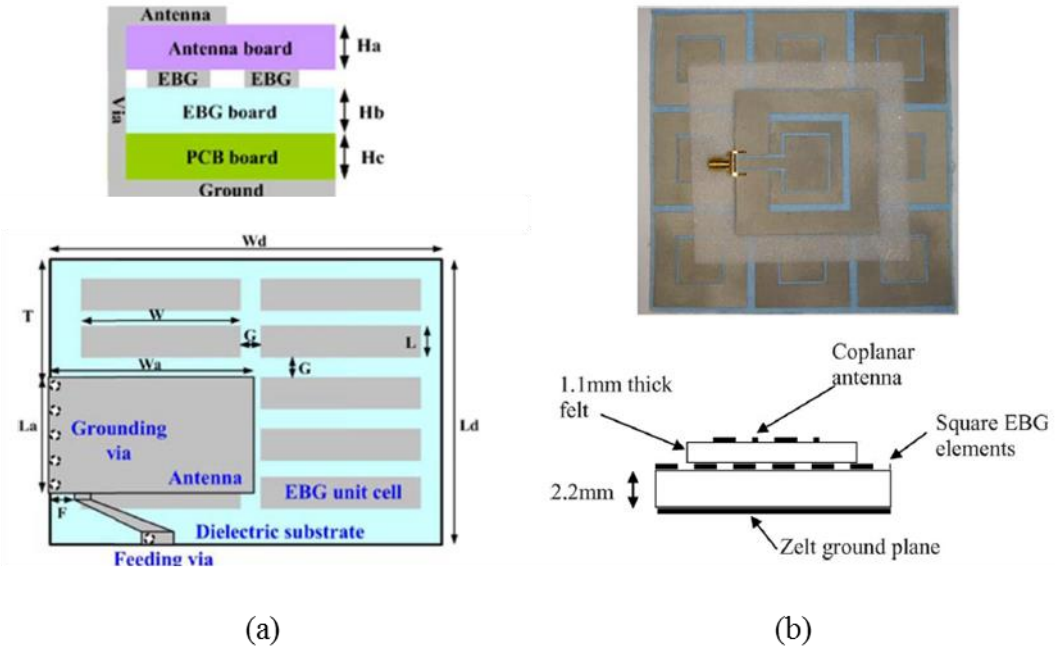

Figure 5.15. Examples of SAR reduction using EBG structure (a) PIFA [48] and (b) Dual-band coplanar antenna [49].

In Kwak *et al*. [48], an optimized multilayer PIFA with an EBG for SAR reduction has been introduced for personal communication services band, as shown in Figure 5.15 (a). The EBG structure was used to prevent EM fields being emitted in the direction of the human head. To reduce SAR, the EBG structure was inserted between the printed circuit board and antenna layer and the EBG cell numbers, height, and location of the PIFA with the EBG structure has been optimized. About 36.67% reduction of SAR, averaged on 1g of tissue, has been achieved with this proposed structure based on simulation. In Zhu *et al*. [49], a dual-band coplanar patch antenna on common clothing fabrics was designed for body-worn communications systems. An EBG substrate had been integrated between the antenna substrate and ground plane to decrease SAR in the human head, as shown in Figure 5.15. (b). The antenna with EBG patches reduced SAR by 96.5% for 1g of tissue.

Figure 5.16 shows another technique using the metamaterial structures for SAR reduction. In Hwang *et al* [50], split ring resonators (SRRs) were arranged periodically to obtain the metamaterial properties, as shown in Figure 5.16 (a). Placing the metamaterial between the antenna and muscle cube resulted in an SAR reduction of 27.57% and 37.62% at 900 and 1800MHz respectively. Similarly in Faruque *et al* [51], the metamaterial using triangular split ring resonators (TSSRs) was placed between the antenna and human head. The SAR reduction was 45.44%.

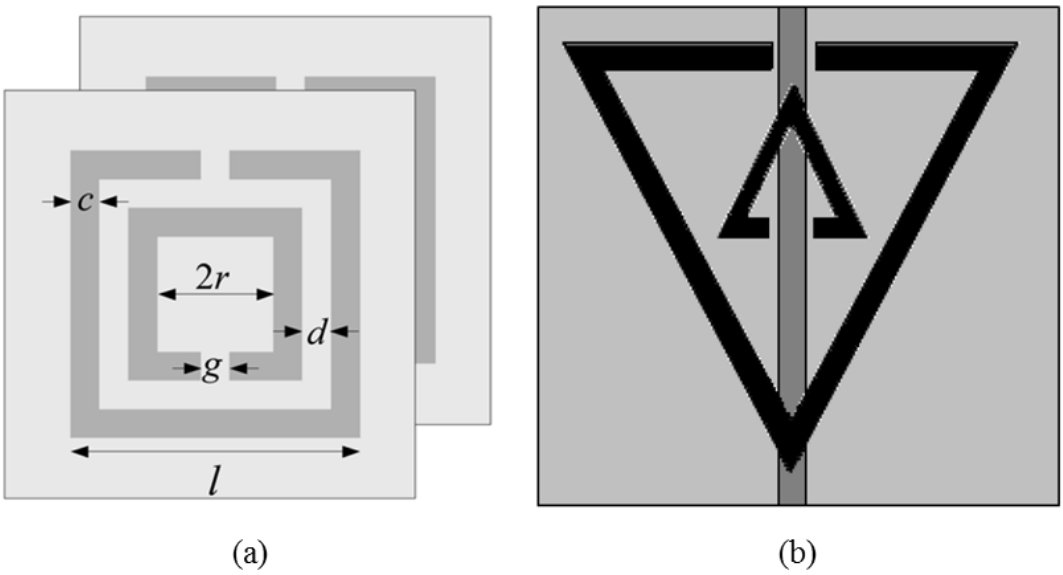

Figure 5.16. Examples of SAR reduction using metamaterials obtained by (a) split ring resonators (SRRs) [50] and (b) triangular split ring resonators (TSSRs) [51].

Ferrite materials for EM shielding have also been used to reduce SAR [52]. Even though these techniques help reduce SAR, they require extra substrates or extra materials between the antenna and the human body. The antenna size will increase using these kind of techniques and, therefore, a different approach for SAR reduction to minimize antenna size is necessary. In the following sections, the SAR of an antenna on MD material and the

effect of loss characteristics of MD material on SAR reduction are discussed as an alternate solution.

5.6 PIFA on MD composite material and SAR reduction

The PIFA on MD composite material substrate in Figure 5.9 was used to analyze the effect of MD composite material on SAR reduction. The PIFA was covered using a plastic case and LCD film to model a realistic cellphone structure, as shown in Figure 5.17.

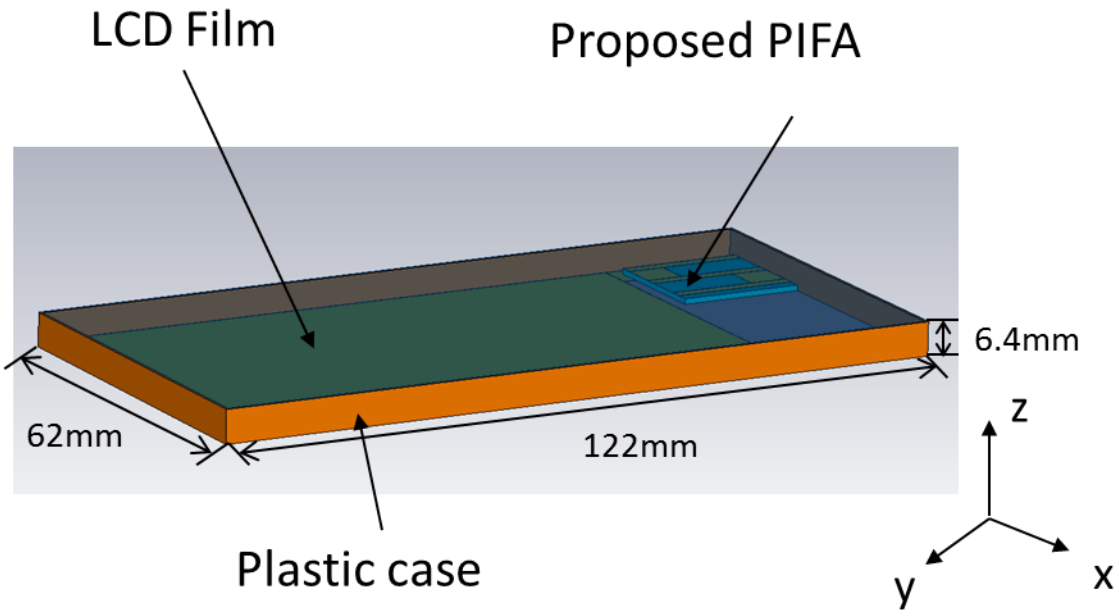

Figure 5.17. Cellphone structure for SAR analysis.

The dielectric constants of the plastic case and LCD film were 2.5 and 4.78 respectively. The heights of plastic and LCD film were 500 and 200um respectively. In this section, the effect of loss characteristics of the MD material on SAR is studied by comparing $PIFA_{MD}$, $PIFA_{DL}$ and $PIFA_{FR4}$ cases. The antenna specification for each PIFA is the same as described in Section 5.4.

Three antennas' xz-plane radiation patterns have been simulated using CST to evaluate front-to-back ratio as shown in Figure 5.18.

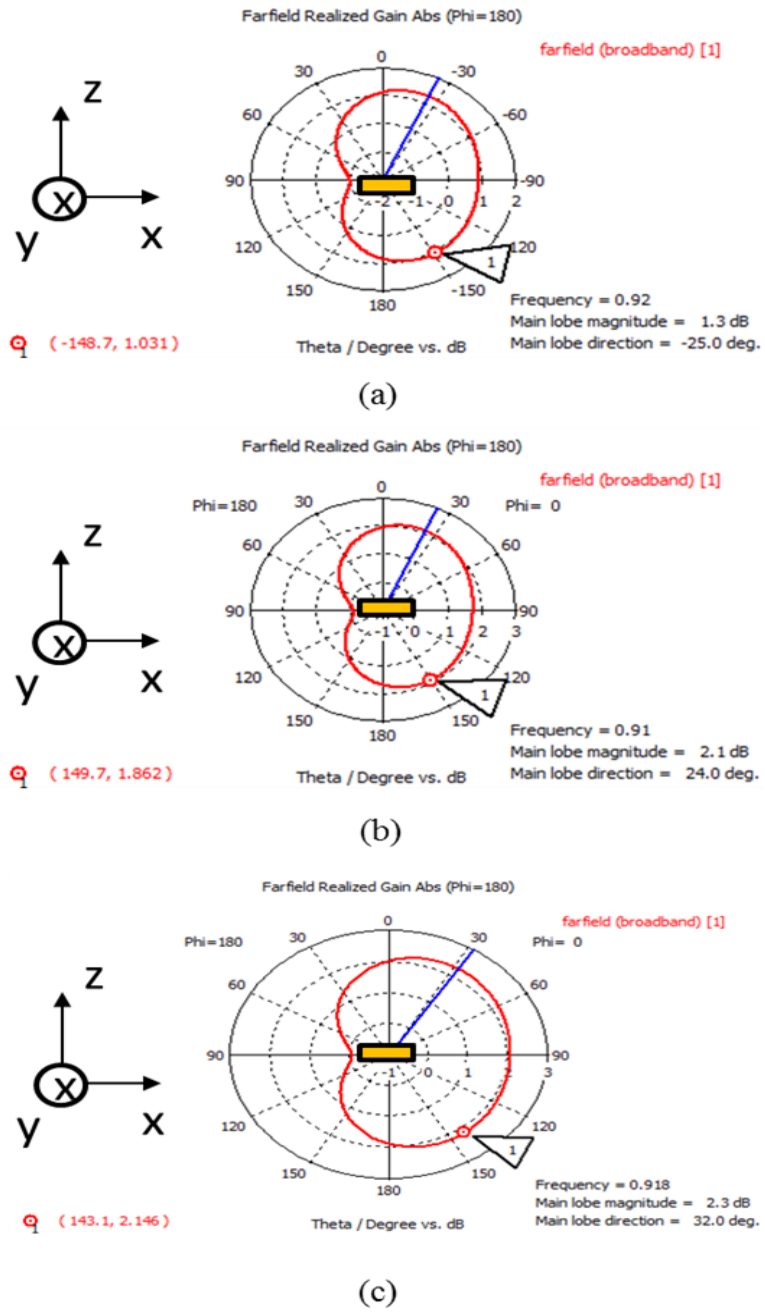

Figure 5.18. xz-plane radiation patterns of (a) $PIFA_{MD}$, (b) $PIFA_{DL}$ and (c) $PIFA_{FR4}$.

Antenna gain patterns for each PIFA were calculated at their own resonant frequency. Lower radiation energy to the back side of the antenna is required to reduce the energy propagating into the human body. The lower back radiation, however, can represent that the antenna does not radiate at all, therefore, the peak gain obtained from the back side of the PIFA was divided by the peak gain obtained from the front side of the PIFA to calculate the back-to-front ratio. If this ratio is small, less energy radiates to back side and it will reduce the SAR of the antenna. A gain of 1.031 and 1.3dB were obtained for the back and front radiation pattern, respectively for $PIFA_{MD}$, resulting in 79.3% of the front side radiation energy radiating to the back side of $PIFA_{MD}$. Using the same calculation, 88.67 and 93.3% of front side radiation energy radiated as back radiation for $PIFA_{DL}$ and $PIFA_{FR4}$ respectively. $PIFA_{MD}$ shows the best front-to-back ratio and the smallest back radiation amongst the three antennas and these results demonstrate that PIFA on MD material can result in a smaller SAR with good radiation characteristics. The front-to-back ratio of three antennae are summarized in Table 8.

Table 8. Front-to-back ratio of three PIFAs.

Ant. Type	f_r (MHz)	Front gain (dB)	Back gain (dB)	BF ratio (%)
$PIFA_{MD}$	920	1.3	1.031	79.3
$PIFA_{DL}$	910	2.1	1.862	88.67
$PIFA_{FR4}$	918	2.3	2.146	93.3

To study the effect of the MD composite material on SAR reduction, two human body models, head and leg, were used as shown in Figure 5.19. An EN 50361 Specific Anthropomorphic Mannequin (SAM) phantom head, which is provided in CST microwave studio, was used for the human head model (Figure 5.19. (b)), and a cylinder shape model with four layers, bone, muscle, fat and skin was used for the human leg model (Figure 5.19. (c)).

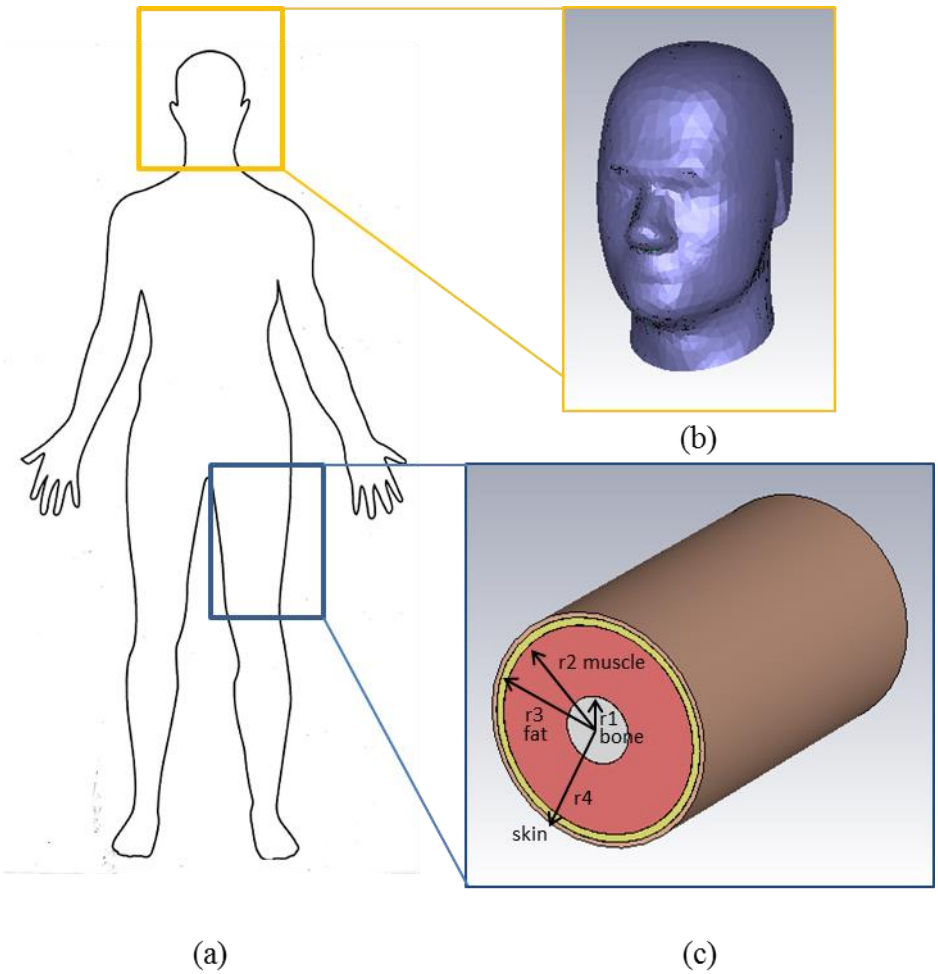

Figure 5.19. Picture of human body model of (a) outline drawing [53], (b) SAM head and (c) leg.

The phantom head consists of a shell filled with a liquid which represents the average material properties of the human head. The relative permittivity and loss tangent of shell and liquid were 5/0.05 and 42/0.53 respectively. The density of liquid was 1000kg/m^3 and the specification of the phantom head model is summarized in Table 9.

Table 9. Specification of Human head model.

Layer	ε_r	Loss tangent	Density (kg/m^3)
Shell	5	0.05	N/A
Liquid	42	0.53	1000

The leg model consists of four layers of human tissue and the relative permittivity and conductivity (s/m) of bone, muscle, fat and skin were 12.45/0.143, 56.87/0.995, 5.46/0.051, 41.4/0.867 respectively. The material density and radius of each human tissue are summarized in Table 10.

Table 10. Specification of human organ tissues [54]

Tissue	ε_r	Kappa (s/m)	Rho (kg/m^3)	Radius (mm)
Bone	12.45	0.143	1850	15
Muscle	56.87	0.955	1040	70
Fat	5.46	0.051	1100	73
Skin	41.40	0.867	1100	75

The cellphone structure in Figure 5.17 was placed around 10mm away from the left hand side of the head to study SAR on human head, as shown in Figure. 5.20.

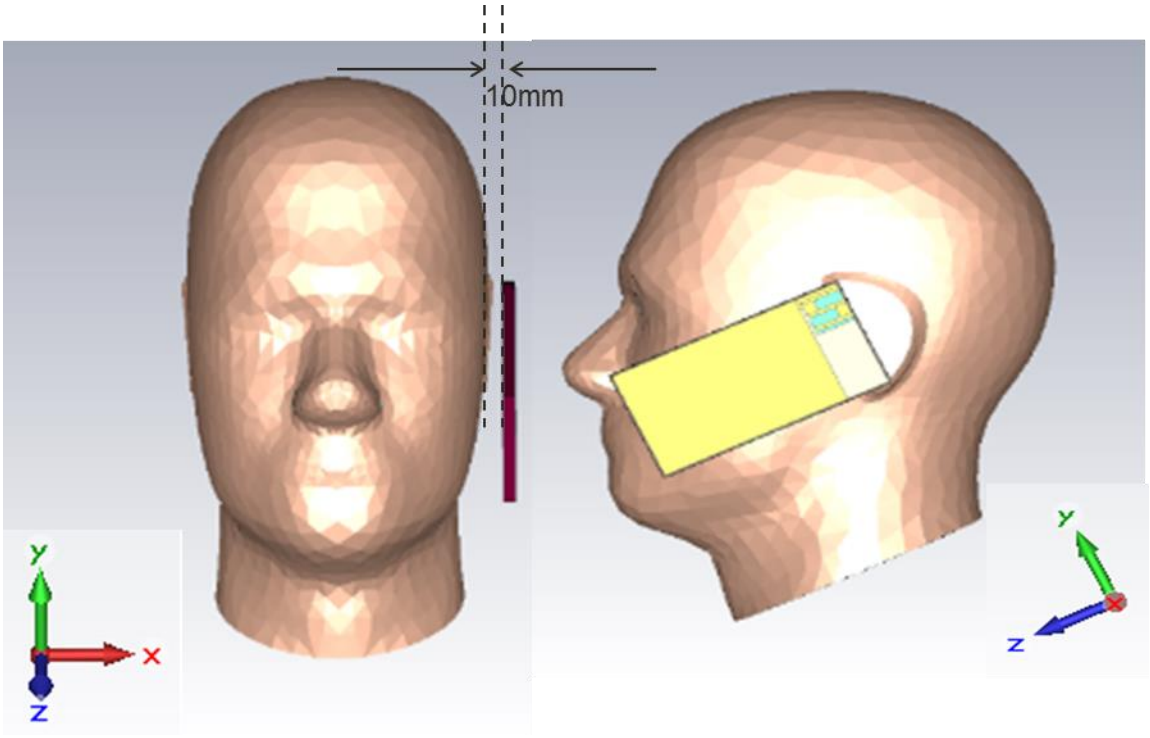

Figure 5.20. Antenna orientation with SAM phantom mannequin.

The resonant frequency, bandwidth, peak efficiency, peak gain and maximum SAR of each antenna were calculated and are summarized in Table 11. The resonant frequencies of the PIFAs were shifted as they were placed close to the head. The resonance shift of the $PIFA_{MD}$ due to the head was 72.77 MHz, which is 17MHz and 19 MHz less than that of the $PIFA_{DL}$ and $PIFA_{FR4}$ respectively. The reason for $PIFA_{MD}$ showing the smallest resonance shift is due to the refractive index ($n=\sqrt{\varepsilon_r \mu_r}$) of MD, which is closest to the refractive index of the head amongst the three materials. The bandwidth with 2:1 VSWR are 7.1, 3.19 and 5.08% for $PIFA_{MD}$, $PIFA_{DL}$ and $PIFA_{FR4}$ respectively. $PIFA_{MD}$ showed the largest bandwidth among all three antennas. The radiation efficiency of standalone $PIFA_{MD}$ was about 15~20% lower than the PIFA on other substrates, but when the antennae were placed close to the head, the difference between them was only 1~2%. Although the peak radiation efficiency and peak gain of $PIFA_{MD}$ were the lowest among all three antennae, the deterioration of these values by the head phantom was the smallest among them. Therefore, human head effects on antenna performance can be decreased by using MD material compared to using high dielectric constant material or FR4. Figure 5.21 shows the simulated maximum SAR inside of the head for each PIFA.

Table 11. PIFAs performance with head phantom

Specification	$PIFA_{MD}$	$PIFA_{DL}$	$PIFA_{FR4}$
Δf_r (MHz)	72.77	90	92.33
Bandwidth (%)	7.1	3.19	5.08
Efficiency (%)	18.17	19.54	20.49
Gain (dB)	-2.61	-2.33	-2.05
Max SAR (W/kg)	0.722	0.853	0.854

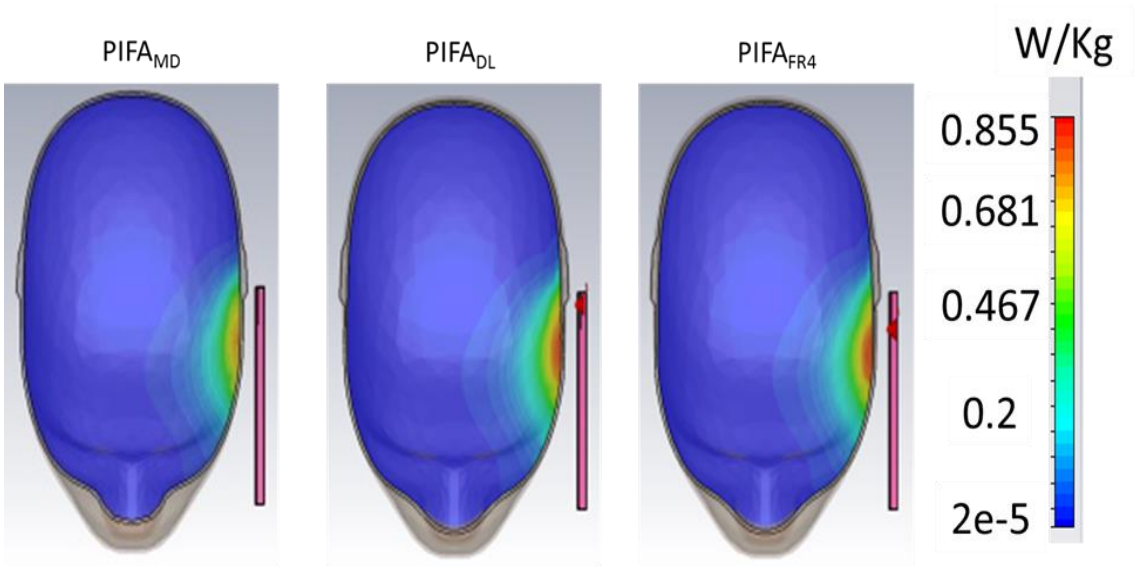

Figure 5.21. Maximum SAR comparison.

PIFA$_{MD}$ showed the lowest maximum SAR amongst the three antennae. The region of energy propagating into the head can be seen in the SAR distribution plot in Figure 5.21. The antenna using the MD material also showed the smallest area. The calculated SAR of PIFA$_{MD}$ was 0.722W/kg averaged over 1g of tissue with a 100mW input power. The other two antennas showed a maximum SAR of 0.853 and 0.854W/kg for PIFA$_{DL}$ and PIFA$_{FR4}$ respectively. About 15.3% reduction in SAR is achieved using the MD material and this significant reduction in SAR can be attributed to the magnetic loss tangent of the MD material.

The cellphone structure in Figure 5.17 was also placed close to the leg model for further SAR study, as shown in Figure 5.22. The antenna was placed 5mm away from the human body model.

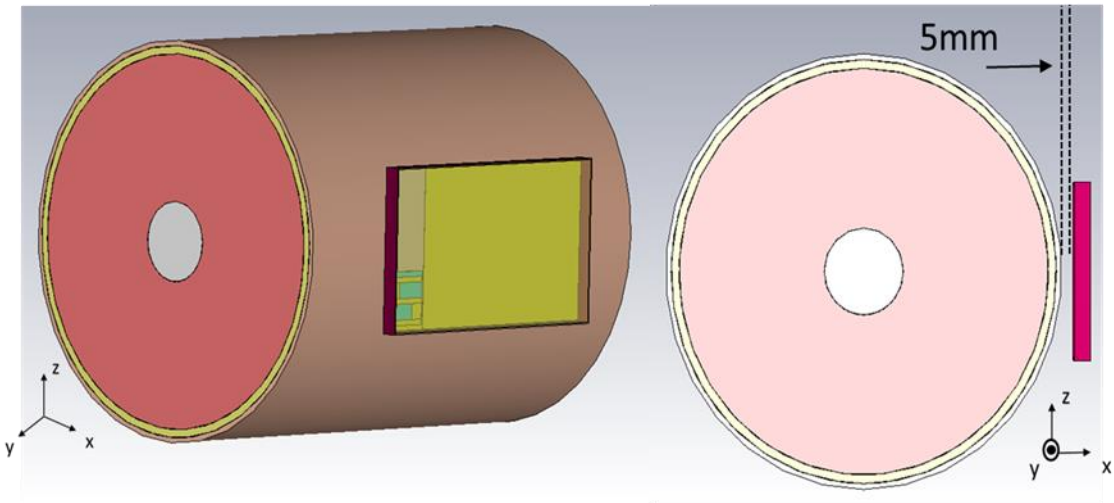

Figure 5.22. Modeling of human leg and PIFA.

As described earlier, placing PIFA close to the human body causes an antenna resonant frequency shift. The resonant frequencies shifted to 866, 858 and 814MHz for $PIFA_{MD}$, $PIFA_{DL}$ and $PIFA_{FR4}$ due to the proximity of the human body. As shown in the human head case, $PIFA_{MD}$ showed the smallest resonance shift among three antennae. The calculated maximum SAR of $PIFA_{MD}$ was 697mW/kg averaged over 1g of tissue with a 100mW input power. The other two antennae have SARs of 834mW/kg and 721mW/kg for $PIFA_{HD}$ and $PIFA_{FR4}$ respectively. The antenna with the MD material substrate showed a significant reduction of SAR as it showed in the human head case. A 16.4% SAR reduction was achieved using the MD material compared to the one using high dielectric constant material with low loss. The resonant frequencies and the maximum SAR of each PIFA are summarized in Table 12. The maximum SAR distributions inside of the human tissues of each PIFA are shown in Figure 5.23. The red region that represents the highest SAR value are much wider for $PIFA_{FR4}$ than other two PIFAs and this could be attributed to the largest antenna size amongst three antennae.

Table 12. Antenna performance with human leg model

Specification	$PIFA_{MD}$	$PIFA_{DL}$	$PIFA_{FR4}$
f_r (MHz)	866	858	814
SAR (mW/kg)	697	834	721

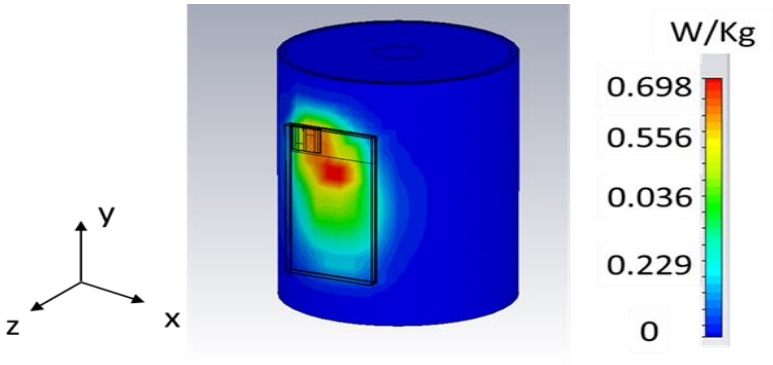

(a)

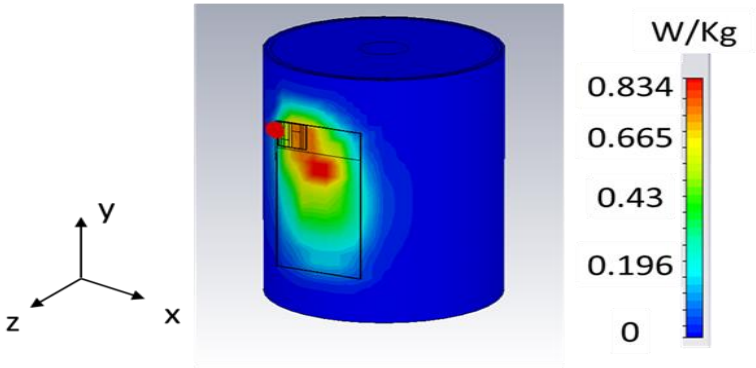

(b)

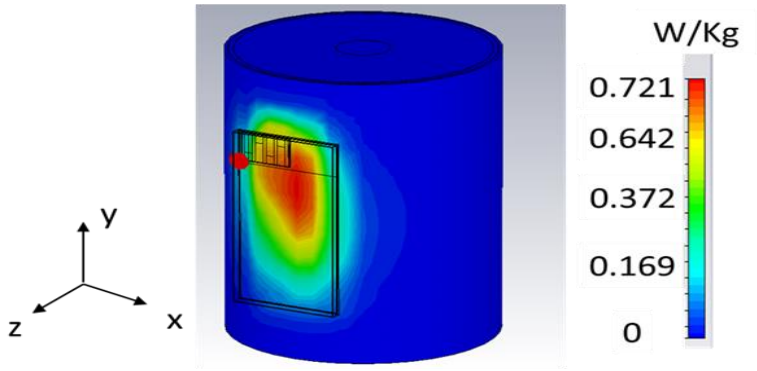

(c)

Figure 5.23. Maximum SAR distribution of (a) $PIFA_{MD}$, (b) $PIFA_{DL}$ and (c) $PIFA_{FR4}$.

5.7 PIFA Fabrication and Measurements

In previous sections 5.3 and 5.4, two types of antenna on MD material were discussed with their comparison summarized in Table 13.

Table 13. Specifications and performance (simulated) of $PATCH_{MD}$ and $PIFA_{MD}$

	$PATCH_{MD}$	$PIFA_{MD}$
Total size (mm^3)	7185.66	7200
Metal patch size (mm^3)	1965.66	360
Size reduction w/ respect to FR4 (%)	73.2	39
Bandwidth (%), VSWR 2:1	4.41	7.24
Radiation Efficiency (%)	8.2	74.19
Gain (dB)	-6.746	1.26
MD volume (mm^3)	10922	400

The $PATCH_{MD}$ shows better size reduction of 73.2% with respect to FR4 material than $PIFA_{MD}$, due to the conductor ground backing. The $PIFA_{MD}$ shows, however, superior antenna performance such as bandwidth, radiation efficiency and gain compared to $PATCH_{MD}$. The $PIFA_{MD}$ also requires less MD material than $PATCH_{MD}$ since the volume of MD material used for the $PATCH_{MD}$ is about 27 times larger than $PIFA_{MD}$. The PIFA antenna is therefore the preferable antenna design for antenna miniaturization. The proposed PIFA in Figure 5.9 was fabricated as shown in Figure 5.24. The size of the MD material for the PIFA substrate is 20 x 20 x 1 mm^3. Since the same process and conditions were used to fabricate the substrate as the sample used in chapter 3, the material properties were expected to be the same. This was verified using the return loss measurements of the antenna.

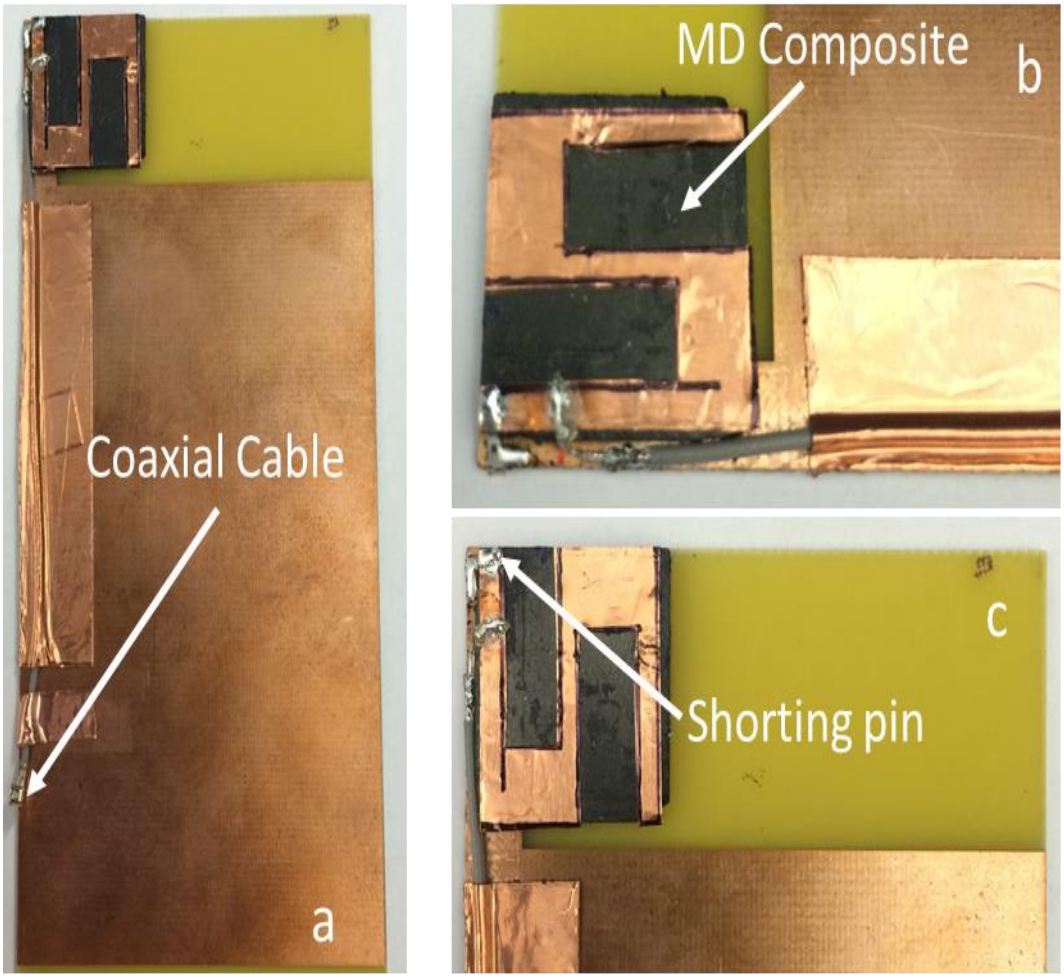

Figure 5.24. Pictures of the planar inverted-F antenna on MD material substrate shown in Figure 5.9.

Meander copper tape was attached on top of the synthesized MD composite and a coaxial cable was used to excite the antenna. The fabricated antenna was measured using a vector network analyzer (VNA) with short, open, load and thru (SOLT) calibration in an anechoic chamber as shown in Figure 5.25.

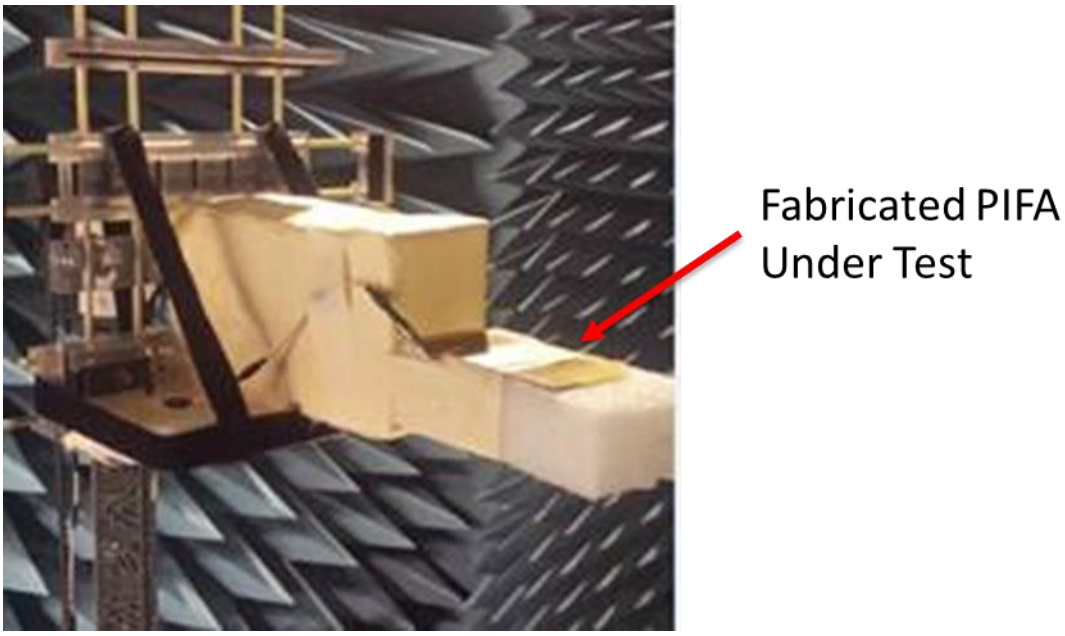

Figure 5.25. Picture of antenna under test in anechoic chamber for measurement.

Simulation and measurement of return loss for the fabricated PIFA are shown in Figure 5.26. These results show measured and simulated resonance frequencies of 944MHz and 910MHz, respectively. The difference in the resonance frequencies is only 34MHz or 3.73%, which demonstrates that the MD material properties are very close to the extracted values. The small frequency offset can be introduced during simulation due to the size difference during fabrication. The bandwidth of 2:1 VSWR is from 911 to 981MHz, which corresponds to a 7.4% bandwidth. A 7.24% bandwidth was obtained from simulation and therefore, measurement and simulation show good agreement for bandwidth as well.

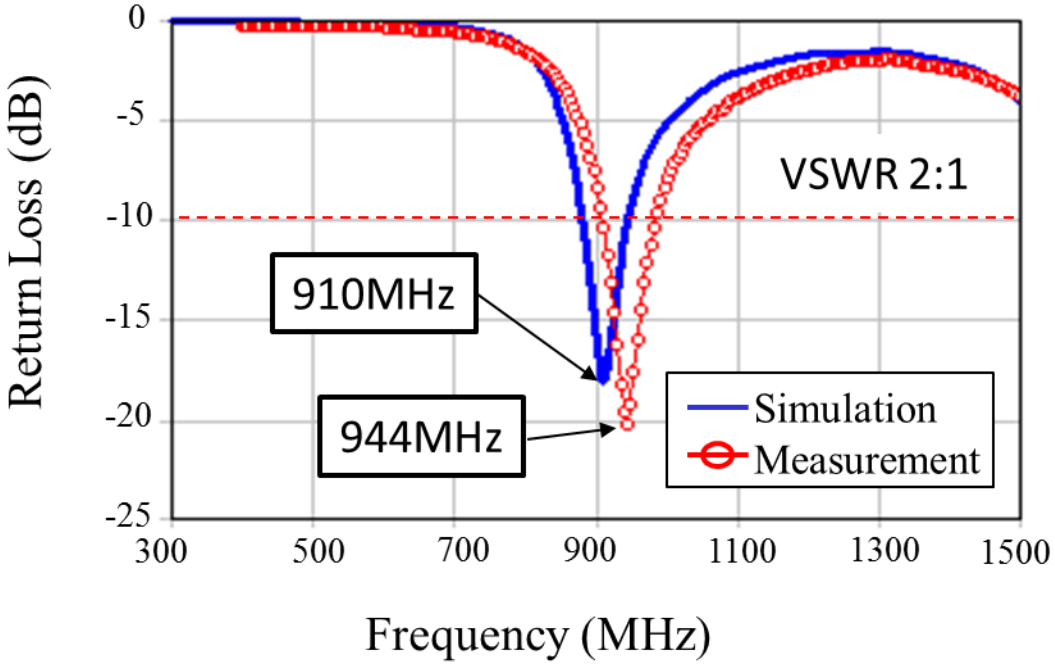

Figure 5.26. Simulation and measurement of return loss of the PIFA in Figure. 5.24.

Simulated and measured radiation efficiency and gain of PIFA are shown in Figures 5.27 and 5.28 respectively. The measured radiation efficiency was 51-61.7 % over the frequency band while the simulated radiation efficiency was 60-76 % over the same band. The measured antenna gain was about -0.3-0.2 dBi over the band which compares to the simulated gain of 0.61-1.29 dBi over the same frequency band. Simulation and measurement showed some difference and it can be attributed to a size difference during fabrication and the effect of the coaxial cable used for measurements. Nevertheless, the measured radiation efficiency of the PIFA still meets the requirements of minimum 30% radiation efficiency for a practical handheld device for most applications in this operating frequency band [23].

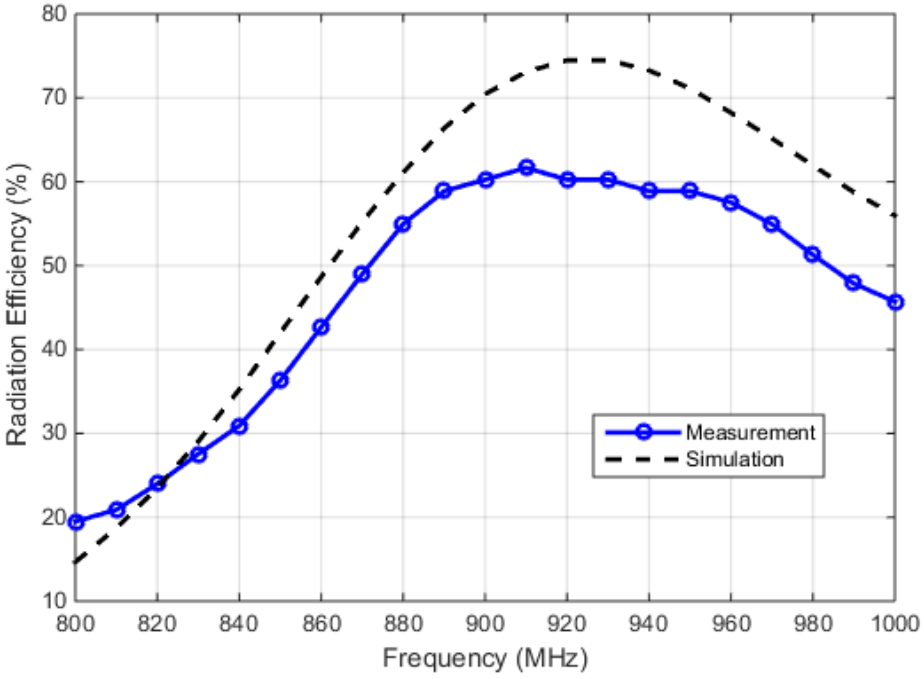

Figure 5.27. Simulated and measured radiation efficiency of the PIFA in Figure. 5.24.

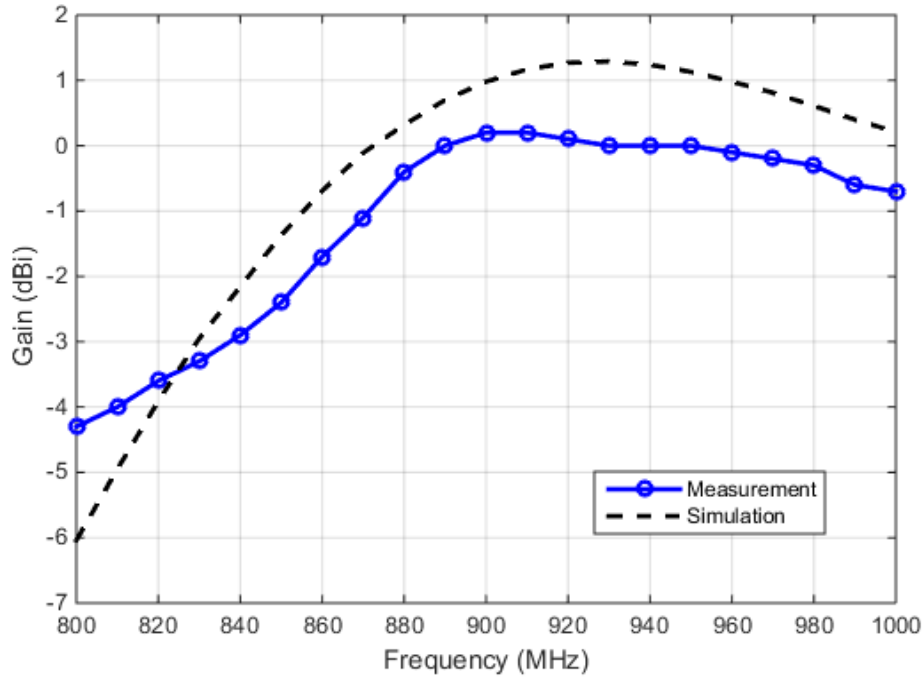

Figure 5.28. Simulated and measured gain of the PIFA in Figure 5.24.

For comparison purposes, simulated and measured radiation patterns are shown in Figure 5.29. The measured radiation patterns are similar to that of the dipole antenna with a null along the negative z axis side and shows good correlation with the simulated radiation pattern.

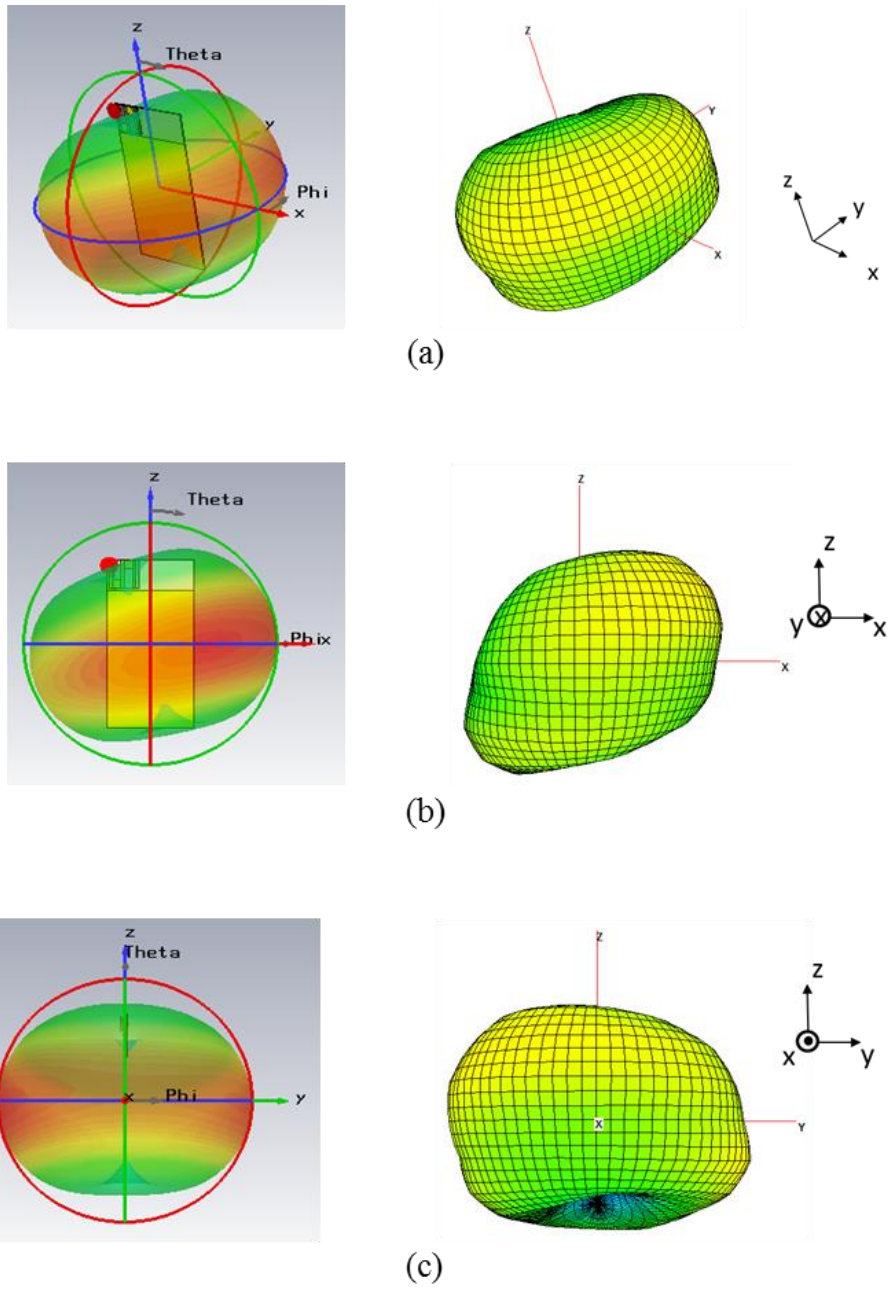

Figure 5.29. Simulated and measured radiation pattern of PIFA (a) perspective view, (b) xz-plane and (c) yz-plane.

Figure 5.30 shows the simulated and measured xy-plane radiation pattern in polar coordinates. Good agreement is obtained with a main lobe at 293 ° in the simulation and 285 ° in the measurement. Comparison between simulated and measured antenna performance of PIFA on MD material substrate is summarized in Table 14 and good agreement between simulation and measurement was obtained.

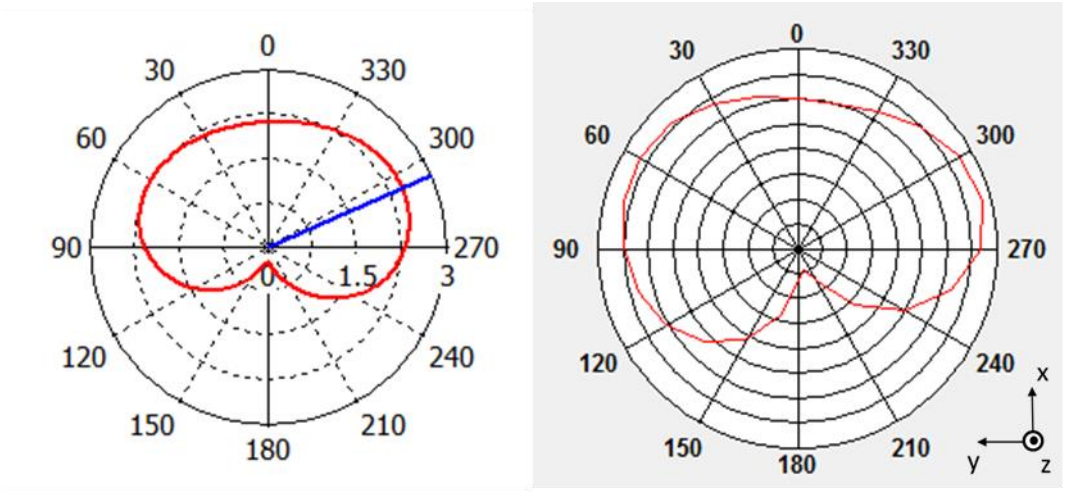

Figure 5.30. Simulated and measured xy-plane radiation patterns in a polar coordinate.

Table 14. Simulated and measured antenna performance for PIFA$_{MD}$.

Result	f_r (MHz)	Bandwidth (%)	Radiation Eff. (%)	Gain (dBi)
Simulation	910	7.24	74.19	1.26
Measurement	944	7.4	61.7	0.2

5.8 Summary

A microstrip patch antenna and a planar inverted-F antenna on magneto-dielectric material substrate were designed and analyzed. Electric and magnetic material properties of MD material were extracted using the method introduced in Chapter 3. Comparing the size of

antennas on a typical FR4 PCB and MD material substrates, antennae on the MD material substrate showed 73.2% and 38.4% size reduction for microstrip patch antenna and PIFA respectively. Antennae on the MD material substrate were compared with other antennae on different substrates, such as FR4 and high dielectric constant material. It was demonstrated that antennas on MD substrate show better antenna performance than the antennas on high dielectric constant material substrate with the same loss as the MD material. Based on simulation, PIFA on the MD material showed 74.2% radiation efficiency while patch antenna on the same MD material showed 8.2%. Therefore, a PIFA type of antenna on MD material is preferable for mobile devices.

In this chapter, the effect of MD material characteristics on the SAR of an antenna was also discussed. It was observed that MD material not only helped minimize the human body effect on antenna performance but also decreased the SAR of the antenna. The resonance shift of the MD antenna due to the proximity of the human body was the smallest amongst other antennae on different material substrates. The SAR of $PIFA_{MD}$ was compared with $PIFA_{DL}$ and $PIFA_{FR4}$ in this chapter. The antennas were placed close to head and leg models to calculate SAR and $PIFA_{MD}$ showed the lowest SAR amongst three antennae in both cases.

PIFA on MD material substrate was fabricated and measured. Simulated and measured antenna performance showed good correlation, which verifies that the extracted values using the method discussed in Section 3 are very close to the actual MD material properties. Measured antenna performance was acceptable for handheld mobile applications in a small size and therefore the magneto-dielectric material can be used for antenna miniaturization.

CHAPTER 6

CONCLUSIONS

With the remarkable development of communication technology, tremendous growth in mobile devices have been achieved. Consumers' demand on high portability and multifunction capability of mobile devices have increased over the years. One of the factors determining the portability of the mobile products is the size, and the size of the antenna has a significant effect in determining the size of the mobile products. Reducing the size of the antenna is very challenging since the performance of the antenna is bounded by the physical size of the antenna. Various methods have been introduced in the literature to reduce the antenna size and their pros and cons were described in this dissertation.

This dissertation primarily focused on miniaturizing antennae using magneto-dielectric composite materials along with material characterization. In Chapter 2, the material characterization method for extracting permittivity and permeability of a synthesized magneto-dielectric composite was presented. A three-pole Lorentzian dispersion equation has been derived to model the extracted material properties and its causality was verified through calculations using Kramers-Kronig relations in Chapter 4. Using the extracted material properties, a 900MHz planar inverted-F antenna was designed, fabricated and measured. The accuracy of the measurement from the characterization method has been verified through good correlation between the simulation and measurement of the antenna performance. The benefits of using magneto-dielectric material on antenna miniaturization was also demonstrated by comparing the performance of an antenna on magneto-dielectric material to other antennas on high dielectric constant

materials and FR4 material in Chapter 5. In Chapter 5, the effect of natural loss characteristics of magneto-dielectric material on Specific Absorption Rate (SAR) reduction also has been presented. Through simulations, it has been observed that using magneto-dielectric material as an antenna substrate can help reduce the SAR of antennae as well as the human body effect on antenna performance without adding any extra structures or extra materials between the antenna and human body.

In conclusion, the magneto-dielectric material is a promising solution for next generation smartphone or wearable type applications. Section 6.1 presents the contributions in this dissertation. The final section shows published papers and inventions.

6.1 Contributions

The contributions of this research are summarized as follows:

Major Contributions:

- An effective and accurate magneto-dielectric material characterization method for frequency-dependent material property extraction has been developed. Its accuracy has been verified through correlation between simulation and measurement.
- Magneto-dielectric composite materials using cobalt-fluoropolymer was synthesized and its properties were measured using the proposed technique from 1 to 4 GHz. Extracted properties of these MD composite materials are the best properties reported in this frequency range for metal nano-composites in the open literature.
- A meander planar inverted-F antenna on MD composite material for 900 GSM band applications has been designed and fabricated. Extracted properties of the

synthesized MD composite material have been used for antenna design and measurements. Antenna performance showed good correlation with simulation results. Though a magnetic loss tangent of 0.068 is considered high for RF antenna application, however, it has been shown that the antenna fabricated using the MD composite material has performance that meets the requirements for handheld devices such as smart phones. As a side benefit, it has been shown that the MD material helps reduce SAR, which is well known, but often overlooked during the antenna design process. It was also observed that the effect of human body on antenna performance can also be reduced using MD material since the refractive index of these materials is close to that of the human body.

Other contributions:

- Mixing rules for MD composite material to predict its properties have been provided as a guideline for material synthesis. Bruggeman's effective medium theory [25] has been applied to predict the effective permeability and Sihvola and Lindell model [24] has been used to estimate the effective permittivity for metal-polymer composite materials.
- Three pole Lorentzian dispersion model for fitting extracted material properties of MD composite materials was developed. Errors between the extracted data and fitting curve were very small. The Kramers-Kronig relations were used to demonstrate that the three pole Lorentzian dispersion model is causal.
- Performance of antennae on MD materials has been compared with other antennae on different materials (High dielectric constant materials and FR4) for two types of

antenna: patch antenna and planar inverted-F antenna. Based on simulation, the narrow bandwidth problem using high dielectric constant materials can be solved using MD materials. For antenna design preference, PIFA antenna on MD material is preferable for mobile devices since it provides better antenna performance than a patch type antenna on the same MD material. The PIFA on MD material is also cost effective because it uses less material than the patch antenna.

6.2 Future Work

The 4 GHz upper frequency limit of cavity perturbation technique using substrate integrated waveguide cavity resonator presented in Chapter 3 is due to the size of the sample. The current sample dimension of 6 x 6mm^2 is too large for increasing resonant frequency beyond 4GHz. Increasing resonant frequency of SIW cavity resonator by decreasing the size of SIW will decrease the isolation level between permittivity and permeability measurement since the inserted sample inside of the SIW cavity will affect both the electric and magnetic field. The 4 GHz upper frequency limit of the method was not sufficient to capture the FMR of the synthesized MD composite materials. MD composite materials measurement beyond 4GHz using smaller size of sample will be necessary for estimating FMR.

In physics and materials science, the Curie temperature (T_c), or Curie point, is the temperature where a material's permanent magnetism changes to induced magnetism [55]. Since the Curie temperature of bulk cobalt is 1400 K, its magnetism would not be sensitive to temperature changes in a regular room environment. The Curie temperature of cobalt nanoparticle is, however, not known and therefore can be an issue. To understand the effect of temperature on material properties, an experiment can be done by placing the SIW cavity

with MD composite material on a hot plate and measuring the change in resonance as a function of temperature. This data can be used to estimate the Curie temperature of the composite material.

6.3 Publications

In the course of the dissertation research, the following journal articles, conference papers, and invention disclosures have been submitted, accepted and published.

1. **Kyu Han**, Madhavan Swaminathan, P. Markondeya Raj, Himani Sharma, Rao Tummala, Brandon Rawlings, Vijay Nair, "RF Characterization of Magneto-Dielectric Material using Cavity Perturbation Technique," submitted to *IEEE Trans. Components, Packaging and Manufacturing Technol.*, Conditionally accepted.
2. **Kyu Han**, Madhavan Swaminathan, P. Markondeya Raj, Himani Sharma, Rao Tummala, Songnan Yang, Vijay Nair, "Magneto-dielectric Nanocomposite for Antenna Miniaturization and SAR reduction," submitted to *IEEE Antennas Wireless Propag. Lett.*, Accepted.
3. **Kyu Han**, Madhavan Swaminathan, P. Markondeya Raj, Himani Sharma, Rao Tummala, Brandon Rawlings, Songnan Yang, Vijay Nair, "Synthesis of Magneto-dielectrics from First Principles and Antenna Design," accepted in *Proc. IEEE Electronic Components and Technol. Conf. (ECTC)*, 2015.
4. **Kyu Han**, Madhavan Swaminathan, P. Markondeya Raj, Himani Sharma, Rao Tummala, Vijay Nair, "Magneto-dielectric Characterization and Antenna Design," *Proc. IEEE Electronic Components and Technol. Conf. (ECTC)*, pp. 782-788, 2014.
5. **Kyu Han**, Madhavan Swaminathan, P. Markondeya Raj, Himani Sharma, Rao Tummala, Vijay Nair, "Magneto-dielectric material cauterization and antenna

design for RF applications," *Antenna and Propagation (EuCAP), 2014 8th European Conference on*, pp. 381-384, 2014.

6. P. Markondeya Raj, P. Chakrabortu, Himani Sharma, **Kyu Han**, S. Gandhi, S. Sitaraman, Madhavan Swaminathan, Rao Tummala, "Tunable and Miniaturized RF Components with Nanocomposite and Nanolayered Dielectrics," *IEEE Nanotechnol. Conf. (IEEE NANO)*, pp. 27-31, 2014.
7. P. Markondeya Raj, Himani Sharma, Dibyajat Mishra, K. P. Murali, **Kyu Han**, Madhavan Swaminathan, Rao Tummala, "Nanomagnetics for High-Performance, Miniaturized Power, and RF Components," *IEEE Nanotechnology magazine*, vol. 6, no. 3, pp. 18-23, 2012.
8. **Kyu Han**, Madhavan Swaminathan, P. Markondeya Raj, Himani Sharma, K.P. Murali, Rao Tummala, Vijay Nair, "Extraction of electrical properties of nanomagnetic materials through meander-shaped inductor and inverted-F antenna structures," *Proc. IEEE Electronic Components and Technol. Conf. (ECTC)*, pp. 1808-1813, 2012.
9. **Kyu Han**, Benjamin Lacroix, John Papapolymerou, Madhavan Swaminathan, "New microstrip-to-CPS transition for millimeter-wave application," *Proc. IEEE Electronic Components and Technol. Conf. (ECTC)*, pp. 1052-1057, 2011.

6.4 Invention Disclosure

- **Kyu Han**, Madhavan Swaminathan, Vijay Nair, P. Markondeya Raj, Himani Sharma, Rao Tummala, "Magneto-dielectric material characterization and antenna design," Invention Disclosure ID: 6626, February 2014.

- P. Markondeya Raj, **Kyu Han**, Vijay Nair, Brandon Rawlings, Himani Sharma, Madhavan Swaminathan, Rao Tummala, "Antennas with three-phase nanocomposite structures and methods thereof," Invention Disclosure ID: 6623, February 2014.
- P. Markondeya Raj, **Kyu Han**, Vijay Nair, Brandon Rawlings, Himani Sharma, Madhavan Swaminathan, Rao Tummala, "Integration of dense magnetic nanocomposites for thin antennas," Invention Disclosure ID: 6624, February 2014.
- P. Markondeya Raj, **Kyu Han**, Himani Sharma, Madhavan Swaminathan, Rao Tummala, "Anisotropic nanocomposite substrates for high-frequency antennas," Invention Disclosure ID: 6622, February 2014.

REFERENCES

[1] H. A. Wheeler, "Fundamental limitations of small antennas," *Proceedings to the IRE*, vol. 35, pp. 1479-1484, December 1947.

[2] J. Volakis, C. Chen, K. Fujimoto, *Small antennas: Miniaturization Techniques and Applications*, McGraw-Hill, New York, 2010.

[3] E. Tsutomu, Yonehiko, S. Shinichi, K. Takashi, "Resonant frequency and radiation efficiency of meander line antennas," *Electronics and Communications in Japan*, vol. 83, pp. 52-58, 2000.

[4] H. T. Nguyen, S. Noghanian, L. Shafai, "Microstrip patch miniaturization by slot loading," *IEEE Antennas and Propagation Society International Symposium*, pp. 215-218, 2005.

[5] M. C. Scardelletti, G. E. Ponchak, S. Merritt, J. S. Minor, C. A. Zorman, "Electrically small folded slot antenna utilizing capacitive loaded slot lines," *IEEE Radio and Wireless Symposium*, vol. 22-24, pp. 731-734, 2008.

[6] J. S. Colburn and Y. Rahmat-Samii, "Patch antennas on externally perforated high dielectric constant substrates," *IEEE Trans. Antennas Propagat.*, vol. 47, pp. 1785-1794, Dec. 1999.

[7] R. K. Mongia, A. Ittipiboon, M. Cuhaci, "Low profile dielectric resonator antennas using a very high permittivity material," *Electron. Lett.*, vol. 30, no. 17, pp. 1362-1363, Aug. 1994.

[8] Y. Jean-Charles, V. Ungvichian, J. A. Barbosa, "Effects of substrate permittivity on planar inverted-F antenna performances," *Journal of Computers*, vol. 4, No. 7, pp. 610-614, 2009.

[9] H. Mosallaei, K. Sarabandi, "Magneto-dielectrics in electromagnetics: concept and applications," *IEEE Trans. Antennas Propagat*., vol. 52, no. 6, pp. 1558-1567, June. 2004.

[10] P. Ikonen, K. Rozanov, A. Osipov, P. Alitalo, S. Tretyakov, "Magnetodielectric substrates in antenna miniaturization: potential and limitations," *IEEE Trans. Antennas Propagat*., vol. 54, no. 11, pp. 3391-3398, Nov. 2006.

[11] R. C. Hansen, M. Burke, "Antennas with magneto-dielectrics," *Microwave and Optical Tech. Lett.*, vol. 26, no. 2, pp.75-78, July 2000.

[12] C. Niamien, S. Collardey, A. Sharaiha, K. Mahdjoubi, "Compact expressions for efficiency and bandwidth of patch antennas over lossy magneto-dielectric materials," *IEEE Antennas and Wireless Propagat. Lett.*, vol. 10, pp. 63-66, 2011.

[13] S. Bae, Y. Mano, "A small meander VHF & UHF antenna by magneto-dielectric materials," *Asia-Pacific Microwave Conference*, vol. 4, no. 4-7, p.3, 2005.

[14] R. Petrov, A. Tatarenko, G. Srinivasan, J. Mantese, "Antenna miniaturization with ferrite-ferroelectric composites," Microwave and Optical Tech. Lett., vol. 50, no. 12, pp. 3154-3157, Dec. 2008.

[15] Y. Shin, S. Park, "A chip antenna with magneto-dielectric material," *Antennas and Propagation Society International Symposium, 2008. AP-S 2008. IEEE*, pp. 5-11 July 2008.

[16] J. Kim, Y. Lee, B. Lee, J. Lee, J. Choi, J. Kim, “Effects of magneto-dielectric ceramics for small antenna application,” *Journal of Electrical Engineering & Technol.*, vol. 9, no. 1, pp. 742-748, Jan. 2014.

[17] Agilent Technology. (2011, June 13). *Agilent E4991A RF Impedance/Material Analyzer* [Online]. Available: http://cp.literature.agilent.com/litweb/pdf/5980-1233E.pdf

[18] N. Altunyurt, M. Swaminathan, P. M. Raj, V. Nair, “Antenna miniaturization using magneto-dielectric substrates,” *in Proc. IEEE Electronic Components and Technol. Conf. (ECTC)*, pp. 801-808, 2009.

[19] J. Baker-Jarvis, E. J. Vanzura, and W. A. Kissick, "Improved technique for determining complex permittivity with transmission/reflection method," *IEEE Tran. Microw. Theory Tech.*, vol. 38, no. 8, pp. 1096-1103, Aug. 1990.

[20] Y. Shin, S. Park, “A monopole antenna with a magneto-dielectric material and its MIMO application for 700 MHz-LTE-band,” *Microw. Optical Technol. Lett.*, vol. 52, no. 10, pp. 2364-2367, 2010.

[21] Y. Cheon, J. Lee, J. Lee, “Quad-band monopole antenna including LTE 700 MHz with magneto-dielectric material,” *IEEE Antennas Wireless Propag. Lett.*, vol. 11, pp. 137-140, 2012.

[22] J. Lee, J. Lee, K. Min, Y. Cheon, “Miniaturized antennas with reduced hand effects in mobile phones using magneto-dielectric material,” *IEEE Antennas Wireless Propag. Lett.*, vol. 13, pp. 935-938, 2014.

[23] B. Park, M. Jeong, S. Park, “A magneto-dielectric handset antenna for LTE/WWAN/GPS applications,” *IEEE Antennas Wireless Propag. Lett.*, vol. 13, pp. 1482-1485, 2014.

[24] I. J. Youngs, N. Bowler, K. P. Lymer and S. Hussain, “Dielectric relaxation in metal-coated particles: the dramatic role of nano-scale coatings,” *J. Phys. D: Appl. Phys.*, vol. 38, pp. 188-201, 2005.

[25] R. Ramprasad, P. Zurcher, M. Miller, P. Renaud, “Fundamental limits of soft magnetic particle composites for high-frequency applications,” *Phys. Stat. Sol.*, vol. 233, pp. 31-38.

[26] P. M. Raj, H. Sharma, S. Samtani, D. Mishra, V. Nair, R. Tummala, “Magnetic losses in metal nanoparticle-insulator nanocomposites,” *J. Mater. Sci.: Mater. Electron.*, 24, no. 9, pp.3448-3455, 2013.

[27] P. Markondeya Raj, P. Chakrabortu, Himani Sharma, Kyu Han, S. Gandhi, S. Sitaraman, Madhavan Swaminathan, Rao Tummala, “Tunable and Miniaturized RF Components with Nanocomposite and Nanolayered Dielectrics,” *IEEE Nanotechnol. Conf. (IEEE NANO)*, pp. 27-31, 2014.

[28] L. F. Chen, C. K. Ong, C. P. Neo, V. V. Varadan, V. K. Varada, *Microwave Electronics: Measurement and Materials Characterization*, Wiley, New York, pp. 250-286, 2004.

[29] H. Lobato-Morales, A. Corona-Chavex, D. V. B. Murthy, J. L. Olvera-Cervantes, "Complex permittivity measurements using cavity perturbation technique with substrate integrated waveguide cavities," *Review of Scientific Instruments*, 81.6, 2010.

[30] K. Saeed, R. D. Pollard, I. C. Hunter, "Substrate integrated waveguide cavity resonators for complex permittivity characterization of materials," *IEEE Trans. Microwave Theory and Techniques*, vol. 56, no. 10, pp.2340-2347 2008.

[31] CST Microwave Studio, Computer Simulation Technology, [Online]. Available: http://www.cst.com/Products/CSTMWS

[32] Rogers Corp., "RO3000 Series Circuit Materials," [Online]. Available: http://www.rogerscorp.com/documents/722/acm/RO3000-Laminate-Data-Sheet-RO3003-RO3006-RO3010.pdf

[33] Rogers Corp., "RO4360G2 High Frequency Laminates," [Online]. Available: http://www.rogerscorp.com/documents/2483/acm/RO4360G2-High-Frequency-Laminates-Data-Sheet.pdf

[34] Cuming Microwave, [Online]. Available: http://cumingmicrowave.com/pdf/Permittivity-Permeability/FLX-16.pdf

[35] Rogers Corp., "RO4000 Series High Frequency Circuit Materials," [Online]. Available: http://www.rogerscorp.com/documents/726/acm/RO4000-Laminates---Data-sheet.pdf

[36] Rogers Corp., "TMM Thermoset Microwave Materials," [Online]. Available: http://www.rogerscorp.com/documents/728/acm/TMM-Thermoset-laminate-data-sheet-TMM3-TMM4-TMM6-TMM10-TMM10i.aspx

[37] A. N. Lagarkov and K. N. Rozanov, "High-frequency behavior of magnetic composites," *J. Magn. Magn. Matter.*, vol. 321, pp. 2082-2092, 2009.

[38] Wikipedia, "Magnetocrystalline anisotropy," [Online]. Available: http://en.wikipedia.org/wiki/Magnetocrystalline_anisotropy

[39] A. E. Engin, "Extraction of Dielectric Constant and Loss Tangent Using New Rapid Plane Solver and Analytical Debye Modeling for Printed Circuit Boards," *IEEE Trans. Microw. Theory Tech.*, vol. 58, pp. 211-219, 2010.

[40] Wikipedia, "Electric susceptibility," [Online]. Available: http://en.wikipedia.org/wiki/Electric_susceptibility

[41] Wikipedia, "Magnetic susceptibility," [Online]. Available: http://en.wikipedia.org/wiki/Magnetic_susceptibility

[42] C. Vittoria, *Magnetics, Dielectrics, and Wave Propagation with MATLAB® Codes*, CRC Press, Boca Raton, pp. 271-276, 2011.

[43] M. Koledintseva, K. Rozanov, A. Orlandi, J. Drewniak, "Extraction of Lorentzian and Debye parameters of dielectric and magnetic dispersive materials for FDTD modeling," *J. of Electrical Engineering*, vol. 53, pp. 97-100, 2002.

[44] K. N. Rozanov, Z. W. Li, L. F. Chen, M. Y. Koledintseva, "Microwave permeability of Co_2Z composites," *J of Appl. Phys.*, vol. 97, pp. 013905, 2005.

[45] Wikipedia, "Specific absorption rate," [Online]. Available: http://en.wikipedia.org/wiki/Specific_absorption_rate.

[46] Agilent, "Agilent 4291B RF Impedance/Material Analyzer Data Sheet," [Online]. Available: http://literature.cdn.keysight.com/litweb/pdf/5966-1543E.pdf

[47] J. Lee, J. Heo, J. Lee, Y. Han, "Design of small antennas for mobile handsets using magneto-dielectric material," *IEEE Trans. Antennas Propag.*, col. 60, no. 4, pp. 2080-2084, 2012.

[48] S. Kwak, D. Sim, J. Kwon, "Design of Optimized Multilayer PIFA with the EBG Structure for SAR Reduction in Mobile Applications," *IEEE Trans. Electromagnetic Compatibility*, vol. 53, no. 2, pp. 325-331, 2011.

[49] S. Zhu, R. Langley, "Dual-band Wearable Textile Antenna on an EBG Substrate," *IEEE Trans. Antennas Propag.*, vol. 57, no. 4, pp. 926-935, 2009.

[50] J. Hwang, F. Chen, "Reduction of the Peak SAR in the Human Head with Metamaterials," *IEEE Trans. Antennas Propag*., vol. 54, no. 12, pp. 3763-3770, 2006.

[51] M. Faruque, N. Misran, M.T. Islam, "Split ring resonators for SAR reduction in human head," *in Proc. Asia-Pacific Conf.*, pp. 880-883, 2011.

[52] M. Faruque, N. Misran, M.T. Islam, "EM Absorption Reduction of Helix with Shielding Material for Mobile Phone Applications," *Electrical, Control and Computer Engineering Conf.*, pp. 17-21, 2011.

[53] Medical Anatomy, "Human Body Outline Drawing," [Online]. Available: http://medicalanatomy.net/human-body-outline-drawing/

[54] K. R. Holmes, "Thermal Conductivity Data for Specific Tissues and Organs for Humans and Other Mammalian Species," Thermal Properties 2009.

[55] Wikipedia, "Curie temperature," [Online]. Available: http://en.wikipedia.org/wiki/Curie_temperature.